Normal impact of liquid droplets on smooth solid surfaces

Yang Xu

THÈSE POUR OBTENIR LE GRADE DE DOCTEUR DE UNIVERSITÉ PARIS EST

En: Mécanique

École Doctorale: Sciences, Ingénierie et Environnement(SIE)
Unité de recherche: Laboratoire MSME UMR 8208 CNRS

Normal impact of liquid droplets on smooth solid surfaces

présentée par

XU Yang

soutenue le 17 Octobre 2018

Devant le jury composé de

ESTIVALEZES Jean-luc	Professeur, IMFT	Rapporteur de thèse
MEILLOT Erick	Ingénieur de Recherche, CEA	Rapporteur de thèse
CALTAGIRONE Jean-Paul	Professeur, I2M	Examinateur de thèse
FUSTER Daniel	Recherche associé, CNRS	Examinateur de thèse
VINCENT Stéphane	Professeur, MSME	Co-Directeur de thèse
HE Qi-Chang	Professeur, MSME	Co-Directeur de thèse
LE QUANG Hung	Professeur associé, MSME	Co-Encadrant de thèse

Abstract

Under the framework of the LabEx Multi-Scale Modelling and Experimentation of Materials for Sustainable Construction, of Université Paris-Est Marne-La-Vallée, the present PhD thesis aims at modelling and characterizing micro-material designed by impact of molten ceramic droplets. The applications of thin coating materials are surface treatments for sustainable construction such as anti-corrosion, heat barrier, glass treatment or mechanical reinforcement of specific structures.

In particular, we focus on the physics behind the liquid droplets' dynamics (the contact area and the contact time between the droplet and surface) by conducting a series of small scale multiphase flow numerical simulations with home-made code Thetis. All simulations are axisymmetric. We have considered variations of initial impact conditions, and studied the influence of inertial, capillary and viscous forces on the droplets' dynamics, especially the maximum spreading diameter, spreading time and the contact time, on solid surfaces. The code is based on Volume-Of-Fluid techniques and introduces an auxiliary smooth function to estimate the local curvature and the normal to the interface. The major reference liquid adopted are the water and the molten ceramic, the water is chosen to validate our code against available experiments at the beginning. The molten ceramic is adopted as it is widely used in thermal spray to built thermal and chemical barriers (anti-oxidant layers) as well as mechanical reinforcements on specific samples. We focus on the cases in which the surfaces are hydrophobic, even if hydrophilic cases are also considered in validation configurations for the sake of generality. Meanwhile, by introducing an energy calculation part in the code, a detailed energetic analysis of the droplet after impact is performed in both the spreading and retraction stage to have a deep understanding of the dynamics inside the droplet.

We find the jetting time is inversely proportional to the impact velocity, independent of the contact angle in the early spreading. A new scaling between maximum spreading and spreading time is observed, and agrees well with experimental results. Further, we introduce this scaling into the model based on energy conservation to predict the maximum spreading factor,

which provides better prediction on maximum spreading factor than existing literature references. Also a scaling of contact time is proposed in terms of Ohnesorge number and Reynolds number.

Résumé en français de la thèse

Dans le cadre de la modélisation et de l'expérimentation multi-échelles (projet LabEx MMCD pour les matériaux pour la construction durable) de l'Université Paris-Est Marne-la-Vallée, cette thèse de doctorat vise à modéliser et caractériser les micro-matériaux conçus par impact de gouttelettes de céramique fondue. Les applications de ces matériaux revétus de couches minces sont des traitements de surface pour la construction durable tels que la protection anti-corrosion, les barrières thermiques, le traitement du verre ou les renforts mécaniques.

En particulier, nous nous concentrons sur la physique associée à la dynamique des gouttelettes liquides (l'aire de contact et le temps de contact entre la gouttelette et la surface) en effectuant une série de simulations numériques pour les écoulements diphasiques à petite échelle avec le code maison Thetis. Nous avons considéré des variations des conditions d'impact initiales ainsi que l'influence des forces d'inertie, capillaire et visqueuses sur la dynamique des gouttelettes. Nous nous sommesintéressés en particulier au diamètre d'étalement maximal, au temps d'étalement maximal et au temps de contact, sur des surfaces solides de mouillabilité variable. Le code est basé sur l'utilisation d'une méthode Volume-Of-Fluid. Il introduit une fonction auxiliaire régularisée pour estimer la courbure locale et la normale à l'interface. Les principaux liquides de référence adoptés sont l'eau et la céramique fondue, l'eau est choisie pour valider notre code en comparant les simulations aux résultats expérimentaux. La céramique fondue est adoptée car elle est largement utilisée en projection thermique pour créer des barrières thermiques et chimiques (couches anti-oxydantes) ainsi que des renforts mécaniques sur des échantillons spécifique. Nous nous concentrons sur les cas où les surfaces sont hydrophobes, même si les cas hydrophiles sont également considérés dans les configurations de validation pour des raisons de généralité. Egalement, en introduisant une partie de calcul de l'énergie dans la thèse, une analyse énergétique détaillée de la gouttelette après l'impact est effectuée dans les phases d'étalement et de rétraction pour bien comprendre la dynamique à l'intérieur de la gouttelette.

Nous trouvons que le temps de projection est inversement proportionnel à la vitesse d'impact, indépendamment de l'angle de contact lors de l'étalement au temps courts. Une nouvelle mise à l'échelle entre l'étalement maximal et le temps d'étalement est proposée. Celle-ci s'accorde très bien avec les résultats expérimentaux. Par ailleurs, nous introduisons cette mise à l'échelle dans une classe de modèle basée sur la conservation de l'énergie pour prédire l'étalement maximal adimensionné, ce qui permet de mieux prévoir l'étalement maximal adimensionné. Pour finir, une mise à l'échelle du temps de contact est proposée en termes de nombre d'Ohnesorge et de Reynolds.

Contents

List of Figures **V**

List of Tables **XI**

Nomenclature **XIII**

1 General Introduction **1**

1.1 Introductory Remarks 1

1.2 Literature Review 5

1.2.1 Maximum Spreading Diameter 7

1.2.2 Retraction Dynamics 9

1.3 Introduction of Numerical Code Thetis 11

1.4 Computational Treatment 15

1.4.1 Energy Calculation 15

1.4.2 Validation of Computational Model 16

1.5 Motivations 19

2 Characteristic Spread Factor ξ **24**

2.1 The Jetting Time 24

2.2 Effects of Wettability on Early Spreading 26

2.3 The recoil stage 29

2.3.1 Effects of the Weber and Ohnesorge numbers on recoil 31

2.3.2 Effects of the contact angle on recoil 34

2.4 Numerical results compared to the relevant analytical ones 35

2.5 Summary 37

3 Maximum Spreading State of Droplets Impacting On Hydrophobic Surfaces 39

3.1 Maximum Spreading Factor ξ_{max} and Maximum Contact Factor ξ_{c_max} 41

3.1.1 The effects of impact velocity, surface tension and dynamic viscosity on ξ_{max} 43

3.2 The Maximum Spreading Time t_{max} 50

3.2.1 The influences of impact velocity, surface tension and dynamic viscosity on t_{max} 50

3.3 The Correlation Between Maximum Spreading Diameter D_{max} and Spreading Time t_{max} 57

3.4 Summary 61

4 The Droplets' Bouncing-Off State On Superhydrophobic Substrates 63

4.1 Droplet's Geometric Shapes At Bouncing-Off Instant 65

4.2 A scaling function Of Contact Time t_c 69

4.2.1 The influence of impact velocity V_0 69

4.2.2 The influence of surface tension σ on contact time t_c 71

4.2.3 The influence of dynamic viscosity μ on contact time t_c 73

4.2.4 A scale function for contact time 74

4.2.5 The Influence of Contact Angle θ on Contact Time t_c 75

4.2.6 The retraction time t_r 76

4.3 Summary 77

5 Energetic Analysis of Droplets' Dynamics on Solid Surface 79

5.1 Energetic Analysis Based on Numerical Simulation Results 81

5.1.1 The energy evolution during dynamics 82

5.1.2 Energy Balance at The Maximum Spreading State 86

5.1.3 Energy Balance at The Bouncing-Off Instant 89

5.2 Brief review of several theoretical cylinder models on predicting droplets' maximum spreading 93

5.2.1 The model of Chandra and Avedisian [16] 94

5.2.2 The model of Pasandideh-Fard *et al.* [72] 95

5.2.3 The model of Ukiwe and Kwok [99] 96

5.2.4 The model of Lee *et al.* [56] 97
5.2.5 Refinement of the Models 97
5.3 Summary 101

6 General Conclusions **103**

References **106**

A The properties of liquids and impact conditions in the experiments by Lee *et al.* [56] and Huang and Chen [40] **118**

List of Figures

1.1 Different dynamics and outcomes after droplets' impact on solid surfaces. (a) Molten ceramic, $We = 4.275$, $Re = 14.25$, $\theta = 30°$; (b) Molten ceramic, $We = 3847.5$, $Re = 427.5$, $\theta = 120°$; (c) Water, $We = 46$, $Re = 2129$, $\theta = 96°$; (d) Molten ceramic, $We = 4.275$, $Re = 14.25$, $\theta = 135°$. 3

1.2 Two-dimensional representation of a droplet on substrate describing interfacial tensions. 6

1.3 Sketch of a droplet impacting on a solid surface according to the 1-fluid model. 13

1.4 The grid dependence of the evolution of the spread factor ξ of a molten ceramic droplet impacting at $V_0 = 20m/s$ on the surface with contact angle $\theta = 90°$. . . 18

1.5 Numerical simulations of the spread of a water droplet with the parameters of Šikalo *et al.* [88], $D_0 = 2.7mm, V_0 = 1.17m/s, We = 50$. (a) on a smooth glass surface, (b) on a rough glass surface, (c) on a PVC surface, (d) on a wax surface. 19

2.1 Numerical simulations of the liquid droplet on solid surface ($\theta = 165°$) showing the geometric shape before impact and after impact. (a) Ceramic droplet impact at $V_0 = 5m/s$, $We = 8.55$, $Re = 28.5$. The interval between each picture is set as $\Delta t/(D_0/V_0) = 0.083$. (b) Ceramic droplet impact at $V_0 = 10m/s$, $We = 34.2$, $Re = 57$. The interval is $\Delta t/(D_0/V_0) = 0.083$. (c) Ceramic droplet impact at $V_0 = 20m/s$, $We = 342$, $Re = 114$. The interval is $\Delta t/(D_0/V_0) = 0.063$. 25

2.2 The jetting time of a droplet impacting at varied initial velocities onto solid surfaces with different wetting properties. ($We = 36.8 \sim 92095.8$) 26

2.3 The effects of wettability on the spread factor of water droplet impact at varied impact velocities. (a) In the high Weber number regime ($We > 2000$): the black symbols for the $V_0 = 8m/s$ ($We = 2357.6, Re = 21513.6$), red for $V_0 = 10m/s$ ($We = 3683.8, Re = 26892$), blue for $V_0 = 15m/s$ ($We = 8288.6, Re = 40338$), magenta for $V_0 = 20m/s$ ($We = 14735.3, Re = 53784$), green for $V_0 = 50m/s$ ($We = 92095.8, Re = 134460$). (b) In the low Weber number regime ($We < 200$): the black symbols for the $V_0 = 1m/s$ ($We = 36.8, Re = 2689.2$), red for $V_0 = 1.5m/s$ ($We = 82.8, Re = 4033.8$), green for $V_0 = 2m/s$ ($We = 147.3, Re = 5378.4$), blue for $V_0 = 2.5m/s$ ($We = 230.24, Re = 6723$), magenta for $V_0 = 3m/s$ ($We = 331.5, Re = 8067.6$) and dark yellow for $V_0 = 5m/s$ ($We = 920.96, Re = 13446$). 27

2.4 The transition zone of the effects of wettability on the spread factor of a water droplet impacting at $V_0 = 1m/s$ ($We = 36.8, Re = 2689.2$) onto different surfaces. 28

2.5 Time-evolving spread factor of a droplet upon impacting on the target surface with different wettability characterised by contact angles with $We = 8.55$ and $Re = 28.5$. 29

2.6 Microdroplet impact and spreading simulation at $We = 8.55$ and $Re = 28.5$ on a hydrophobic substrate($\theta = 135°$). Left: velocity field. Right: pressure field. . 30

2.7 Time-evolving spread factor of a droplet upon impacting on the hydrophobic surfaces with $Oh \approx 0.1$. (a) droplet impacting on surface with $\theta = 120°$; (b) droplet impacting on surface with $\theta = 135°$; (c) droplet impacting on surface with $\theta = 150°$; (d) Time-evolving spread factor during recoil stage ($t^*/We^{1/2} > 0.5$) of different non-dimensional numbers, black color for droplet impacting on the surface with $\theta = 120°$, red for $\theta = 135°$, blue for $\theta = 150°$. 31

2.8 Effect of the Ohnesorge number on the droplet impact dynamics with the dimensionless number $We = 34.2$ on the solid surface. (a) with $\theta = 135°$, (c) with $\theta = 150°$. (b) and (d) present the partial curves after $\hat{t} = 0.5$ of (a) and (c), respectively. The red dash line is the second-order polynomial fitting curve of the symbols. 33

2.9 Water droplet impact onto smooth solid surfaces: $We = 37$, $Re = 2022$, $\theta = 30°$. 36

2.10 Water droplet impact onto smooth solid surfaces: $We = 37$, $Re = 2022$, $\theta = 120°$. 36

3.1 Definition sketch of the maximum spreading diameter D_{max} and maximum contact diameter D_{c_max}. 42

3.2 The maximum spreading factor ξ_{max} plotted versus impact velocity V_0. (a) with varied dynamic viscosity μ, (b) with varied surface tension σ. 43

3.3 (a) The maximum spreading factor ξ_{max} plotted versus dynamic viscosity μ. (b) The maximum spreading factor ξ_{max} plotted versus surface tension σ. 44

3.4 The maximum spreading factor ξ_{max} normalised by $Re^{0.2}$ as a function of $WeRe^{0.4}$. 45

3.5 The maximum spreading factor ξ_{max} (a) and the maximum contact factor ξ_{c_max} (b) normalised by $Re^{0.2}$ as a function of $WeRe^{-2/5}$. 46

3.6 The difference between maximum spreading factor ξ_{max} and the maximum contact factor ξ_{c_max} plotted versus Weber number. 46

3.7 The maximum contact factor ξ_{c_max} normalised by $Re^{1/5}$ as a function of $WeRe^{2/5}$. 47

3.8 The maximum spreading factor ξ_{c_max} and $(\xi_{max}^2 - 1)^{1/2}$ normalised by $Re^{1/5}$ plotted versus $WeRe^{-2/5}$. 49

3.9 The maximum spreading time t_{max} for the droplets with varying dynamic viscosity impacting on purely non-wetting surfaces at velocities from $3\ m/s$ to $25\ m/s$. 51

3.10 The dimensionless maximum spreading time t_{max}^* plotted against Reynolds number for the droplets with varied dynamic viscosity impacting on purely non-wetting surfaces. 52

3.11 The time t_{max} for the droplet to reach its maximum spreading state plotted against different values of surface tension coefficient σ. The Weber number is in the range of $2.18 \sim 267.2$. 53

3.12 The dimensionless maximum spreading time t_{max}^* plotted against Weber number for the droplets with varied surface tension impacting on purely non-wetting surfaces. 54

3.13 The function $t_{max}^*/Re^{1/5}$ plotted versus the impact number $P = WeRe^{-2/5}$. All the data shown in Fig.3.10 and Fig.3.12 are included. 55

3.14 Comparison between the scaling relation Eq.(3.13) and experimental results. The symbols represent experimental results from the works of Lee *et al.* [56] and Huang and Chen [40]. 56

3.15 (a) The ratio ξ_{c_max}/t^*_{max} versus Weber number. (b) The ratio ξ_{max}/t^*_{max} versus Weber number. 58

3.16 (a) The rescaled ratio ξ_{c_max}/t^*_{max} as a function of $Oh(WeRe^{-2/5})$. (b) The rescaled ratio ξ_{max}/t^*_{max} as a function of $Oh(WeRe^{-2/5})$. 58

3.17 Comparison between the prediction of the dimensionless spreading time t^*_{max} and the experiments. (a), (b) and (c) are the experiments performed by Lee *et al.* [56]. (d) are the experiments performed by Huang and Chen [40]. 60

4.1 The geometric shapes of droplet (with varied dynamic viscosity μ) at maximum spreading state and bouncing-off state. (a) $V_0 = 5\ m/s$, $We = 4.275$, (b) $V_0 = 10\ m/s$, $We = 17.1$, (c) $V_0 = 15\ m/s$, $We = 38.475$, (d) $V_0 = 20\ m/s$, $We = 68.4$. 66

4.2 The geometric shapes of droplet (with varied surface tension σ) at maximum spreading state and bouncing-off state. (a) $V_0 = 5\ m/s$, $Re = 14.25$, (b) $V_0 = 10\ m/s$, $Re = 28.5$, (c) $V_0 = 15\ m/s$, $We = 42.75$, (d) $V_0 = 20\ m/s$, $Re = 57$. 67

4.3 The pressure contour P and velocity vector $\mathbf{V}$ in the droplet impacting at $V_0 = 10\ m/s$, $We = 17.1$, $Re = 28.5$. And at $t = 6.85e-6\ s$, $7e-6\ s$, $8e-6\ s$, the regions around the air-bubbles are zoomed. 68

4.4 The lift-velocity V_1 contour and velocity vector $\mathbf{V}$ inside the droplet during the retraction stage. The droplet impacts at impact velocity $V_0 = 10\ m/s$, $We = 17.1$, $Re = 28.5$ onto superhydrophobic surfaces. 69

4.5 The dimensionless contact time t^*_c, contact time normalised by D_0/V_0, as a function of the impact velocity. 70

4.6 The contact time t_c between droplet and surface versus the surface tension coefficient σ. The dynamic viscosity μ is constant ($\mu = 0.03\ Pa \cdot s$), the impact velocity V_0 and the surface tension coefficient σ are varied in a certain range ($2.67 < We < 267$). 72

4.7 The contact time t_c^* plotted with dynamic viscosity μ. 73
4.8 The dimensionless contact time t_c^* plotted with Ohnesorge number. The black and red dash lines are the fitting curves plotted by Padé approximation and exponential function, respectively. 75
4.9 The dimensionless contact time t_c^* of bouncing droplet on surfaces with different contact angles $\theta = 120°, 150°, 170°$. 76
4.10 The dimensionless contact time t_c^* and retraction time t_r^* plotted with Ohnesorge number. 77

5.1 Time evolution of water droplet impacting on a steel surface at $V_0 = 1.1\ m/s$. The upper row is adopted from the work by Lee *et al.* [55]. The second row is the results of numerical simulation. The red line presents the liquid/gas interfaces from experiments, measured by shadowgraphy and the the black line presents the interfaces from numerical simulations. The left contour map shows the kinetic energy per unit volume, and the right presents the dissipation function ϕ. 82
5.2 Time-evolving energy components's percent at low impact velocity on a hydrophobic surface ($\theta = 170°$). The two columns: (a) $V_0 = 3\ m/s$, $We = 1.539$, $Re = 2.85$, (b) $V_0 = 20\ m/s$, $We = 68.4$, $Re = 19$. 84
5.3 The ratio between the dissipation in spreading and the total dissipation W_{max}/W_{BC} plotted versus $WeRe^{-3/4}$. 86
5.4 Energy components's portion at maximum spreading state when droplets impact on a hydrophobic surface ($\theta = 170°$). The diamond ($\diamond$), circle ($\circ$) and square ($\square$) represent the ratio of E_{max}^K/E_0, E_{max}^S/E_0 and W_{max}/E_0, respectively. The colours indicate different impact velocities of the impacting droplets. 87
5.5 Energy components's variations at maximum spreading state when droplets impact on a hydrophobic surface ($\theta = 170°$). 88
5.6 The restitution coefficient ϵ plotted versus surface tension σ (a) and viscosity μ (b). 89

5.7 The energy components' variations ΔE_{BC}^{K}, ΔE_{BC}^{S}, ΔW_{BC}, between droplets' bouncing-off instant and the end of relaxing phase on superhydrophobic surfaces. (a) $V_0 = 3\ m/s$, $We = 1.539$, (b) $V_0 = 5\ m/s$, $We = 4.275$, (c) $V_0 = 15\ m/s$, $We = 38.475$, (d) $V_0 = 25\ m/s$, $We = 106.875$. 91

5.8 The energy components' percent $\Delta W_{BC}/\Delta E_{BC}^{S}$, $\Delta E_{BC}^{K}/\Delta E_{BC}^{S}$ between droplets' bouncing-off instant and maximum spreading state on purely non-wetting surfaces. (a) Lower velocity, $V_0 = 3, 4, 5\ m/s$, (b) Higher velocity, $V_0 = 15, 20, 25\ m/s$. 92

5.9 The energy components' percent $\Delta W_{BC}/\Delta E_{BC}^{S}$ (symbol with solid line), $\Delta E_{BC}^{K}/\Delta E_{BC}^{S}$ (symbol with dash line) between droplets' bouncing-off instant and maximum spreading state on purely non-wetting surfaces. 93

5.10 Comparison between maximum spreading factor predictions and experimental results. (a), (b), (c) presents experiments of ethanol, water, glycerol droplets impacting on aluminium surface by Lee *et al.* [56], respectively. (d) presents experiments of water droplets impacting on parafilm surface by Huang and Chen [40]. The red and black lines indicate predictions calculated with $\theta_D(t_{max})$, grey lines for predictions with θ. The legend for lines is given in (a). 99

5.11 Comparison of maximum spreading factor predictions ξ_{max} ((a-1) and (b-1)) and dissipation work W_{max} ((a-2) and (b-2)) between theoretical predictions and numerical simulations with varied viscosity. The first row (a) presents the case in which a ceramic droplet impacts at $V_0 = 5\ m/s$ on a superhydrophobic surface, $We = 4.275$. The row (b) gives the case where a ceramic droplet impacts at $V_0 = 20\ m/s$ on a superhydrophobic surface, $We = 68.4$. 101

List of Tables

1.1 Equilibrium contact angles calculated from Šikalo *et al.* [88] 17

2.1 The list of values of a_1, a_2 and a_3 obtained from simulations ($We = 34.2, \theta = 135°$) 34

3.1 The fitting functions of $t_{max} \sim f(\sigma)$ in Fig.3.11 53

4.1 The fitting functions in each case with different Ohnesorge number in Fig.4.5. . 71

4.2 The fitting functions in each case with different Reynolds number in Fig.4.6. . . 72

A.1 Impact Conditions and Properties of Liquids at $25°$ [56] 118

A.2 Contact angles measured of liquid droplet on surfaces at $25°$ [56] 119

Nomenclature

b	Ratio of Liquid's Surface Tension to Water	
C	Color Function	
C_S	Smooth Color Function	
D_0	Initial Diameter	m
D_{c_max}	Maximum Contact Diameter	m
E	Energy	$N \cdot m$
$\mathbf{F}_{ST}$	Continuum Surface Force	
g	Acceleration Due to Gravity	m/s^2
h	Height of The Droplet	m
$\mathbf{n}$	Interface Normal Vector	
P	Pressure	Pa
R_0	Initial Radius	m
t	Time	s
t_j	The Jetting Time	s
t_{relax}	The Relaxing Time	s
t_c	Contact Time	s
t_r	Retraction Time	s
$\mathbf{u}$	Velocity Vector	
u_x	Velocity component in radial direction	m/s
u_y	Velocity component in axial direction	m/s
V_0	Initial Impact Velocity	m/s
W	Dissipation	$N \cdot m$
Δx	The dimension of unit volume	m
Δt	The time step	s

Dimensionless Numbers

h^*	Dimensionless Height of The Droplet	h/D_0
t_*	Dimensionless Time	$t/(D_0/V_0)$
Bo	Bond Number	$\rho g D_0^2/\sigma$
Oh	Ohnesorge Number	$\sqrt{We}/Re$
P	Impact Number	$WeRe^{-2/5}$
Re	Reynolds Number	$\rho V_0 R_0/\mu$
We	Weber Number	$\rho V_0^2 R_0/\sigma$

Greek Symbols

δ	Dirac Function	
ϵ	Restitution Coefficient	
ξ	Spreading Factor	D/D_0
ξ_{c_max}	Maximum Contact Factor	D_{c_max}/D_0
κ	Local Curvature	
ϕ	Dissipation Function	
Ω	Dissipation Volume	
ρ	Density	kg/m^3
μ	Dynamic Viscosity	$Pa \cdot s$
θ	Equilibrium Contact Angle	$^\circ$
θ_D	Dynamic Contact Angle	$^\circ$
θ_{adv}	Advancing Contact Angle	$^\circ$
θ_{rec}	Receding Contact Angle	$^\circ$
σ	Liquid/Gas interfacial Tension	N/m
σ_{SL}	Solid/Liquid interfacial Tension	N/m
σ_{SG}	Solid/Gas interfacial Tension	N/m

Superscript

K	Kinetic Energy
S	Surface Energy

Subscript

0	Inital State
BC	Bouncing-Off State
max	Maximum Spreading State
$relax$	Relaxing Phase

Chapter 1

General Introduction

1.1 Introductory Remarks

The impact of a liquid droplet onto liquid or solid surfaces is a subject having been studied for decades, not only because of numerous physical phenomena of fundamental interest involved, but also due to its strong relevance to many industrial applications, such as ink-jet printing, micro-fabrication, spray cooling and painting, self-cleaning, coating manufacturing [see, e.g., 23, 33, 54, 96, 105, 107]. Having a understanding of the physics of a droplet's impact and predicting or controlling its outcome, is a major challenge in fluid mechanics. This present project is financially supported by LabEx MMCD (Modélisation et Expérimentation Multi-Échelle de Matériaux pour la Construction Durable), under Axe 2, to study the manufacturing of thin metallic or ceramic coatings by liquid droplets impacting on a target surface, as for example plasma spraying [see, e.g., 89, 90, 91, 20, 53, 54, 60, 103, 104, 106]. Under this current project, inquiring about the detailed mechanism and physics behind these physical phenomena of liquid droplet impact is of utmost significance in applying dependable initial or boundary conditions required in numerical codes or making reliable assumptions in theoretical analysis for plasma spray simulations to obtain high-quality coatings. This process is very promising for building applications in order to provide new properties to existing structures, such as to provide thermal or chemical barriers or mechanical reinforcements to the glass or iron structures in buildings. When considering the plasma spray application, the corresponding investigations could be divided into three groups according to difference simulation regions, the first one region is in the creator of plasma, the second one is in the plasma spray, the region where the

turbulence takes place and the third one the region on the target surface, in which the droplets deform, spread, and solidify.

The history of investigating the droplet impact phenomenon dates back to Worthington [114], who firstly photographed water droplets impinging on a solid surface and revealed the complex shapes as droplets spread and splash after impact. Thanks to the development of the high-velocity imaging technique [95] and high performance computing [28], droplet impact has been an intensive subject of research since Worthington [114]. Two influential reviews on droplet impact could be referred [see, e.g., 46, 116]. However, besides the numerous works on droplet impact, this subject still lacks a comprehensive understanding and continues to attract researchers' attention. The widely diverse accompanying phenomena after droplets' impaction are jointly determined by the liquid properties, the initial impact condition, and the physical properties of the target surfaces.

Despite all the interesting accompanying phenomena after droplets' impaction under diverse conditions, the topic attracts us is the simulations of Newtonian droplets impacting on solid surfaces, related to the applications spray cooling and coating manufacturing. With Computational Fluid Dynamics (CFD) tools, the multiple droplets' impaction, interaction and solidifications could be captured [see, e.g., 54]. And the droplets' impaction may be oblique or perpendicular to the target surface. The microstructure and physical properties of a sprayed coating are determined by the dynamics of the deformation of the droplets impacting on the substrate, the solidification rates, and the droplet-droplet interactions [see, e.g., 65, 70, 101, 29]. Apart from the complex droplet-droplet interaction in spray impaction [54], the studies of single droplet impingement are essential to understanding the relational character of spray impaction, providing sights on the influences of the hydrodynamics of impact on the thickness of the lamella, the air entrapment, and consequently the quality of contact [see, e.g., 27, 67, 69]. More specially, our work focus on the single droplet's normal isothermal impaction on dry smooth rigid surfaces in air without phase change to inquire about the fundamental understanding of the droplet impact phenomena to optimise the efficiency of associated applications and for example to control the appearance of the microstructure in the coating.

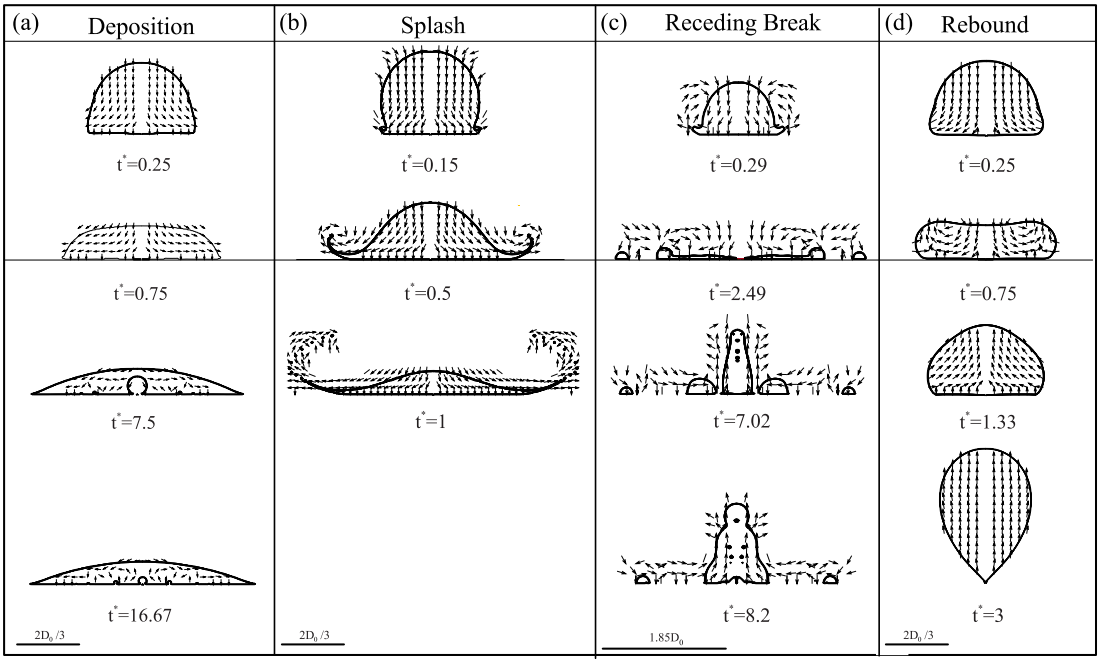

FIGURE **1.1**: Different dynamics and outcomes after droplets' impact on solid surfaces. (a) Molten ceramic, $We = 4.275$, $Re = 14.25$, $\theta = 30°$; (b) Molten ceramic, $We = 3847.5$, $Re = 427.5$, $\theta = 120°$; (c) Water, $We = 46$, $Re = 2129$, $\theta = 96°$; (d) Molten ceramic, $We = 4.275$, $Re = 14.25$, $\theta = 135°$.

In the research of this kind droplet impaction, the early studies of the impact process were mostly focused on the phenomena in nature, identifying the most important parameters influencing the spreading of the liquid lamella on the surface and the final outcome of the droplet's impaction [41, 59, 78]. More recent studies have attempted to quantify the influences of various parameters in order to predict the dynamics of the droplet. In particular, thin coatings can be obtained on surfaces by spray coating and spray painting [see, e.g., 18, 4, 54]; the fundamental understanding of the droplet impact phenomenon is essential.

Some physically important phenomena can be exhibited by a droplet impacting on a solid substrate, such as deposition, rebound, partial recoil and splashing [see, e.g., 81], illustrated with our simulations in Fig.1.1. The dynamics and outcomes of the impacting droplet is influenced by its material properties (density, viscosity and surface tension), impact velocity, droplet diameter and the physicochemical properties of the solid surface. Splashing is resulted from the breakup of a thin liquid lamella which breaks through the droplet's surface and is ejected ra-

dially along the surface [see, e.g., 62, 61, 115]. The spreading behaviour, characterised by the spread factor ξ, has been investigated extensively [see, e.g., 16, 78, 38, 6, 116, 11, 46]. In this work, considering the balance between gravity and surface tension through Bond number $Bo = \rho g D_0^2/\sigma$, we can show that gravity is negligible. Under usual impact conditions, we find that $Bo \ll 1$ so that only three dimensionless parameters are needed for describing the impact dynamics. The major dimensionless parameters characterising the droplet impact are

$$We = \frac{\rho R_0 V_0^2}{\sigma}, \qquad Re = \frac{\rho R_0 V_0}{\mu}, \qquad Oh = \frac{We^{1/2}}{Re},$$

and

$$\xi = \frac{D}{D_0},\ t^* = \frac{tV_0}{D_0},\ \xi_{\max} = \frac{D_{\max}}{D_0},$$

with ξ the dimensionless diameter of the droplet during the impact, t^* the dimensionless time and ξ_{max} the dimensionless maximum diameter of the droplet over time. Recall that the Weber number We measures the relative importance of kinetic energy compared to surface energy of the droplet, while the Reynolds number Re, is defined as the ratio of inertial forces to viscous forces, quantifying the relative importance between them for given flow conditions. A large Weber number has the consequence that the droplet spreads to a maximum radius much greater than its initial value, occupying a large surface area. A large Reynolds number implies that viscous effects are confined to a thin boundary layer close to the solid surface.

Due to the small time and space scales in this study (ranges of μs and μm for ceramic droplet spreading), it is difficult to measure the parameters governing the spreading. The numerical simulation of two-phase flows is of interest for numerous fundamental and applied researches in fluid mechanics applied to material selection, surface treatment, energy production in industrial processes. The unsteadiness and complex optical properties make the experimental measurements difficult to be accurate. Among the wide variety of physical approaches, there exists two main fundamental modelling approaches based on microscopic considerations and continuous fluid mechanics, respectively. Molecular dynamics of multiphase flows integrate molecular interfacial forces into continuous models [43]. The models based on continuous fluid mechanics are the most commonly used in academic and industrial Computational Fluid Dynamics (CFD) tools, which are built by integrating the Navier-Stokes equations in each phase and by defining jump relations at the interface to ensure mass and momentum conservation [21].

1.2 Literature Review

A deep understanding of the physics controlling the dynamics and solidifications of liquid droplets (molten or natural) on a solid surface is of importance in the development of applications related to plasma spray. Based on experiments on the impact and solidification of motel wax droplets on aluminium, Bhola and Chandra [7] observed that the droplet solidifications barely affected the dynamics after droplet impact. After studying the deposition of nickel particles after impacting on a stainless steel surface by plasma spray experimentally and numerically, [73] concluded that splashing could be triggered by the solidification inside a spreading droplet, also by other obstacles on the test surface, for example the previously deposited splats. They also found that the temperature of the target surface has a considerable impact on the outcomes of droplet impact, Nickel particles would splash if the temperature of the substrate is below $300°C$ and deform into a round disk on substrates with temperature higher than $400°C$.

Rioboo *et al.* [81] experimentally showed that for droplets impacting on wetting surfaces, the deposition could be divided into two stages: the kinematic stage and the actual deposition. They concluded that the spreading radius in this kinematic stage (for $t^* \leq 0.1$) is independent of the physical properties of the liquid and the wall and, therefore, the obtained description of the spreading radius should be general. The spreading diameter becomes dependent on the parameters in the deposition stage. Kobayashi *et al.* [51] investigated nano-droplet spreading at the early stage after the impact by molecular dynamics simulations. They found that at the early stage of the nano-droplet impact, the spread factor of the droplet is proportional to the square root of a dimensionless time t^* $(= tV_0/D_0)$:

$$\xi \sim \sqrt{t^*}.$$

Roisman *et al.* [84] concluded that with high Weber and Reynolds number, the thickness, velocity distribution and pressure distribution of the lamella ejected from the droplet barely depend on the impact conditions. Their theoretical results show that the dissipation mainly takes place in the viscous boundary layer, and only has influence on the lamella thickness at the late stages of spreading.

Considering the splash after droplet impact, Stow and Hadfield [86] observed that the splashing would occur when the splash parameter $K = We^{1/2}Re^{1/4}$ exceeds a critical value, whose value is dependent on the roughness of the solid surface. Jian *et al.* [44] numerically distinguished

two different splashing mechanisms, which depends on whether a jet is created before or after the impacting droplet spreads on the substrate. They also highlight the important gas effect on the dynamics is due to its viscosity through the thin gas film beneath the droplet.

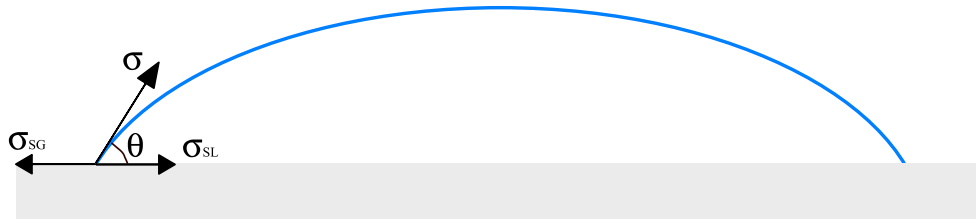

FIGURE **1.2**: Two-dimensional representation of a droplet on substrate describing interfacial tensions.

The wettability of solid materials is an important issue in surface engineering, and has a key impact on the dynamics of droplet impact. Generally speaking, there are two extreme limits. The first is complete wetting where liquid would spread into a film when it is in contact with a solid. The other limit is complete nonwetting. On a complete nonwetting solid surface, liquid droplet remain spherical without further spreading. The parameters used to characterise the wettability could be the surface tension, which reflects the cohesion between phases. The geometric shape of a droplet resting on a substrate is determined by several factors: the liquid properties, the gas atmosphere around, and the target substrate. This could be described by Young equation [118] in terms of interfacial tensions,

$$\sigma cos\theta = \sigma_{SG} - \sigma_{SL}, \tag{1.1}$$

where σ_{SG} is the interface energy per unit area or force per unit length of solid/gas interface, σ_{SL} the tension of solid/liquid interface. The liquid/gas interface energy is simply denoted as σ. The influence of wettability was first investigated by Hartley and Brunskill [37] who showed its effects on droplet rebounding after impact onto leaves. They proposed an energy balance approach for the spreading lamella considering wettability through a static contact angle. The experiments and theoretical analysis by Fukai *et al.* [30] indicate the wettability significantly affects all stages of the spreading process. Antonini *et al.* [1] investigated the effects of wettability on the spread behaviour of droplet impact onto hydrophilic and hydrophobic surfaces under moderate and high Weber number regimes. For moderate Weber ($We < 200$), droplet maximum spread factor and spreading time are both influenced by wettability; for high Weber

number ($We > 200$), inertial effects become predominant over capillary one and the influence of wettability is negligible during spreading. When a droplet impacts onto a solid surface, the air film between the droplet and substrate would evolve into a spherical bubble due to minimisation of surface energy. The formation of air entrapment was investigated analytically by Duchemin and Josserand [24] and experimentally by Thoroddsen *et al.* [98], San *et al.* [87] and de Ruiter *et al.* [22].

1.2.1 Maximum Spreading Diameter

After the initial stage of spreading, the droplet continues to spread until reaching its maximum spread extent. Then, depending on the surface properties, the liquid can recoil or stay close to the maximum spreading diameter. The maximum spread factor $\xi_{max}$is defined as the ratio of the largest lamella radius at the wall to the initial droplet one. The dynamic behaviour of spreading in droplet impingement has been extensively investigated though experimentation, theoretical analysis, and numerical simulations.

Using the energy and momentum conservation equations, a large number of theoretical models have been proposed to predict the maximum factor, using different arguments and sometime arriving at very different conclusions [see, e.g., 59, 16, 72, 17]. Based on the momentum conservation, Clanet *et al.* [17] proposed a scaling that the maximum spreading factor scales with $We^{1/4}$ in the regime of low viscosity and low wettability (water droplet on a super-hydrophobic surface).

Based on the energy balance of a droplet impacting on a solid surface, the kinetic energy, the surface energy and the viscous dissipation have to be taken into consideration. In practice and in numerical simulations, the difference in gravitational potential energy between two states is assumed to be negligible, and the kinetic energy is assumed to be zero at the maximum spreading state. At the state prior to impact, the initial kinetic energy of droplet reads as $E_0^K \sim \rho V_0^2 D_0^3$. And according to Madejski [59] and Collings *et al.* [18], the viscous dissipation takes the form $W_{max} \sim \mu V_0 D_{max}^5 / D_0^3$ whereas the capillary energy can be written as $E_{max}^S \sim \sigma D_{max}^2$ at the maximum spreading state. Studies distinguish two main regimes [17, 26], the capillary regime where the viscous dissipation could be neglected so the capillary forces determines ξ_{max}, the other one where the viscous forces play the dominating role in countering the spreading then ξ_{max} is determined by the balance between inertial energy and viscous dissipation. In

the capillary limit, the kinetic energy is transformed into capillary energy (still considering the viscous dissipation in the boundary layer), $E_0^K \sim E_{max}^S$, then the maximum spreading factor scales as

$$\xi_{max} \sim We^{1/2}, \tag{1.2}$$

which is also found by Collings *et al.* [18]. In the viscous regime, the initial kinetic energy is almost lost to the dissipation work, $E_0^K \sim W_{max}$. In that case, the maximum spreading factor is obtained as

$$\xi_{max} \sim Re^{1/5}, \tag{1.3}$$

which is again observed by Madejski [59] and Roisman *et al.* [82]. Based on the assumptions that the splat shapes as a disk and $t_{max} = 8D_0/3V_0$, Pasandideh-Fard *et al.* [72] found a scaling as $\xi_{max} \sim Re^{1/4}$ by taking the initial kinetic energy and surface energy, the surface energy and the dissipation work at maximum spreading into consideration. Most of these models focused on the estimation of viscous dissipation and surface free energy. The correctness of these estimations can be verified in particular on the basis of their ability to predict the maximum spreading factor. This factor is necessary to describe the droplet deformation because it not only guides the design of coating devices but also reveals energy conversion, such as viscous dissipation. Laan *et al.* [52] interpolated between these two scaling models to allow for a universal scaling. The fact that no clear dependency on We or Re is found suggests that all three forces mentioned above (inertia, capillarity, and viscosity) are important. The approach proposed by Eggers *et al.* [26], completed by Laan *et al.* [52], interpolated between $We^{1/2}$ and $Re^{1/5}$ scalings by using

$$\xi_{max} \sim Re^{1/5} f_{EC}(WeRe^{-2/5}),$$

where f_{EC} is a function of the parameter $WeRe^{-2/5}$ that varies between zero (capillary regime) and infinity (viscous regime). This interpolation between two regimes corrected that all three energy components are vital in most situations, the spreading dynamics of droplet can not be predicted by neglecting the relatively minor energy component.

Further, Lee *et al.* [57] investigated the maximum spreading factor of droplets impacting on wetting/non-wetting, smooth/rough surfaces at low velocities to high velocities. To account the influences of dynamic contact angle at low velocity, they correct the measured maximum

spreading factor ξ_{max} by the spreading factor at zero velocity $\xi^2_{V_0\to 0}$ as

$$\sqrt{\xi^2_{max} - \xi^2_{V_0\to 0}} \sim Re^{1/5} f(We). \tag{1.4}$$

As mentioned above, all three energy components are important in the theoretical models predicting the maximum spreading diameter. The spreading time, which is used to calculate the dissipation work accumulated at maximum spreading state, has a considerable impact on predicting the maximum spreading diameter. Chandra and Avedisian [16] equals the maximum spreading time to D_0/V_0 as the height of the droplet decreases to zero. Pasandideh-Fard *et al.* [72] obtains an equation that $t_{max} = 8D_0/3V_0$ based on a disk-shape assumption. As more experimental works are conducted, these two equations become unphysical by regarding the maximum spreading time only depends on initial diameter and impact velocity. Based on experimental results, Lee *et al.* [56] introduced ξ_{max} into the prediction model of t_{max} to replace the initial diameter and considered the influences of surface tension as,

$$t_{max} = D_{max}/V_0 \cdot b, \tag{1.5}$$

where b is the ratio of liquid droplet's surface tension to water's surface tension and this prediction provides better predictions of ξ_{max}, as well as in the work of Huang and Chen [40].

1.2.2 Retraction Dynamics

The retraction starts from the droplets' maximum spreading state, until the droplets sit on the surface with certain deposition or the droplets rebound off the surfaces. Clanet *et al.* [17] observed vortical motion in the low-viscosity droplet at the maximum spreading state. This residual flow in the droplet proves that the initial kinetic energy is not all converted and is still available. While this remaining kinetic energy could be neglected compared to other energy components at the initial state and the maximum spreading state, it can not be assumed as vanished in the retraction analysis as most of the initial energy is dissipated in the spreading.
Kim and Chun [48] used the energy balance along with an assumption that using a cylinder or truncated-sphere to approximate the droplet shape throughout the impact process, aiming to develop an analytical model of the droplet rebound. In the model by Kim and Chun [48] adopted an empirically determined factor to estimate the viscous friction. They conclude that the cylinder model predicts the droplet retraction dynamics approximately when $Oh < 0.002$

and truncated-sphere model for $Oh > 0.006$. Okumura *et al.* [71] employed scaling arguments to characterise the droplets' oscillation on superhydrophobic surfaces as a spring-mass system in the limit of high restitution (small deformation). Under the topic of droplet's normal impact on solid surface, the restitution coefficient ϵ is the ratio of the rebound velocity V_{BC} to initial impact velocity V_0, or related to the kinetic energy,

$$\epsilon = \frac{V_{BC}}{V_0}, \qquad \epsilon = \frac{E^K_{BC}}{E^K_0}, \tag{1.6}$$

where E^K_0 is the initial kinetic energy of the droplet, and E^K_{BC} is the droplet's kinetic energy at bouncing-off instant. With experiments of liquid droplets impacting on hydrophobic surfaces at high velocity, Bartolo *et al.* [8] introduced the retraction rate ($= max[\dot{D(t)}/D_{max}]$) and showed that the droplet retraction rate does not depend on the impact velocity ($We > 10, Re > 10$), only determined by the physical properties of the liquid droplet. Based on the retraction rate, Bartolo *et al.* [8] observed two regimes for retraction dynamics, the capillary-inertial regime and the capillary-viscous regime. In the capillary-inertial regime, the retraction rate does not depend on the impact speed. While with the increase of viscosity, typically $Oh > 0.05$, in the capillary-viscous regime, the retraction rate decreases strongly as the capillary forces and the viscous forces govern the retraction dynamics.

The retraction ending with total rebound is usually observed on superhydrophobic surfaces. The superhydrophobic surfaces are attributed to the surfaces with large contact angles ($\theta > 150°$) and small contact angle hysteresis ($\theta_{adv} - \theta_{rec} < 10°$). Mao *et al.* [64] investigated the liquid droplets' impactions on surfaces with equilibrium contact angles ranging from $37° < \theta < 97°$ experimentally and set a rebound energy criterion based on the energy conservation,

$$E^*_{ERE} = \frac{1}{4}\xi^2_{max}(1 - cos\theta) - 0.12\xi^{2.3}_{max}(1 - cos\theta)^{0.63} + \frac{2}{3}\xi_{max} - 1, \tag{1.7}$$

the droplet would rebound from the surface when $E^*_{ERE} > 0$, otherwise, the droplet remains in contact with the surface. Based on Eq.(1.7), Mao *et al.* [64] deduced that the droplet can rebound when the equilibrium contact angle is larger than $90°$ and larger contact angle and larger maximum spreading factor increases the droplet's rebounding tendency. Antonini *et al.* [2] concluded that the impacting droplets can have the rebound outcome only on surfaces with receding contact angle greater than $100°$ and the contact time decreases with the increase of receding contact angle.

The time that the droplet stays in contact with target surface before the first bouncing-off is defined as the contact time t_c in our work. Richard *et al.* [80] and Okumura *et al.* [71] found that the droplet's contact time on superhydrophobic surface is independent of the impact velocity, and scales as a function of the droplet's mass, surface tension,

$$t_c = 2.6 \left(\frac{\rho D_0^3}{8\sigma} \right)^{1/2}. \tag{1.8}$$

Note that the retractions in the works by Richard *et al.* [80] and Okumura *et al.* [71] are in the capillary-inertial regime, in which the impact is mainly inertial and the restitution coefficient ϵ reaches 0.91. To reduce the contact time, besides utilising the Eq.(1.8), Weisensee *et al.* [111] investigated droplets' impact onto elastic superhydrophobic surfaces experimentally. They found that droplets rebounded off the surface with shorter contact time as the vertical momentum provided by the elastic surfaces to the droplets. Further, in the work by Weisensee *et al.* [110], it is concluded that the contact time t_c, which shows no independence on the impact velocity on rigid stationary substrates, can be actively controlled through substrate vibration ($60 - 320\ Hz$). And lots of work are dedicated to texturing the target surface to achieve shorter contact time [see e.g., 58, 14, 31, 79]. Impacting onto micro-patterned surfaces, the capillary energy stored in the liquid penetrating between pillars promotes the lift of the drop.

1.3 Introduction of Numerical Code Thetis

Besides the analytical modelling and experimental scaling, numbers of works are conducted on numerical simulation of droplet spreading on dry, wettable surfaces. Based on the finite element method, Fukai *et al.* [30] solved the Navier-Stokes equations with unstructured grids adapting in time to the deformations of the impacting droplet. Pasandideh-Fard *et al.* [72] used the Volume-Of-Fluid method to describe the spreading dynamics on a dry smooth surface with constant or variable measured contact angle applied at the contact line.

The simulation tool used in this thesis is based on the Computational Fluid Dynamic library Thetis, developed initially by J.-P Caltagirone, S. Vincent and S. Glockner at I2M Institute, Bordeaux. The approximations of the conservation equations are based on fixed staggered regular Cartesian meshes first introduced by Harlow and Wekch [42]. The Navier-Stokes equations are discretised with an implicit finite volume technique and centred schemes. For the pressure-

velocity coupling, an augmented Lagrangian approach is used as well as an Adams-Bashforth scheme for the linearisation of the non-linear inertial term in the momentum equations. The advection of the VOF function is approximated by a Lagrangian geometric Piecewise Linear Interface Construction (PLIC). All the details of numerical methods are given in previous publications [see, e.g., 119, 103, 105, 107], together with numerous validations [60, 54, 108].

The modelling and simulation of two-phase flows involving separated phases are achieved by introducing the Navier-Stokes equations in each phase and by imposing appropriate jump conditions on the velocity and stress fields [21]. A unified flow model valid in all phases and at the surface is used in this work. Our modelling framework is limited to non-miscible, incompressible and isothermal flows. Moreover, a constant surface tension coefficient is assumed. The required jump equations valid at the interface are integrated in the 1-fluid model by convolving the single phase conservation equations with a phase function C describing the interface evolutions over time through a material advection equation. As shown in Fig.1.3, this function C is assumed to behave like a Heaviside function as:

$$C\left(\mathbf{x},t\right)=\begin{cases}1 & \text{if } x\in \text{ phase } k=1,\\ 0 & \text{if } x\in \text{ phase } k=0,\end{cases} \tag{1.9}$$

where $k=1$ for the liquid phase and $k=0$ for the gas phase. The interface between these two phases is assumed to be sharp and defined by the isosurface $C=0.5$ (Gibbs discontinuous representation of an interface).

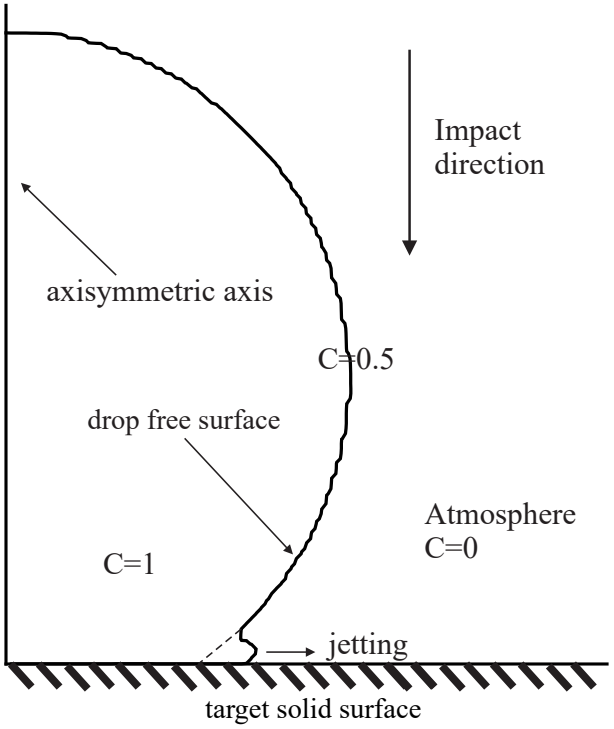

FIGURE **1.3**: Sketch of a droplet impacting on a solid surface according to the 1-fluid model.

With this phase function C, local quantities, such as the density ρ and the dynamic viscosity μ, are defined by numerical mixture laws:

$$\rho = C\rho_1 + (1 - C)\,\rho_0, \tag{1.10}$$

$$\mu = C\mu_1 + (1 - C)\,\mu_0. \tag{1.11}$$

Using these definitions, a set of Navier-Stokes equations for a two-phase flow is designed in the framework of the 1-fluid model [47]:

$$\rho\left(\frac{\partial \mathbf{u}}{\partial t} + \mathbf{u}\cdot\nabla\mathbf{u}\right) = -\nabla p + \rho\mathbf{g} + \nabla\cdot\left(\mu\left[\nabla\mathbf{u} + \nabla^T\mathbf{u}\right]\right) + \mathbf{F}_{ST}, \tag{1.12}$$

$$\nabla\cdot\mathbf{u} = 0, \tag{1.13}$$

$$\frac{\partial C}{\partial t} + \mathbf{u}\cdot\nabla C = 0, \tag{1.14}$$

where $\mathbf{F}_{ST}$ represents the force associated to the interfacial energy between air and droplet due to the surface tension depending on the interface location. This force is modelled by a continuum surface force (CSF) approach based on the work of Brackbill *et al.* [13]:

$$\mathbf{F}_{ST}\left(C\right) = \sigma\kappa\mathbf{n}\delta_i = \sigma\nabla\cdot\left(\frac{\nabla C}{\|\nabla C\|}\right)\nabla C \tag{1.15}$$

with κ the local curvature of the interface, $\mathbf{n}$ the local unit normal to the interface and δ_i a Dirac function indicating interface. Eq.(1.14) means that the phase function is advected with the local fluid velocity $\mathbf{u}$, and consequently, the evolution of both phases is known at each physical time and at each position in the calculation domain. Moreover, the Navier-Stokes equations (1.12) and the advection equation (1.14) are coupled by considering the term $\mathbf{F}_{ST}$ in the momentum equation. The boundary conditions for the momentum equations are symmetry conditions on all sides of the simulation domain except at the bottom boundary where a Dirichlet condition with zero velocity, *i.e.* a no-slip condition, is considered. No phase change is considered in the present work nor heat transfers.

In Eq.(1.15), deducing the curvature requires the approximation of second order partial derivatives of the VOF function, whose gradients are restricted to one numerical control volume (a mesh cell). We utilise the Smooth-VOF technique introducing an auxiliary smooth function C_S, proposed by Guillaument *et al.* [36], to estimate the curvature and the normal to the interface required in Eq.(1.15). This approach can be compared to the height functions proposed by Popinet [74] to calculate the local interface curvature on a discrete level. The interface location, $C = 0.5$, is verified in the same cells in which $C_S = 0.5$. The averaging procedures of equations (1.10) and (1.11), based on the unsteady diffusion equation for scalar concentration transfers take the following form

$$-\nabla \cdot D_c \nabla C_S^{n+1} + C_S^{n+1} = C_S^n, \tag{1.16}$$

with a source term initially equal to the sharp VOF function C. Here the diffusion coefficient D_c equals to $L_i \Delta h^2$ and is used to make the VOF function C_S spread on a distance L_i on each side of the interface $C = 0.5$. Then the surface tension force will be modelled as,

$$\mathbf{F}_{ST}\left(C_S\right) = \sigma \nabla \cdot \left(\frac{\nabla C_S}{\|\nabla C_S\|} \right) \nabla C_S. \tag{1.17}$$

A penalty term is added in the VOF smoothing equation in order to account for wetting effects, as previously proposed by Guillaument *et al.* [36]. It takes the form of the following Helmholtz equation:

$$-\nabla \cdot D_c \nabla C_S^{n+1} + C_S^{n+1} + B_S(C_S^{n+1} - C_S) = C_S^n, \tag{1.18}$$

with B_S a penalty parameter [36]. When B_S tends to zero, the standard smooth VOF equation is recovered. For large values of B_S, we obtain $C_S^{n+1} = C_S$. In addition, $C\left(\theta\right)$ is defined as the

values to be imposed on C_S in mixed fluid/solid cells so as to satisfy the physical contact angle. It reads

$$C(\theta) = 0.5\left[-\tanh\left(0.025\left(\theta - 90\right)\right) + 1\right], \tag{1.19}$$

this relation is obtained from simulations in which the impacting droplet has no initial velocity and holds in a wide range of $15° \leq \theta \leq 170°$. This contact angle θ could be seen as the static contact angle.

1.4 Computational Treatment

The axisymmetric numerical simulations are carried out to validate the model used in this work in a first step and also to investigate in second step a wide range of parameters concerning the effects of impact velocity and wettability on early spreading stages after the impact. These simulations involve two types of liquids in the droplet, water and molten ceramic. The first one is chosen as it is widely used in experiments and the second fluid is chosen as representative of coating process materials. The simulations using water droplet are carried out to validate our simulation with experiments in the literature while the molten ceramic droplet is chosen for industrial applications.

1.4.1 Energy Calculation

In this work, the changes in the initial energy (initial surface and kinetic energy) and the transformation in viscous dissipation energy will be analysed. The kinetic energy per unit volume in the droplet is given by

$$E^K = \frac{1}{2}\rho \cdot |\mathbf{u}|^2 \tag{1.20}$$

The viscous dissipation function utilized is defined by,

$$\phi = \frac{\mu}{2}\left(\frac{\partial \mathbf{u}_y}{\partial x} + \frac{\partial \mathbf{u}_x}{\partial y}\right)^2. \tag{1.21}$$

The accumulated viscous dissipation within an impacting droplet is calculated as

$$W = \int_0^t \int_\Omega \phi d\Omega dt, \tag{1.22}$$

where Ω is the volume in which viscous dissipation occurs and t is the time from impact.

1.4.2 Validation of Computational Model

In the first validation, the simulations are designed to be compared with the experimental study by Šikalo *et al.* [88], in which three liquids and four kinds of surfaces with varied wettability were used to analyse the impact of droplets on horizontal solid surfaces. The simulations considers the water as the liquid of the droplet and sets the impact velocity V_0 at $1.17\ m/s$. The water droplet is of diameter $2.7\ mm$, with density $\rho = 998\ m/s$, surface tension $\sigma = 0.073$ and dynamic viscosity $\mu = 0.001\ Pa \cdot s$. The calculation domain is set as $3mm \times 10mm$ including 150×500 stagger grids. The time step is set as $\Delta t = 0.5e-5\ s$, smaller than $\Delta x/2V_0$. A gird dependence test has been performed that finer mesh or smller calculation time step would not present better results. Four kinds of surfaces (smooth glass, rough glass, smooth PVC and wax) are utilised for their characteristic wettability. The majority of investigations in literature employ the static contact angle at the three-phase contact line. As indicated in the work of Šikalo *et al.* [88], the dynamics after the impact of the droplet are mainly spreading. The advancing contact angles are adopted here for the solid boundary condition instead of the static contact angle. While the work of Šikalo *et al.* [88] does not provide equilibrium contact angle, then the correlation between equilibrium contact and advancing, receding contact angle by [97] is used. Based on the theoretical work by Tadmor [97], the equilibrium contact angle θ could be calculated from the advancing and receding contact angles θ_{adv} and θ_{rec},

$$\theta = arccos\left(\frac{r_{adv}cos\theta_{adv} + r_{rec}cos\theta_{rec}}{r_{adv} + r_{rec}}\right) \tag{1.23}$$

with

$$r_{adv} = \left(\frac{sin^3\theta_{adv}}{2 - 3cos\theta_{adv} + cos^3\theta_{adv}}\right)^{1/3}, \qquad r_{rec} = \left(\frac{sin^3\theta_{rec}}{2 - 3cos\theta_{rec} + cos^3\theta_{rec}}\right)^{1/3},$$

this relation has been validated with the experiments by Chibowski and Terpilowski [19]. With the advancing and receding contact angles of water on different surfaces presented by Šikalo *et al.* [88], the corresponding equilibrium contact angles can be calculated by the results of Tadmor [97] and listed in Table.1.1.

As presented in Fig.1.5, the results obtained by simulations with advancing contact angles θ_{adv} provide better coincidence with the experimental results by Šikalo *et al.* [88] than those calculated with a static contact angle θ. This could be explained as the droplet only spreads along the dry target surface in the chosen configurations. The numerical code Thesis is working nicely

TABLEAU **1.1**: Equilibrium contact angles calculated from Šikalo *et al.* [88]

	Advancing	Receding	Calculated [97]
Smooth glass θ	10°	6°	8.077°
Rough glass θ	78°	16°	45.377°
Smooth wax θ	105°	95°	99.72°
Smooth PVC θ	83°	53°	67°

for all the contact angles except for the more wetting case ($\theta = 10^\circ$) after $t^* > 1$, and we have discrepancy between the simulation results and the experimental ones in Fig.1.5 (a). This is because that the contact angle model Eq.(1.19) is only valid in the range of $15^\circ \leq \theta \leq 170^\circ$. The phenomenon that the discrepancy becomes larger with time could be explained as the influence of contact angle could be neglected in the early spreading. Nevertheless, through this comparison, the numerical code Thesis is validated, besides the fact that numerous validations have been provided in literature [60, 54, 108].

For the simulations of ceramic droplet ($D_0 = 30\ \mu m$) impact conducted in the present thesis, a grid dependence of the spread factor ξ and dimensionless axial height h^* for these simulations is presented in Fig.1.4. It is observed that a convergence of the simulations is obtained for the mesh arranged as 250×500 in the calculation domain of dimension $50\mu m \times 100\mu m$, i.e., we arrange 75 unit grids in the length of R_0. These grid dependence tests sets the mesh size criterion for all the simulations that are considered in the rest of the present work, the dimension of the simulation region could be altered with arranging at least 75 unit grids per initial radius and the thickness of thin lamella is of at least 20 unit grid length.

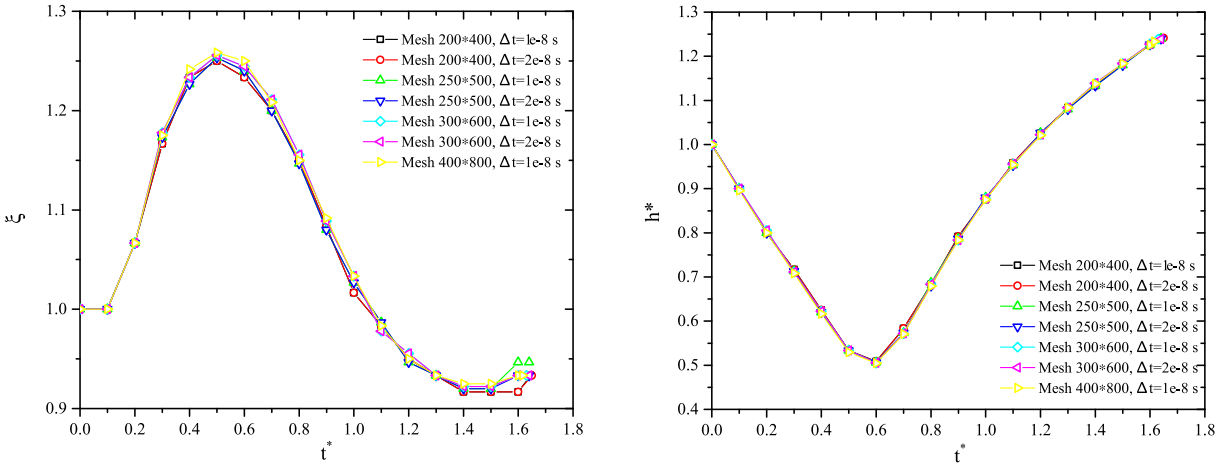

FIGURE **1.4**: The grid dependence of the evolution of the spread factor ξ of a molten ceramic droplet impacting at $V_0 = 20m/s$ on the surface with contact angle $\theta = 90°$.

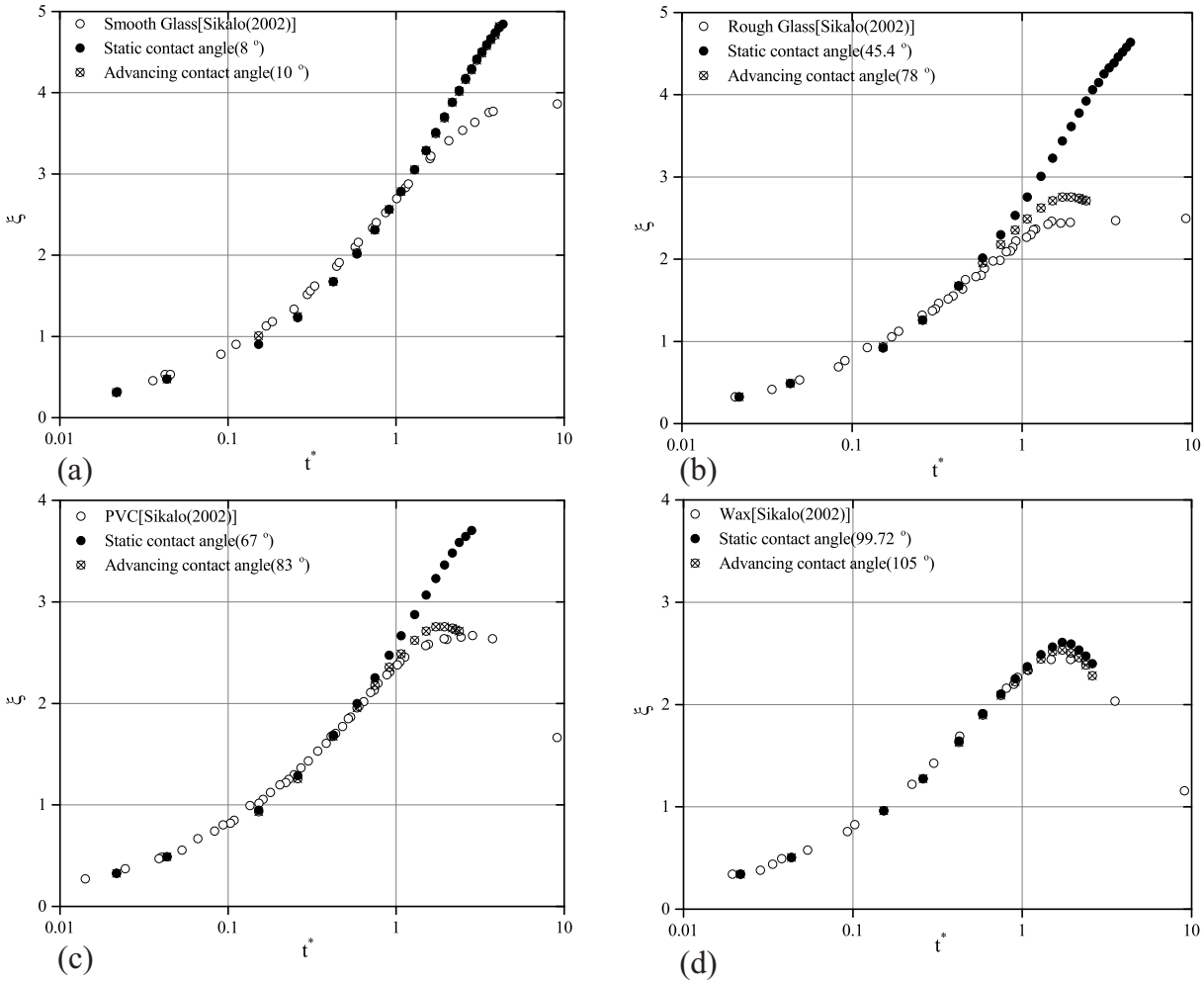

FIGURE **1.5**: Numerical simulations of the spread of a water droplet with the parameters of Šikalo *et al.* [88], $D_0 = 2.7mm, V_0 = 1.17m/s, We = 50$. (a) on a smooth glass surface, (b) on a rough glass surface, (c) on a PVC surface, (d) on a wax surface.

1.5 Motivations

In this chapter, we have discussed the different dynamics and outcomes of liquid droplets' impaction on solid surface due to the variations of liquid properties and impact conditions. After validating our numerical code Thetis to available experimental results, we can easily vary the liquid properties, impact conditions in a systematical way to investigate the droplets' dynamics, such as the time-evolving diameter and the variations of energy components, which are hard or impossible to obtain from experiments.

Based on the mentioned studies on liquid droplets' dynamics after impacting on dry solid sur-

faces, we start our work with investigations on the early spreading dynamics. One of the important aspects in the early spreading stage is the jetting time, as the jetting lamella affects the droplets' dynamics on target surface, and the contact mechanism between them when taking heat transfer and solidification into consideration.

Indeed, the maximum spreading diameter of the liquid droplets impacting on solid surfaces have been extensively and thoroughly studied by considering the influences of impact velocity, surface tension, viscosity, wettability and roughness. The majority of these studies are on the wetting surfaces or surfaces with contact angle smaller than $150°$, where the spreading diameter could be approximately regarded as the real contact diameter between the droplet and surface. While on super-hydrophobic surfaces, the rim radius becomes larger and the spreading diameter could no longer be taken as the real contact diameter, especially at low impact velocities. To our knowledge, only few studies take the influences of wettability at low impact velocity into consideration by eliminating the diameter spread at zero impact velocity from the maximum spreading diameter. Our strategy is to measure the maximum contact diameter of droplets impacting on superhydrophobic surfaces and study the influence of liquid properties and impact conditions on the difference between maximum spreading diameter and maximum contact diameter. Meanwhile, the maximum spreading time should also be put under investigation. Considering the molten ceramic or metal droplets, the solidification inside the droplet would triggers the droplet for splashing or figering. Pasandideh-Fard *et al.* [73] pointed out that a molten droplet would not splash when the droplet spreads completely before solidification. Although there exist numbers of studies on droplets' maximum spreading state, few of them studies the spreading time. The spreading time could have a large impact on the estimation of dissipation work accumulated, which usually affects the energy conversion largely during spreading. The available models on maximum spreading time are based on simple geometric assumptions, which lack the necessary accuracy and need to be improved. We expect to obtain a correlation between maximum spreading diameter and maximum spreading time and validate it with available experimental results.

As mentioned, the contact time for the droplet in contact with the target surface, has a considerable impact on the heat and mass transfer between the droplet and substrate. However, the works studying the contact time focus on texturing and micro-patterning the target surface to make the surfaces approaching the purely non-wetting limit $\theta = 170°$. Fewer studies have

investigated the contact time of liquid droplets impacting on numerically purely non-wetting surfaces. Only several studies conduct investigations on the influences of liquid properties and impact conditions on contact time within a regime where the restitution coefficient $\epsilon \to 1$, i.e., there is nearly no spreading dynamics during the contact time. As there exists a regime for impacting droplets to spread and rebound, where the dissipation work could affect the contact time considerately. Our idea is to study the contact time in the regimes from high to low restitution coefficient and expect to obtain a smooth cross-over between these two regimes. To this purpose, the liquid properties and impact conditions are varied to make the droplets' outcomes sit between partial recoil and total rebound with secondary droplet appearing at the top of the droplet. In the meantime, the contact angle will be varied from $90°$ to $170°$. The retraction time for the droplet to recoil from maximum spreading to total rebound will also be studied.

Lastly, the energetic analysis on droplets' dynamics is important to find the dominating forces and distinguish different regimes during spreading and retraction stage, and at droplets' maximum spreading state and bouncing-off instant. Thus, the time-evolving variations of three energy components will be presented, along with suppressing the their individual ratios to the driving energy.

This manuscript is divided in six chapters.

Chapter 1 discusses the fundamental and background of droplets' impaction. We demonstrate the droplets' dynamics and outcomes after impacting on liquid or solid surfaces. We introduce the different outcomes of droplets' impaction, along with their major applications and impact conditions. We compare different commonly used numerical methods for simulating the dynamics of droplets after impaction. We present a brief introduction on the major parameters dominating the droplets' dynamics in different stage. Then we narrowed down to the droplets' maximum spreading diameter and spreading time. Also, a brief introduction of the numerical code Thetis we used to conduct simulations is presented, including the governing equations, the contact angle model and a validation against experiments. At the end of this chapter, we explain the motivation of this work.

Chapter 2 details the spreading and retraction dynamics in terms of the spread factor ξ, especially the dynamics in the early spreading stage and the retraction dynamics. The effects of wettability on early spreading dynamics and retraction dynamics, also the effects of Weber number and Ohnesorge number on dynamics. A comparison between a theoretical model pro-

viding prediction of time-evolving spread factor and simulation results is also included. In this chapter, two liquids are adopted into our simulation, the water and molten ceramic, and the contact angle between the droplet and target suface has a wide range from 15° to 170°.

In the following three chapters, we focus on the molten ceramic droplet impact, which takes place on superhydrophobic surfaces with higher contact angle from 150° to 170° to get rebound outcome after droplet impacting on surfaces.

Chapter 3 focuses on the droplets' maximum spreading state on purely non-wetting surfaces. The effects of impact velocity, surface tension and viscosity on maximum spreading diameter are investigated. We also suppress to establish a cross-over of maximum spreading diameter between capillary and viscous regimes by rescaling the maximum contact diameter to eliminate the effects of wettability at low impact velocity. In addition, we conducted detailed analysis on the maximum spreading time and observed a scale function similar to the one for maximum spreading diameter. The last and the most important work in this chapter is the correlation between maximum spreading diameter and spreading time, which is important to estimate the dissipation work in energy analysis.

Chapter 4 conducted a systematic work on the droplets' bouncing-off instant on superhydrophobic surfaces, and illustrates the mechanisms behind the different geometric shapes and air-bubble entrapment at the bouncing-off instant. The influences of inertial forces, capillary forces and viscous forces on the contact time are studied and a corresponding scale is built

Chapter 5 concerns the energetic analysis of droplets' dynamics after impaction, by considering three states: the initial state, the maximum spreading state and the bouncing-off state. Then several theoretical models predicting the maximum spreading diameter are compared and improved with a correlation between maximum spreading diameter and spreading time obtained previously. This energetic analysis helps illustrating the dominating forces during spreading and retraction.

In conclusion, this manuscript presents a work aiming at illustrate the physics behind the droplets' dynamics after impaction on smooth solid surfaces. The scales we find concerning the jetting time and contact time could help potential analysis concerning the heat and mass transfer between the droplet and target substrate. The energetic analysis presented shed light on the distinction between different regimes, the capillary regime and the viscous regime, also the cross-over between them. Meanwhile, the correlation we obtained between maximum spreading

diameter and spreading time is expected to have a significant impact on the theoretical energetic analysis related to maximum spreading.

Chapter 2

Characteristic Spread Factor ξ

According to Rioboo *et al.* [81], the spreading procedure of a droplet could be divided into four phases: the kinematic phase, the spreading phase, a relaxation phase and a wetting/equilibrium phase. In the kinematic phase, The time when the liquid medium breaks through the droplet free surface at the contact edge is called jetting time. The period between the first contact and the jetting time is regarded as the initial spreading stage. During this stage the shape of the droplet resembles a truncated sphere. Chandra and Avedisian [16] and Rioboo *et al.* [81] experimentally show that the jetting is characterised by the formation of a thin liquid lamella, emerging from the droplet surface illustrated with our simulations in Fig.2.1.

2.1 The Jetting Time

The parameter, jetting time, is of significance in understanding the dynamic behaviour of the impacting droplet, which plays an important role in the splash of the droplet after impact. Further, when the solidification of a molten metal or ceramic droplet is taken into account for coating application, it is required to know the occurring sequence of the solidification and jetting for better understanding the solidification of the molten droplet on the target surface. Moreover, the jetting time is also essential to the analytical prediction models based on some droplet shape assumptions. After the jetting, the shape of a droplet becomes more complicated than in the initial stage of spreading.

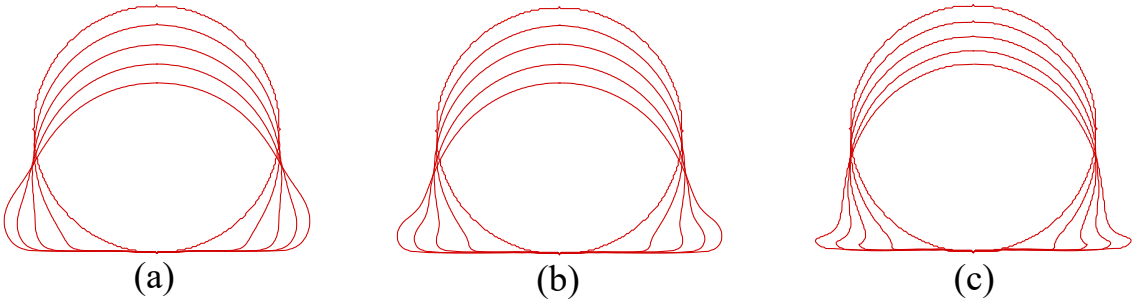

FIGURE **2.1**: Numerical simulations of the liquid droplet on solid surface ($\theta = 165°$) showing the geometric shape before impact and after impact. (a) Ceramic droplet impact at $V_0 = 5m/s$, $We = 8.55$, $Re = 28.5$. The interval between each picture is set as $\Delta t/(D_0/V_0) = 0.083$. (b) Ceramic droplet impact at $V_0 = 10m/s$, $We = 34.2$, $Re = 57$. The interval is $\Delta t/(D_0/V_0) = 0.083$. (c) Ceramic droplet impact at $V_0 = 20m/s$, $We = 342$, $Re = 114$. The interval is $\Delta t/(D_0/V_0) = 0.063$.

In Fig.2.2, the effects of wettability and impact velocity on the jetting time are investigated through a numerical simulation of a water droplet impacting onto surfaces with varied characteristic wettability at different impact velocities. It is concluded that the wettability of the surface has little influence on the jetting time. In addition, the jetting time t_j scales as,

$$\frac{t_j}{(\rho D_0^3/\sigma)} \sim V_0^{-1}. \tag{2.1}$$

In particular, according to our simulations (the data presented in Fig.2.2), the data could be divided into two groups $\theta \leq 120°$ and $135° \leq \theta \leq 170°$, considering the slight difference between them. In each group, the data points presenting different contact angle coincide. Either group could be fitted well as follows,

$$\begin{aligned} \frac{t_j}{(\rho D_0^3/\sigma)} &= 0.00741 \cdot V_0^{-1},\ 15° \leq \theta \leq 120°; \\ \frac{t_j}{(\rho D_0^3/\sigma)} &= 0.0056 \cdot V_0^{-1},\ 135° \leq \theta \leq 170°. \end{aligned} \tag{2.2}$$

The impacting droplet with a larger Weber number jets a lamella at an earlier time point; indeed, the pressure inside the droplet at the contact line gets high enough to overcome the corresponding surface tension to form a lamella.

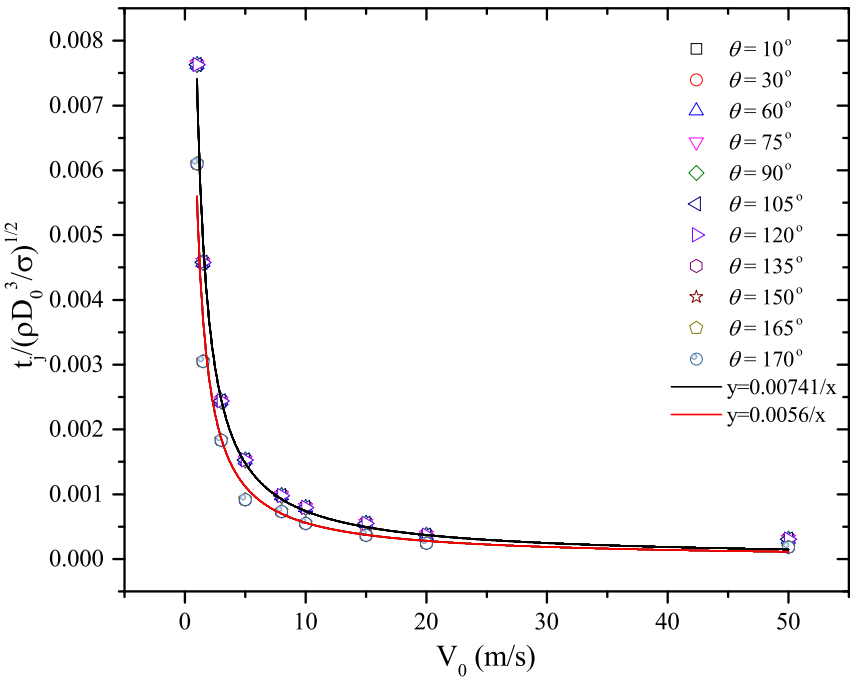

FIGURE **2.2**: The jetting time of a droplet impacting at varied initial velocities onto solid surfaces with different wetting properties. ($We = 36.8 \sim 92095.8$)

2.2 Effects of Wettability on Early Spreading

For the perfectly wetting surfaces, Biance *et al.* [12] observed that the spread factor of water droplet grows as $\xi \sim t^{1/2}$. While in the case where the surfaces are partially wetting, Bird *et al.* [11] found that the dynamics of droplet impact in the initial stage, is such that $\xi \sim t^{\alpha}$, where the exponent α varies with the equilibrium contact angle. Recently, Winkels *et al.* [113] used two methods, molecular dynamics simulations and high-speed imaging, to study initial spreading dynamics. Both methods indicate that the spread factor is independent of wettability, and growing as the square root of time in the initial stage of spreading.

Through our simulations, we obtain the same conclusion for spreading in the initial stage. However, we plan to go through the details of the dynamic behaviour in the initial stage of spreading from two perspectives. The first one is that in spite of the conclusion that the spread factor in the initial stage is independent of Weber number and contact angle, we question whether the influence of contact angle will change in a large range of Weber numbers. In Fig.2.3, different contact angles and various impact velocities are considered. Two different spreading behaviours are observed, for $0.2 < (t^*)^{1/2} < 0.35$, the spread factor is proportional to the square root of di-

mensionless time $(t^*)^{1/2}$ but this scaling law do not work for $(t^*)^{1/2} \leq 0.2$. It is also remarked that the effects of wettability on spreading are more important than the effects of impact velocity in the early spreading stage and may not be negligible. Fig.2.4 shows that in the very early spreading stage, droplet impacting onto hydrophobic surfaces with high contact angles, produces larger spread factor than onto the hydrophilic surfaces with low contact angles. This phenomenon can be explained as follows, in the early stage of spreading, the strong liquid-solid interaction existing for the hydrophilic surfaces restricts the spreading of the droplet more severely than the relatively weak liquid-solid interaction holding for the hydrophobic surfaces.

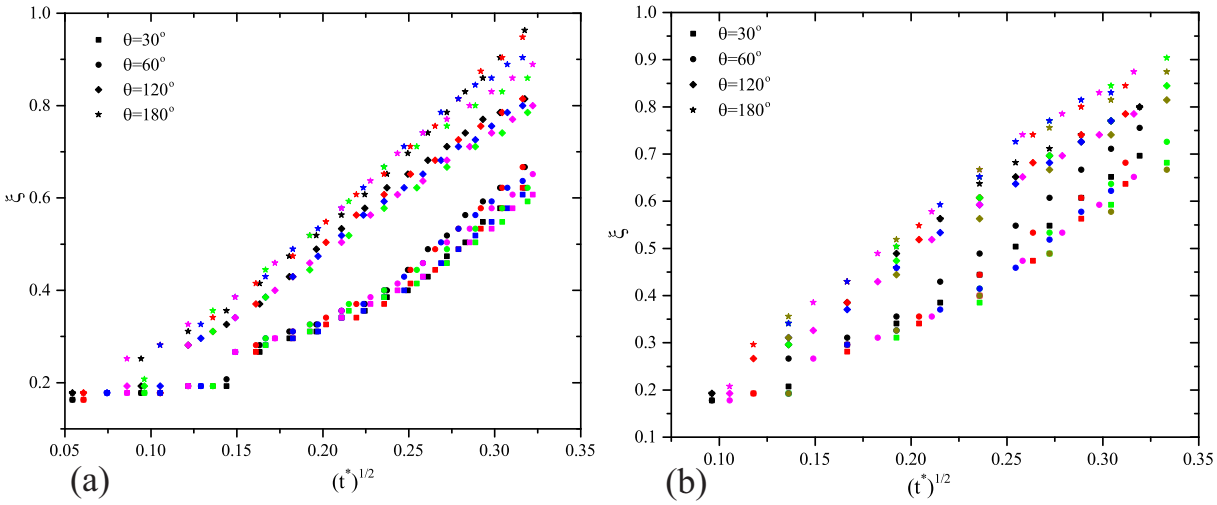

FIGURE **2.3**: The effects of wettability on the spread factor of water droplet impact at varied impact velocities. (a) In the high Weber number regime ($We > 2000$): the black symbols for the $V_0 = 8m/s$ ($We = 2357.6, Re = 21513.6$), red for $V_0 = 10m/s$ ($We = 3683.8, Re = 26892$), blue for $V_0 = 15m/s$ ($We = 8288.6, Re = 40338$), magenta for $V_0 = 20m/s$ ($We = 14735.3, Re = 53784$), green for $V_0 = 50m/s$ ($We = 92095.8, Re = 134460$). (b) In the low Weber number regime ($We < 200$): the black symbols for the $V_0 = 1m/s$ ($We = 36.8, Re = 2689.2$), red for $V_0 = 1.5m/s$ ($We = 82.8, Re = 4033.8$), green for $V_0 = 2m/s$ ($We = 147.3, Re = 5378.4$), blue for $V_0 = 2.5m/s$ ($We = 230.24, Re = 6723$), magenta for $V_0 = 3m/s$ ($We = 331.5, Re = 8067.6$) and dark yellow for $V_0 = 5m/s$ ($We = 920.96, Re = 13446$).

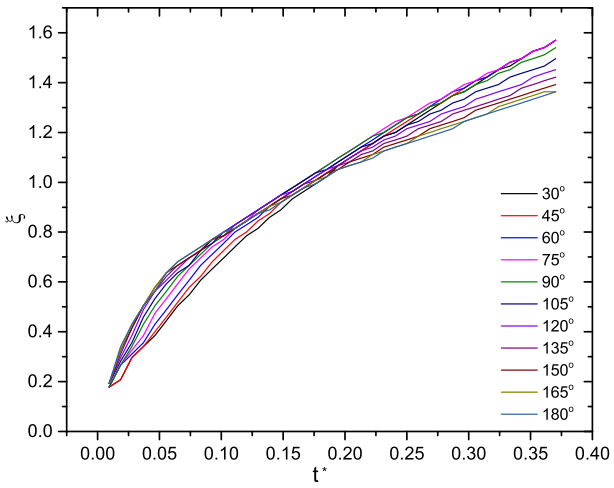

FIGURE **2.4**: The transition zone of the effects of wettability on the spread factor of a water droplet impacting at $V_0 = 1m/s$ $(We = 36.8, Re = 2689.2)$ onto different surfaces.

Moreover, in Fig.2.4, the zone $0.15 < t^* < 0.2$ is a transition one where the curves drawn with different wettability intersect with each other, and the gradient of the curves with smaller contact angle is more important than that of the curves with larger contact angles. This means that the spread factor of a droplet on a surface with a smaller contact angle increases faster than the one of the same droplet but impact on a surface with a bigger contact angle. These effects of wettability on spreading can be explained in the following way: in the early spreading stage before the transitional point, the inertial effects can be omitted so that only adhesive and cohesive forces affect the spreading; after the transitional point, the inertial force starts to influence the spreading of the droplet. The effects of contact angle on early spreading behaviour may be small when contact angle θ varies in the range of $10° \sim 90°$ or in the one of $90° \sim 170°$. However, the difference between the early spreading behaviours on hydrophilic surfaces and hydrophobic surfaces appears to be not negligible.

When considering the heat transfer between the droplet and the substrate, this investigation on early-spreading could put some insight on the heat transfer at early stage in particular concerning appearance or not of solidification. As the cooling rate is a decreasing function of splat thickness, the difference of cooling rate in the jetting lamella and in the centre truncated-sphere could lead to different contact strength between the splat and the substrate.

2.3 The recoil stage

The recoil stage starts at the moment when a droplet reaches its maximum spreading extent after impacting onto target surface. The maximum spread factor ξ_{max} is of critical importance for studying the spreading and recoiling dynamics of a droplet. Upon impact, its liquid initially spreads on a wettable or non-wettable surface until its kinetic energy is almost converted into surface energy and viscous dissipation. In other words, at the maximum spreading state, the kinetic energy inside the liquid decreases due to dissipation but is not zero. It is balanced by the surface energy. The maximum spread in the capillary regime is found to scale with the Weber number, while the maximum spread in viscous regime can be described by a function of the Reynolds number [see, e.g., 59, 16, 9, 26].

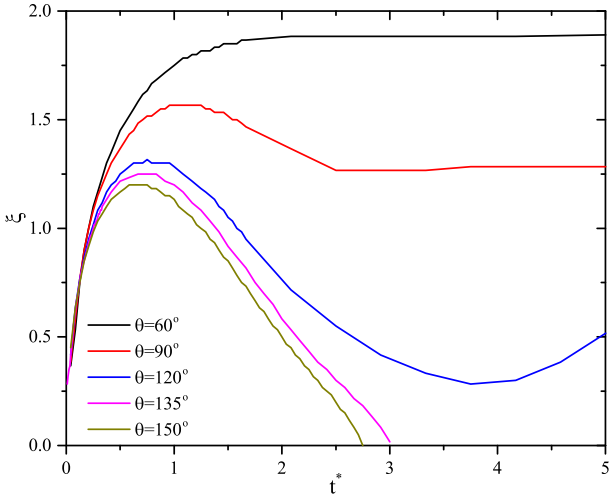

FIGURE **2.5**: Time-evolving spread factor of a droplet upon impacting on the target surface with different wettability characterised by contact angles with $We = 8.55$ and $Re = 28.5$.

Here, we switch the droplet fluid from water to molten ceramic (a common material used in coating) in order to study recoiling dynamics.

Fig.2.5 presents the molten ceramic droplet impacting on target surfaces with different wettability characterised by $\theta = 60°, 90°, 120°, 135°$ and $150°$ for $We = 8.55$ and $Re = 28.5$. On a hydrophilic surfaces with $\theta = 60°$, there only exists spreading behaviour. Starting from $\theta = 90°$, the recoiling behaviour appears; with $\theta = 90°$, the droplet recoils to an equilibrium state after reaching the maximum spreading diameter; at $\theta = 120°$, the droplet first oscillates and then reaches an equilibrium; for $\theta = 135°$ or $150°$, the droplet first recoils and then bounces

off the target solid surface.

In Fig.2.6, we show the velocity and pressure fields in the droplet and the nearby atmosphere at different dimensionless time points in the case of $We = 8.55$ and $Re = 28.5$. At $t^* = 0.5$, the droplet has the velocity components along the impact and spread directions. At $t^* = 0.75$, the spreading droplet reaches the maximum spread extent. After this state, the velocity components opposite to the spreading and impacting direction due to the surface tension appear at the rim of the droplet, which leads the droplet to recoil and eventually bounce off the solid surface.

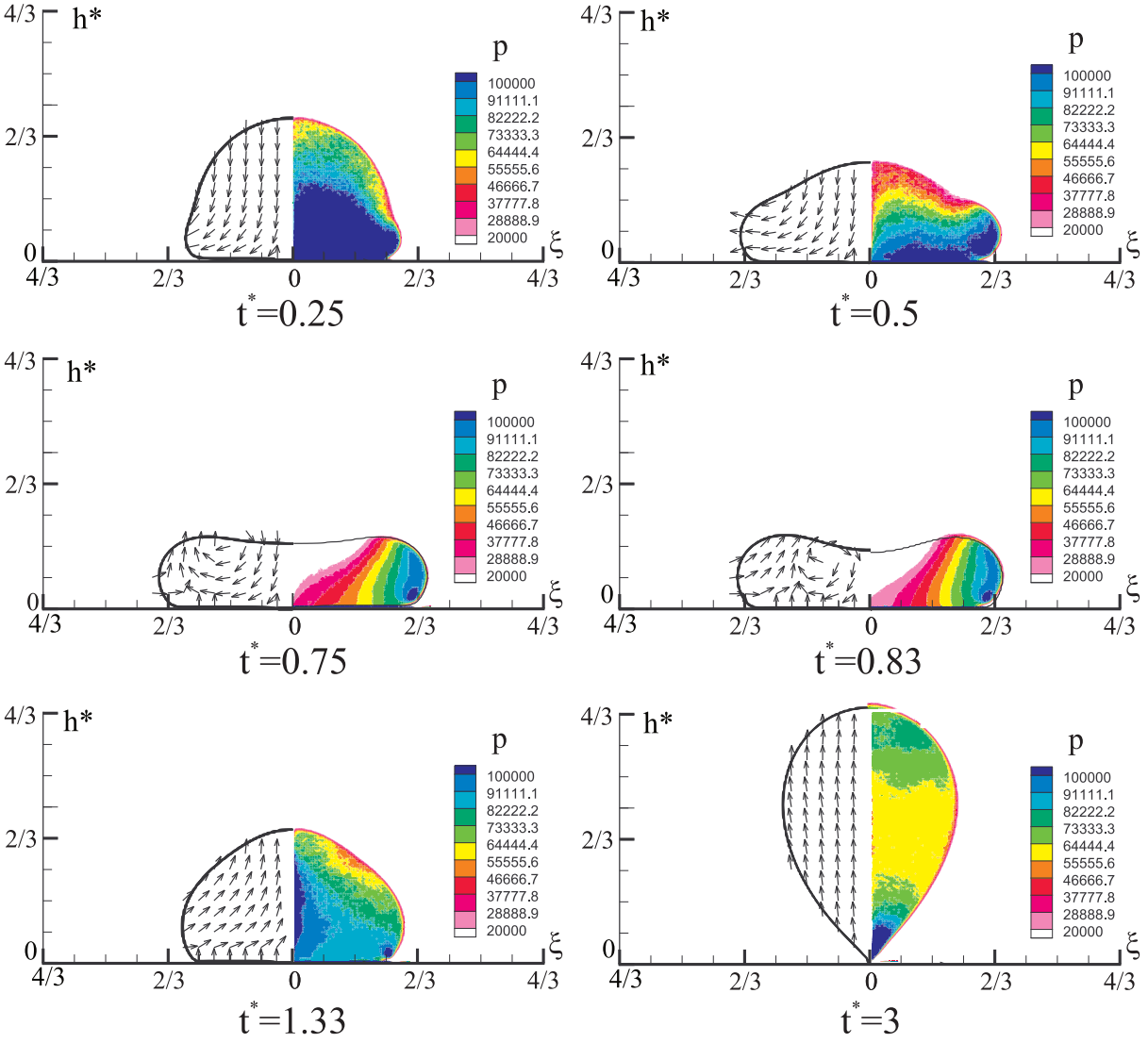

FIGURE **2.6**: Microdroplet impact and spreading simulation at $We = 8.55$ and $Re = 28.5$ on a hydrophobic substrate($\theta = 135°$). Left: velocity field. Right: pressure field.

2.3.1 Effects of the Weber and Ohnesorge numbers on recoil

Schiaffino and Sonin [90] observed that the inertial effect dominates the early stage of spreading and the later dynamic behaviours of droplet depend mainly on Oh and θ. This subsection discusses the role of We and Oh and the next subsection will address the effect of the contact angle.

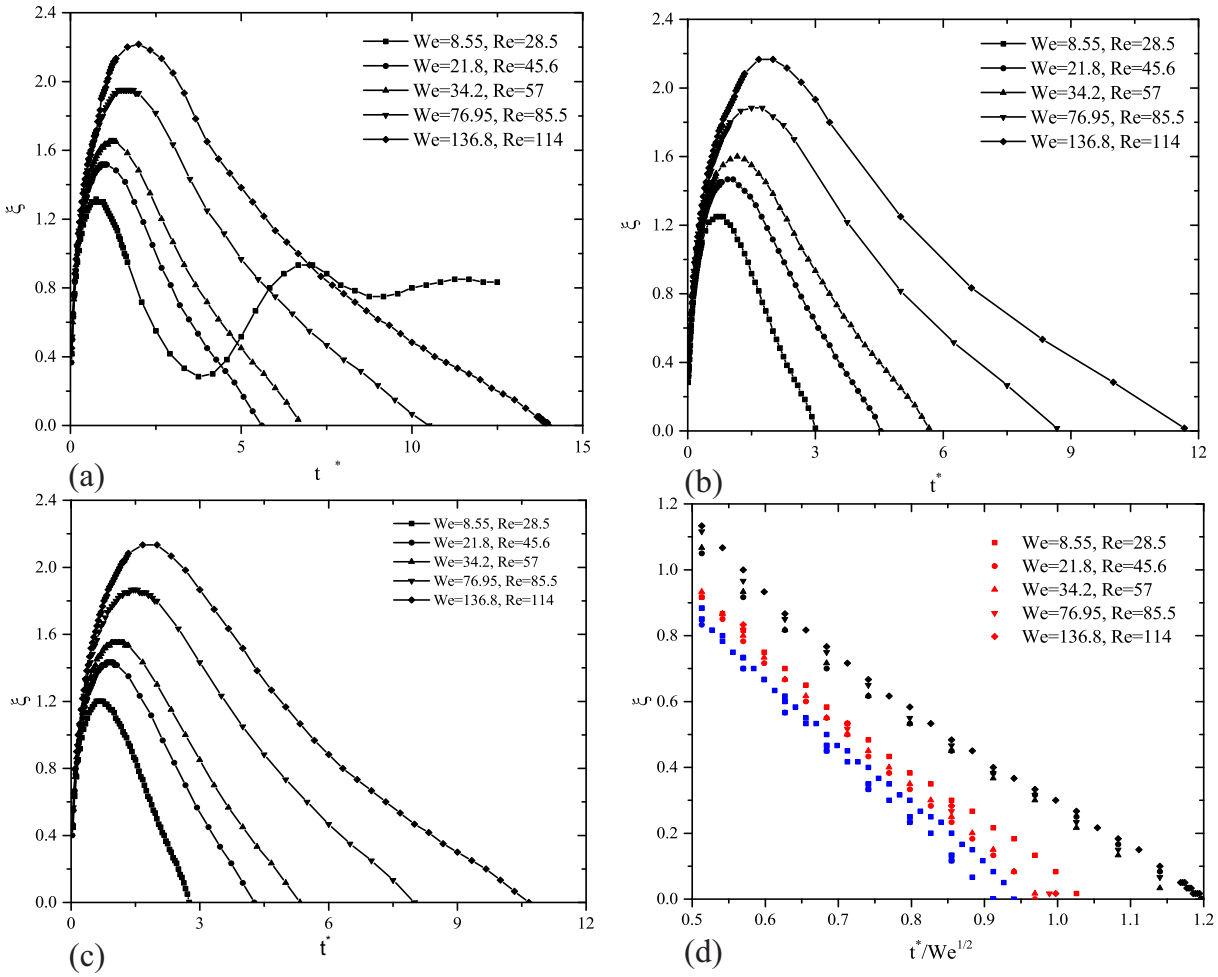

FIGURE **2.7**: Time-evolving spread factor of a droplet upon impacting on the hydrophobic surfaces with $Oh \approx 0.1$. (a) droplet impacting on surface with $\theta = 120°$; (b) droplet impacting on surface with $\theta = 135°$; (c) droplet impacting on surface with $\theta = 150°$; (d) Time-evolving spread factor during recoil stage ($t^*/We^{1/2} > 0.5$) of different non-dimensional numbers, black color for droplet impacting on the surface with $\theta = 120°$, red for $\theta = 135°$, blue for $\theta = 150°$.

To focus on the recoil behaviour of a droplet after impacting onto the target surface, in Fig.2.7,

we present the time-evolving spread factor of a droplet impacting, with different Weber and Reynolds numbers, but a constant Ohnesorge number $Oh = 0.1$, onto surfaces with $\theta = 120°$ (subfigure a), $\theta = 135°$ (subfigure b) and $\theta = 150°$ (subfigure c). In subfigure (d) of Fig.2.7, a new dimensionless time $\hat{t}$ is introduced:

$$\hat{t} = \frac{t^*}{\sqrt{We}}. \tag{2.3}$$

The starting value of $\hat{t}$ is set at 0.5, due to the spread factor ξ of the simulations that is around 1 ($0.8 \sim 1.2$). For a constant Weber number and a contact angle, we conclude that, for the spread factor ξ in recoiling stage,

$$\xi \sim t^*/We^{1/2}. \tag{2.4}$$

The effect of Ohnesorge number on the recoil stage of a droplet impacting onto a surface with the equilibrium contact angle $\theta = 135°$ or $\theta = 150°$ is investigated by keeping the Weber number constant ($We = 34.2$). In the subfigures (a) and (c) in Fig.2.8, where the time-evolving spread factor curves with different Ohnesorge numbers are shown, it is interesting to note that:

- the spread factors ξ of these curves attain its maximum value when $t^* = 1.16667$;
- the curves in subfigures (a) and (c) intersects when $\xi \approx 1$, and at this point $\hat{t} \approx 0.5$ (shown in (b) and (d) in Fig.2.8).

The Ohnersorge number scales the resisting force in the recoiling process. A high Ohnesorge number number, indicating that the liquid has a relatively high dynamic viscosity and a low surface tension, indicates that the viscous dissipation is dominant compared to the energy converted into surface energy. As the surface energy is the motor behind the recoiling behaviours of a droplet, the lower surface energy leads to slower retraction.

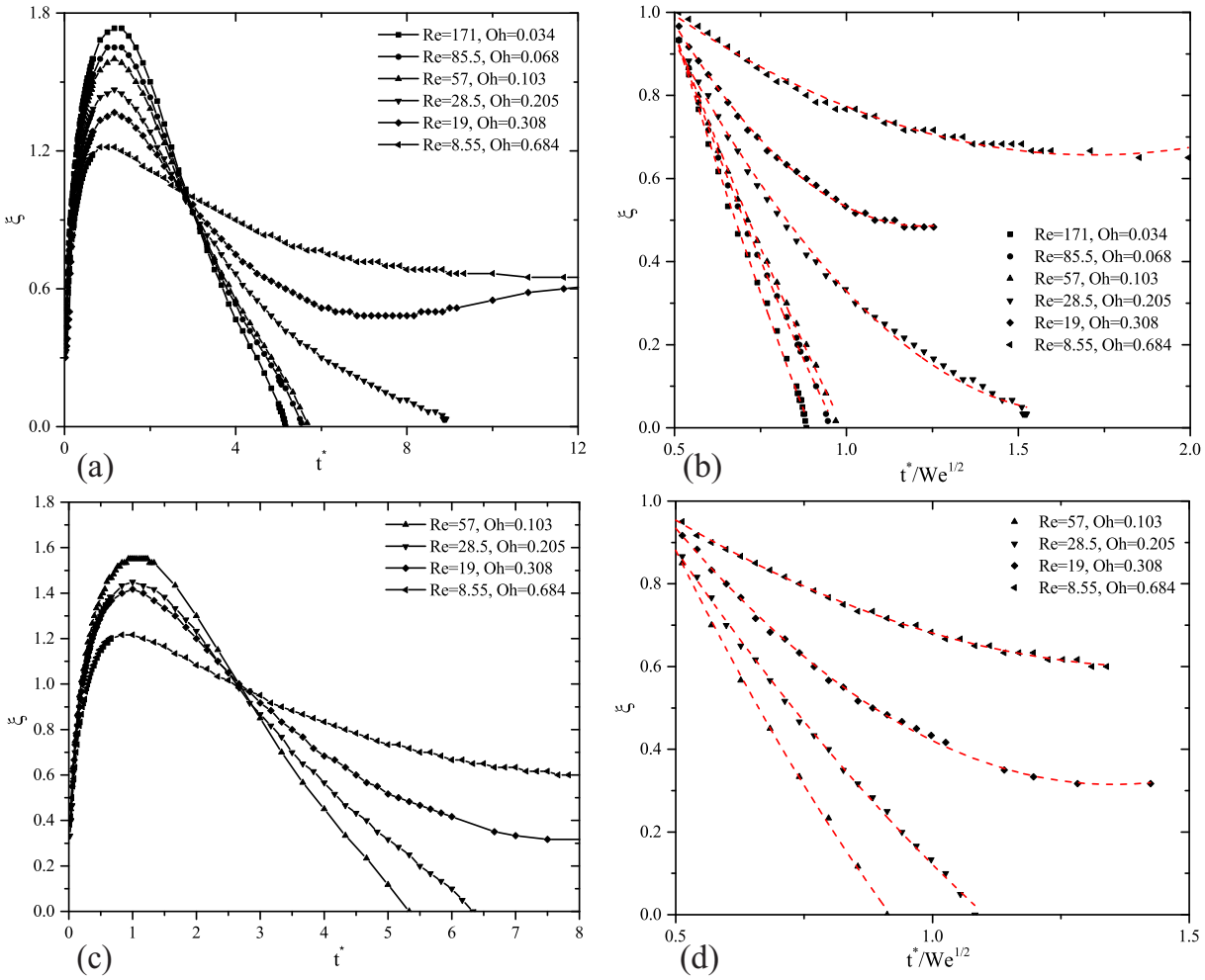

FIGURE **2.8**: Effect of the Ohnesorge number on the droplet impact dynamics with the dimensionless number $We = 34.2$ on the solid surface. (a) with $\theta = 135°$, (c) with $\theta = 150°$. (b) and (d) present the partial curves after $\hat{t} = 0.5$ of (a) and (c), respectively. The red dash line is the second-order polynomial fitting curve of the symbols.

Taking the point defined by $\xi = 1$ and $\hat{t} = 0.5$ as a special point to split the curves, the curves in (a) are plotted versus $\hat{t}$ starting from $\hat{t} = 0.5$ and stopping when the curves arrive at the first bottom in subfigure (b) in Fig.2.8. One apparent pattern is that the slope of these curves increases with the augmentation of the Ohnesorge number. These curves simulated with $Re \geq 57$ can be fitted by linear equations, while those with $Re < 57$ cannot be fitted in this way. In fact, the recoil behaviour of the droplet after $\hat{t} = 0.5$ turns out to be characterised by

$$\xi = a_1\hat{t}^2 + a_2\hat{t} + a_3, \tag{2.5}$$

where the coefficients a_1, a_2 and a_3 are constants to be determined experimentally or numerically. The corresponding values of a_1, a_2 and a_3 of the simulation ((b) of Fig.2.8) with $We = 34.2$ and $\theta = 135°$ are listed in Table.2.1

TABLEAU **2.1**: The list of values of a_1, a_2 and a_3 obtained from simulations ($We = 34.2, \theta = 135°$)

Re	a_1	a_2	a_3
8.55	0.22706	-0.77932	1.32561
19	0.92842	-2.27312	1.87674
28.5	0.64743	-2.1675	1.8493
57	0.55588	-2.75883	2.19094
85.5	0.75403	-3.12523	2.32566
171	0.68767	-3.37056	2.46677

2.3.2 Effects of the contact angle on recoil

This subsection examines the effects of target solids on the recoiling of molten ceramic droplets. The equilibrium contact angle θ is assumed to be the major parameter for describing the effects of wetting that determines the strength of recoiling. The Fig.2.5 compares the contact diameters of the droplet on different target surfaces with varying contact angles. With similar initial conditions, the contact diameters in the early spreading stages evolve likely as the inertial force governs this stage. In the recoiling stage after the maximum spreading state, major part of the initial energy has been dissipated against spreading, only a minor part is converted into surface energy due to deformation. The wetting effects could not be ignored.

As shown in Fig.2.7 (d), in the cases where the droplets are about to bounce off the target surface, the contact angle θ ($\theta = 120°, 135°, 150°$) has little influence on the slopes of the curves $\xi \sim \hat{t}$. This phenomenon can be explained by the fact that in the case where the droplet bounces off the surface, the contact angle has much less effect compared to the kinetic energy of the recoiling droplet. But the contact angle does affect the value of the spread factor. Indeed, different contact angles lead to different maximum spread factors.The maximum spreading is the initial condition for the recoiling. In this section, we have presented the numerical results obtained by varying the target surfaces and impact inertia. The simulations performed have

shown that the motion of the droplet (characterised by the contact radius) is governed by the Weber number, the Ohnesorge number, and the contact angle. This is consistent with the result of the analysis for the liquid deposition process by Schiaffino and Sonin [89]. The quantitative predictions of the recoiling velocity and the thickness of the lamella are important parameters in the applications such as spray-cooling and coating process, as they have great influences on the cooling and solidification rates of the splat.

2.4 Numerical results compared to the relevant analytical ones

Kim and Chun [48] developed a model based on the variational principle, assuming the droplet shape to be cylindrical, and modified the truncated-sphere model to accommodate the dissipation factor. They showed that the cylinder model estimates the retraction appropriately for low Oh ($Oh < 0.002$), and cylinder model for relatively high Oh ($Oh < 0.002$). In these two models, an empirically determined factor, the dissipation factor F_d, is introduced [see, e.g., 48]. These two models of droplet shape have their limitation for predicting spread and recoiling processes and use an empirical dissipation factor, F_d. The value of F_d for water is equal to 15 in the work of Kim and Chun [48]. The cylinder model predicts the spread radius as

$$\ddot{R} - \hat{A}(R)\dot{R}^2 + \hat{B}(R)\dot{R} + \hat{C}(R) = 0, \tag{2.6}$$

where the coefficients are given as

$$\hat{A}(R) = 3R^{-1} - R^{-3}\Gamma(R)/3, \tag{2.7}$$

$$\hat{B}(R) = 2F_d\Gamma(R)Oh^{1/2}/3, \tag{2.8}$$

$$\hat{C}(R) = -96R^3\Gamma(R)\left(R^{-7}/216 - (1 - cos\theta)R^{-4}/36\right), \tag{2.9}$$

where

$$\Gamma(R) = 9R^2\left(R^{-6}/216 + 1/16\right)^{-1}/16. \tag{2.10}$$

The truncated-sphere model predicts the temporal evolution of h as

$$2E(h)\ddot{h} - G(h)\dot{h}^2 + I(h)\dot{h} + Jh = 0, \tag{2.11}$$

where the coefficients are given by

$$E(h) = \left(\frac{M'(h)}{M(h)}\right)^2 \left(\frac{13h^5}{180} + \frac{11h^2}{144} + \frac{1}{72h}\right), \tag{2.12}$$

$$M(h) = \frac{2h + h^4}{6}, \tag{2.13}$$

$$\begin{aligned} G(h) = &\left(\frac{13h^4}{36} + \frac{11h}{72} + \frac{1}{72h^2}\right)\left(\frac{1}{3} + \frac{2h^3}{3}\right)\left(\frac{h}{3} + \frac{h^4}{6}\right)^{-2} \\ &+ \left(\frac{13h^5}{90} + \frac{11h^2}{70} + \frac{1}{36h}\right)\left(\frac{1}{3} + \frac{2h^2}{3}\right) \\ &\times \left(2h^2\left(\frac{h}{3} + \frac{h^4}{6}\right) - \left(\frac{1}{3} + \frac{2h^3}{3}\right)^2\right) \cdot \left(\frac{h}{3} + \frac{h^4}{6}\right)^{-3}, \end{aligned} \tag{2.14}$$

$$I(h) = \psi\left(h^4 - 2h + h^{-2}\right)\left(\frac{1}{3} + \frac{2h^3}{3}\right)^2 \left(\frac{h}{3} + \frac{h^4}{6}\right)^{-2}, \tag{2.15}$$

$$J(h) = 2\left(4h - h^{-2} + cos\theta(2h + h^{-2})\right), \tag{2.16}$$

where the parameter is given as

$$\psi = F_d \cdot Oh^{1/2}, \tag{2.17}$$

A comparison of the results of our simulations with the analytical results issued from the cylinder and truncated-sphere models is performed.

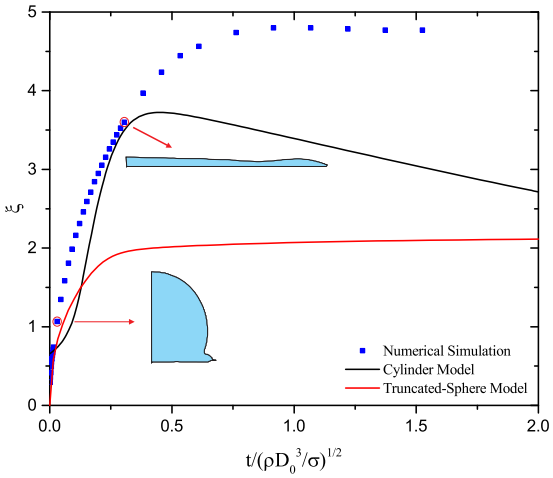

FIGURE **2.9**: Water droplet impact onto smooth solid surfaces: $We = 37$, $Re = 2022$, $\theta = 30°$.

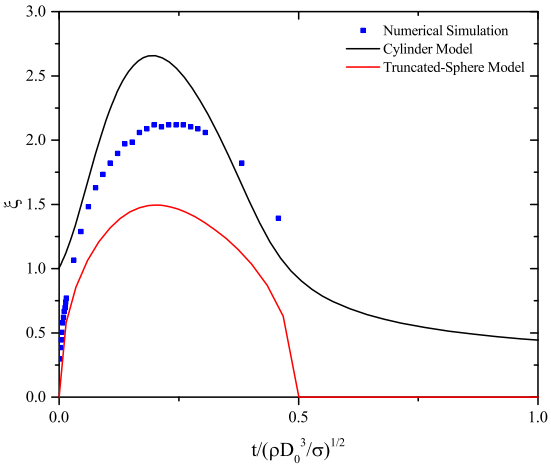

FIGURE **2.10**: Water droplet impact onto smooth solid surfaces: $We = 37$, $Re = 2022$, $\theta = 120°$.

Through this comparison in Fig.2.9 and Fig.2.10, we conclude that, besides the Ohnesorge number influence on the accuracy of the prediction of these two models, the assumption of droplet

shape is critically important for the accuracy of theoretical prediction. It is not sufficient to use only one of these two models to estimate the spread factor of droplet impact as the geometry of the droplet changes significantly. The truncated-sphere model is accurate for predicting the spread factor in the initial stage of the spreading, i.e., before the jetting lamella appears. Between the jetting time and the time at the maximum spreading extent, a model combining the cylinder and truncated-sphere ones should work. But because of the complexity of this combination, it is hard to establish a relation between the thickness of the lamella, the height of the truncated-sphere and the base diameter of the droplet. Prediction of the maximum spreading diameter of a droplet impacting on a solid surface provides a quantitative estimation of heat removal and energy consumption.

2.5 Summary

The normal impact of liquid droplets on solid surfaces has been systematically studied in a numerical way, by considering the influences of Weber number, Reynolds number, Ohnesorge number and contact angle. In particular, the dynamic behaviours in the early spreading stage and the dynamic retraction in the recoil stage have been thoroughly investigated. Besides the fact that many studies concerning specific issues in thermal spray have been conducted, the present study with ideal assumptions provides some new physical insights.

At the early spreading stage, the spread factor ξ turns out to be proportional to the square root $(t^*)^{1/2}$ of the dimensionless time t^* for $0.2 < (t^*)^{1/2} < 0.35$ but this proportionality does not hold for the very initial stage where $(t^*)^{1/2} < 0.2$. During the early spreading of a droplet, the effects of the contact angle are more important than those of Weber number. A transitional zone has been identified to explain the competition of the inertial force and the liquid/solid interaction in the early stage. An important parameter is the jetting time, which allows determining when the kinematic phase of the droplet spreading ends. The dimensionless jetting time t_j^* is inversely proportional to the square root of the Weber number and not affected by the wettability of the target solid surface. After the jetting time, the analytical truncated-sphere model is no longer suitable for describing the dynamic behaviour.

At the recoil stage, it is shown that the Ohnesorge number scaling the resisting force against the surface tension is the parameter determining the retraction velocity of the droplet, while the We-

ber number and the contact angle change the retraction velocity barely. We have also obtained the important conclusion that, with the aid of another dimensionless time $\hat{t}$, the recoil behaviour of droplet impact after $\hat{t} = 0.5$ is well described by a second-order polynomial equation of $\hat{t}$.

The present work can be extended in several directions. First, the static contact angle adopted in the present work can be replaced by a dynamic contact angle in agreement with real experimental conditions [see, e.g., 92, 93]. Second, the heat transfer between droplets and surfaces should be taken into account. The temperature of the target substrate affects the outcomes of droplet impact enormously [see, e.g., 27]. Third, the phase change of droplets is also important issue to be investigated. Although many studies on millimetre-size droplets have concluded that the solidification is much slower than the spreading, this conclusion remains debatable for small size droplets [see, e.g., 25, 109]. In the present work, only the normal impact of liquid droplets has been studied. A natural extension is to the oblique impact of liquid droplets. Such an extension is not direct but expected to be particularly rich and important from the mechanical point of view.

Chapter 3

Maximum Spreading State of Droplets Impacting On Hydrophobic Surfaces

The studies concern the deposition of droplets on solid substrate, which is essential to many applications such as ink-jet printing, rapid prototyping, coating manufacturing [see, e.g., 4, 10, 66]. For the applications involving droplet deposition, the contact area between the droplet and the substrate, especially the maximum contact area plays an important role. Under the assumption that the whole process of droplet impact is axisymmetric, the maximum contact area is predicted or controlled through the analysis of the maximum spreading factor ξ_{c_max}. The maximum spreading factor is not only directly related with the performance of spray systems in industrial processes, but also an important preliminary condition for the following retraction process. Controlling or predicting maximum spreading factor is essential for many topics involving the deposition of an impacting droplet or the contact time of a rebounding droplet. Parameters, such as droplet radius, impact velocity, surface tension, dynamic viscosity and wettability, all play a role in spreading to maximum extent. Analytical, semi-analytical, numerical methods have been used by extensive models to analyse the maximum spreading diameter [see, e.g., 72, 15, 52, 56]. A strictly theoretical model, based on the mass and momentum equations, is introduce by Roisman *et al.* [82] to predict the evolution of the droplet diameter in both the spreading and receding phase.

The maximum spreading time t_{max}, the instant at which the droplet spreading diameter reaches its maximum value is as well important. More precisely, maximum spreading time is the time when the velocity of the rim becomes towards the centre of the splat, as the droplet maintains

its maximum spreading time for several calculation steps. Note that at the instant t_{max}, the velocity of the rim could be ignored, whereas the liquid in the lamella continues to move. The analytical or semi-analytical approaches predicting the maximum spreading diameter require the maximum spreading time to estimate the viscous dissipation work in spreading.

On hydrophobic surfaces, an impacting droplet will firstly spread out to the maximum state, then recoil and eventually bounce off the surface. Some semi-analytical models were proposed to characterise the recoiling motion [see, e.g., 32, 48]. Kim and Chun [48] used an empirically determined dissipation factor to estimate the viscous friction while assuming the droplet at maximum spreading depicts like a truncated-sphere or a cylinder, their study shows that the Ohnesorge number plays the most important role in characterising the recoiling motion. Gao and Li [32] assume that the droplet maintains a ring-like shape and the volume of the thin central film is zero. Then an experimentally-fitted viscous dissipation terms along with a flow potential energy term (due to nonuniform distribution of pressure) are introduced into the equation of the conservation of energy predict the dynamic behaviours of the droplet.

In this chapter, the axisymmetric and isothermal assumptions are adopted. The nonaxisymmetric effects (destabilisation or break-up at the rim) can not be captured with our simulations. However, with this idealisation, the basic spreading and recoiling behaviours could be simulated, which could be difficult to access experimentally. The spreading and subsequent recoiling dynamics of molten ceramic droplets impacting on hydrophobic surfaces ($\theta = 170°$) is studied. Through performing extensive simulations, we investigate the role of parameters, such as impact velocity, surface tension and viscosity, on the maximum spreading factor, maximum spreading time, contact time and retraction time. The sample fluid is chosen as the molten ceramic. Then, vary the surface tension ($0.2 \sim 0.8N \cdot m^{-1}$) and dynamic viscosity($0.01 \sim 0.1Pa \cdot s$) of the droplet to achieve a comprehensive and complete set of data from low to high impact velocity ($3 \sim 25m/s$) in order to analyse their influences on maximum spreading time, contact time and retraction time. More specifically, the aim of this study is to provide more accurate predictions and scalings of these dependent parameters, as observed in our numerical simulations.

The material of the droplet simulated in this paper is the molten ceramic with original density $\rho = 5700kg/m^3$, surface tension $\sigma = 0.5N/m$, dynamic viscosity $\mu = 0.03Pa \cdot s$ and initial diameter $D_0 = 30\mu m$. The strategy adopted in this section to study the influences of impact velocity V_0, surface tension σ and dynamic viscosity μ on the dynamics of the droplet is,

- *Step 1*: varying the impact velocity V_0 and dynamic viscosity μ to study their influences on the dynamics;
- *Step 2*: varying the impact velocity V_0 and surface tension σ to study their influences on the dynamics;
- *Step 3*: based on the above simulations, proposing a scaling for the dynamics of the droplet after impaction and present the scaling in dimensionless numbers We, Re.

To maintain a full rebound of the droplet without splash, the variations of impact velocity V_0, surface tension σ and dynamic viscosity μ are performed as from $3m/s \leq V_0 \leq 25m/s$, $0.2N/m \leq \sigma \leq 0.8N/m$ and $0.01Pa \cdot s \leq \mu \leq 0.1Pa \cdot s$. The corresponding dimensionless numbers are in the range as $1.539 \leq We \leq 267.1875$ and $2.565 \leq Re \leq 213.75$. In this chapter, the maximum spreading factor, the maximum spreading time and the contact time are chosen as representative parameters describing the spreading and recoiling dynamics of the droplet after impact.

3.1 Maximum Spreading Factor ξ_{max} and Maximum Contact Factor ξ_{c_max}

As the maximum spreading diameter is often considered in the research related to the applications where the droplets dynamically wet the target surface and finally deposit on surface. The contact angle between the droplet and surface is usually acute. The spreading diameter observed is the real contact diameter when there is no thin air film between the droplet and surface. The large number of investigations dealing with the maximum spreading account the distance from rim to rim as the maximum spreading diameter D_{max}. When the surface is non-wetting, the difference between the maximum rim diameter and the maximum contact diameter should be taken into consideration. In Fig.3.1, the definition of the maximum spreading diameters D_{max} and maximum contact diameter D_{c_max} are presented. And they are normalised by the initial diameter as

$$\xi_{max} = \frac{D_{max}}{D_0}, \quad \xi_{c\_max} = \frac{D_{c\_max}}{D_0}. \tag{3.1}$$

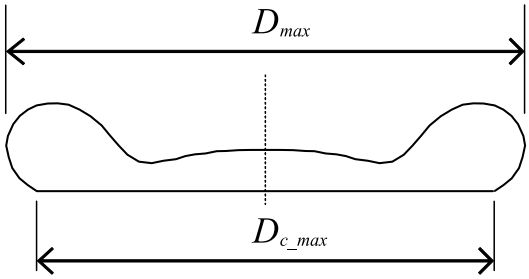

FIGURE **3.1**: Definition sketch of the maximum spreading diameter D_{max} and maximum contact diameter D_{c_max}.

From theoretical perspective, maximum spreading is commonly predicted based on the energy balance, in terms of kinetic energy, surface energy and the viscous dissipation at its maximum spreading. For large Re and We numbers, two regimes may be assumed: one where viscosity may be neglected so that the balance between kinetic energy and surface energy determines ξ_{max}, the other for which viscous dissipation dominates surface tension, ξ_{max} scales as a balance between inertia and viscosity. In the inertial regimes, when the initial kinetic energy is completely converted into surface energy, the maximum spreading factor $\xi_{max} \sim We^{1/2}$ for large Weber numbers [9], when accounting the viscous dissipation in inertial regime, the maximum spreading factor follows that $\xi_{max} \sim We^{1/4}$ [17]. In the viscous regime, ξ_{max} is given by a balance between inertia and viscous dissipation in the spreading droplet, which leads to $\xi_{max} \sim Re^{1/5}$ [17]. Consequently, a single dimensionless number is defined that discriminates between these two regimes: $P = WeRe^{-2/5}$ referred to as the impact parameter. In this chapter, we study a large number of impact events under a variety of initial conditions. None of these cases shows neither simple capillary nor viscous scaling, *i.e.*, all three forces (inertial, capillary, viscous) are important in these cases. Laan *et al.* [52] introduced a broad cross-over regime between the low and high impact velocities by interpolating between $We^{1/2}$ and $Re^{1/5}$. For the cases between these two extreme regimes, the maximum spreading factor should scale as,

$$\xi_{max} = Re^{1/5}\frac{P^{1/2}}{1.24 + P^{1/2}}, \qquad 10 < We < 1700, 70 < Re < 17000, \tag{3.2}$$

where the constant in denominator is a fitting constant. And this scale would be compared in later section with the scaling proposed based on our simulation results in Fig.3.7.

3.1.1 The effects of impact velocity, surface tension and dynamic viscosity on ξ_{max}

The influences of impact velocity V_0, surface tension σ and dynamic viscosity μ on maximum spreading have been extensively investigated experimentally and theoretically [see, e.g., 9, 72, 15, 17, 52, 56]. Here, a brief introduction to these influences is presented. In Fig.3.2, the maximum spreading factor ξ_{max} increases with the increase of the impact velocity as larger initial kinetic energy of the droplet drives the droplet to cover larger area. The Fig.3.3 shows that both the augmentation of dynamic viscosity and surface tension would lead to a smaller maximum spreading factor, as the viscous dissipation and surface tension counter the initial kinetic energy in the spreading stage. The subfigure (a) in Fig.3.3 presents that the influences of dynamic viscosity become larger as the impact velocity increases. The volume that the dissipation takes place becomes larger as the maximum spreading diameter increases, which causes the growth of the influence of dynamic viscosity on maximum spreading factor. The variation of the surface tension σ on ξ_{max} appears to have the similar impact on ξ_{max} regardless of the variation within the impact velocity (see (b) in Fig.3.3).

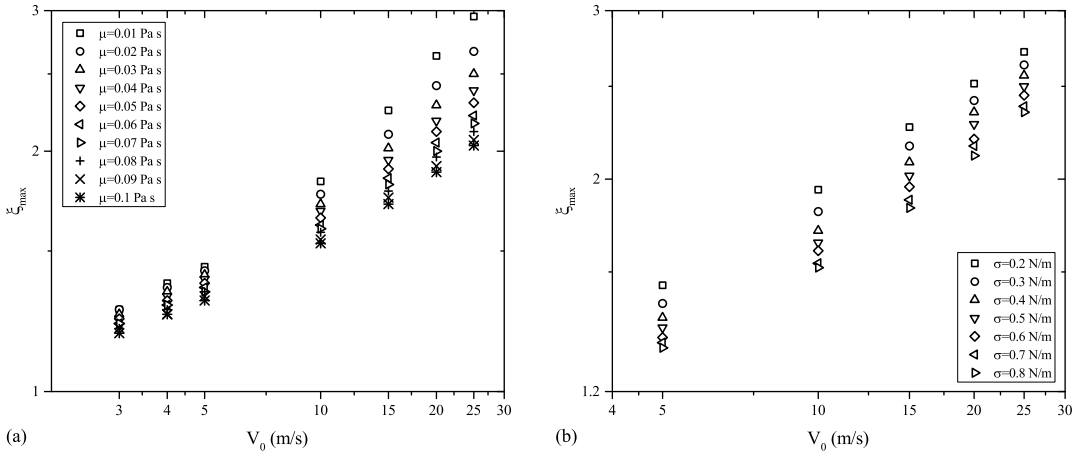

FIGURE **3.2**: The maximum spreading factor ξ_{max} plotted versus impact velocity V_0. (a) with varied dynamic viscosity μ, (b) with varied surface tension σ.

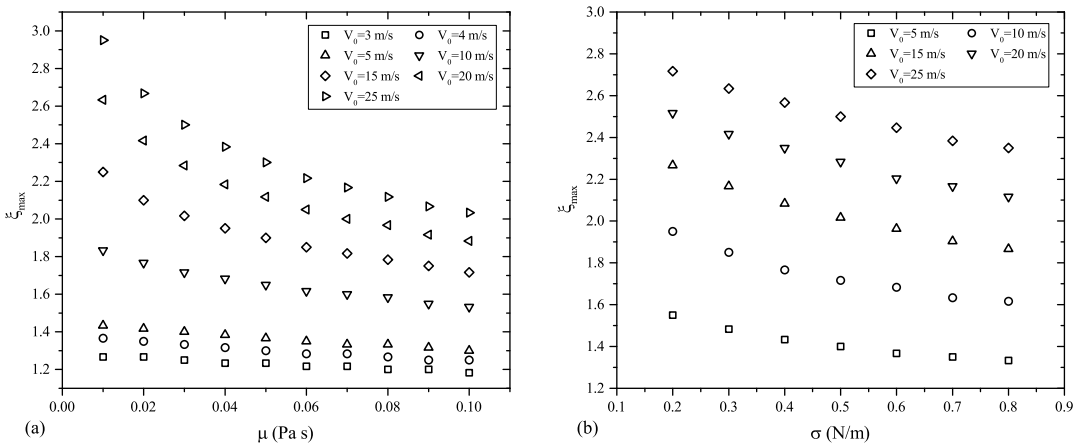

FIGURE **3.3**: (a) The maximum spreading factor ξ_{max} plotted versus dynamic viscosity μ. (b) The maximum spreading factor ξ_{max} plotted versus surface tension σ.

Next, according to the crossover between inertial and viscous regimes proposed by Laan *et al.* [52], the raio $\xi_{max}/Re^{1/5}$ calculated from the data presented in Fig.3.2 is plotted against the function $WeRe^{-2/5}$ in Fig.3.4, it shows that the function failed to provide a smooth crossover between these two regimes. In the higher range $WeRe^{-2/5} > 10$, $\xi_{max}/Re^{1/5}$ scales with $(WeRe^{-2/5})^{1/10}$. While for lower value of $WeRe^{-2/5}$ ($WeRe^{-2/5} < 10$), $\xi_{max}/Re^{1/5}$ varies with $(WeRe^{-2/5})^{1/2}$, or $\xi_{max} \sim We^{1/2}$ with subtle simplification. This function $\xi_{max} = Re^{1/5} f(WeRe^{-2/5})$ has provided smooth crossover between the inertial and viscous regimes based on many experimental results [52].

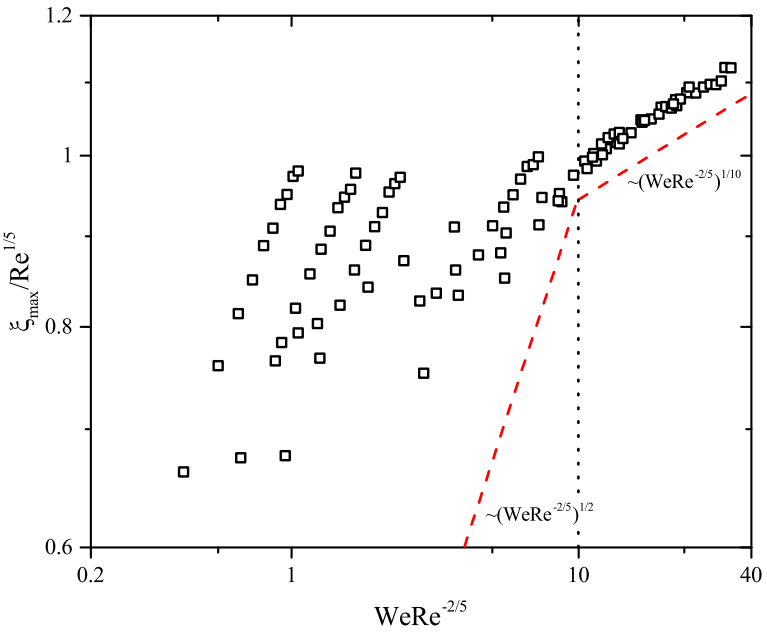

FIGURE **3.4**: The maximum spreading factor ξ_{max} normalised by $Re^{0.2}$ as a function of $WeRe^{0.4}$.

The purely non-wetting property of the surface, or the difference $D_{max} - D_{c\_max}$ attributes to this fitting failure, especially for the case where the impact velocity is small and the dynamic viscosity is large. Then, the maximum contact diameter ξ_{c_max} from our simulations is plotted versus the impact number $WeRe^{-2/5}$ in Fig.3.5. Compare the two subfigures (a) and (b) and observe that the maximum contact factor is slightly smaller than the maximum spreading factor, the difference $\xi_{max} - \xi_{c\_max}$ becomes apparent in the range $We < 5$ and $WeRe^{-2/5} < 10$ (red hollow squares). The difference $\xi_{max} - \xi_{c\_max}$ is plotted versus We in Fig.3.6, and decreases with the increasing Weber number. The difference $\xi_{max} - \xi_{c\_max}$ scale as an exponential function in terms of We as $\xi_{max} - \xi_{c\_max} = 0.3We^{-1/4}$. After eliminating the difference $\xi_{max} - \xi_{c\_max}$ from ξ_{max}, the maximum contact factor ξ_{c_max} is fitted well by

$$\xi_{c\_max}/Re^{1/5} = 0.686(WeRe^{-2/5})^{0.13}, \tag{3.3}$$

where the constant 0.686 and the exponent 0.13 are fitting constants obtained with adjusted R-Square $R^2 = 0.95$, and this function is plotted as the red dash line in (b) in Fig.3.5. Recall the first-order Padé approximation Eq.(3.2), a similar Padé approximation also provides good fitting with adjusted R-Square $R^2 = 0.95$, shown as the red dash line in Fig.3.7.

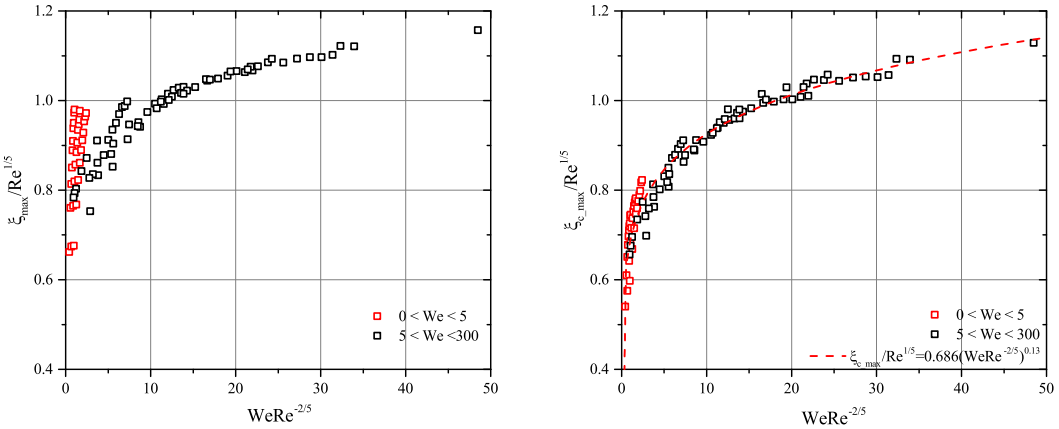

FIGURE **3.5**: The maximum spreading factor ξ_{max} (a) and the maximum contact factor ξ_{c_max} (b) normalised by $Re^{0.2}$ as a function of $WeRe^{-2/5}$.

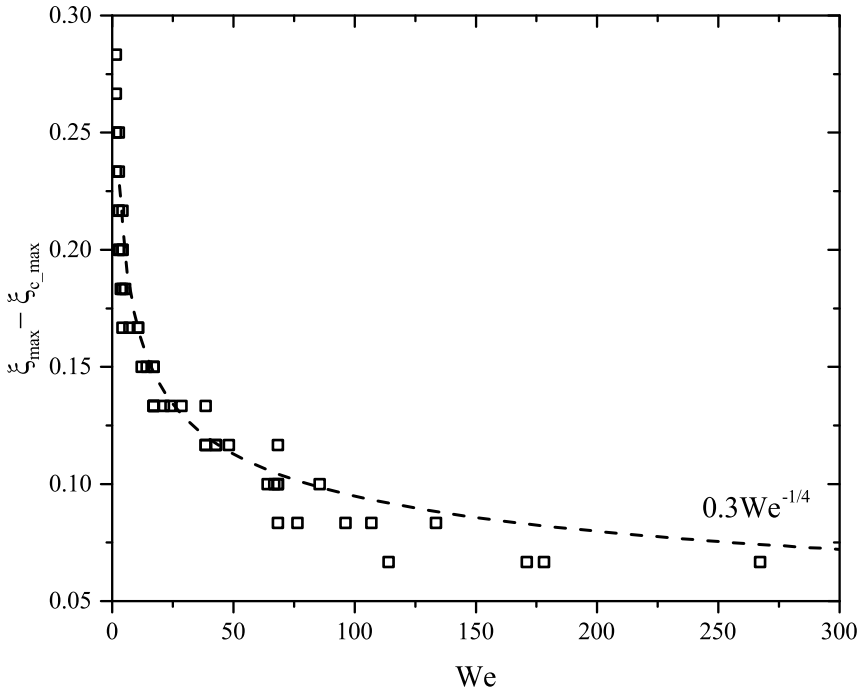

FIGURE **3.6**: The difference between maximum spreading factor ξ_{max} and the maximum contact factor ξ_{c_max} plotted versus Weber number.

The investigations on maximum contact diameter D_{c_max} are limited, compared to the works on the maximum spreading diameter D_{max}. The experimental results obtained by impacting water-glycerol droplets on parafilm surface (hydrophobic) by Bartolo *et al.* [8] are visited and

replotted in Fig.3.7. The experimental results not only maintain the scale tendency (given by the dash lines), but also coincides well with the results from our numerical simulations.

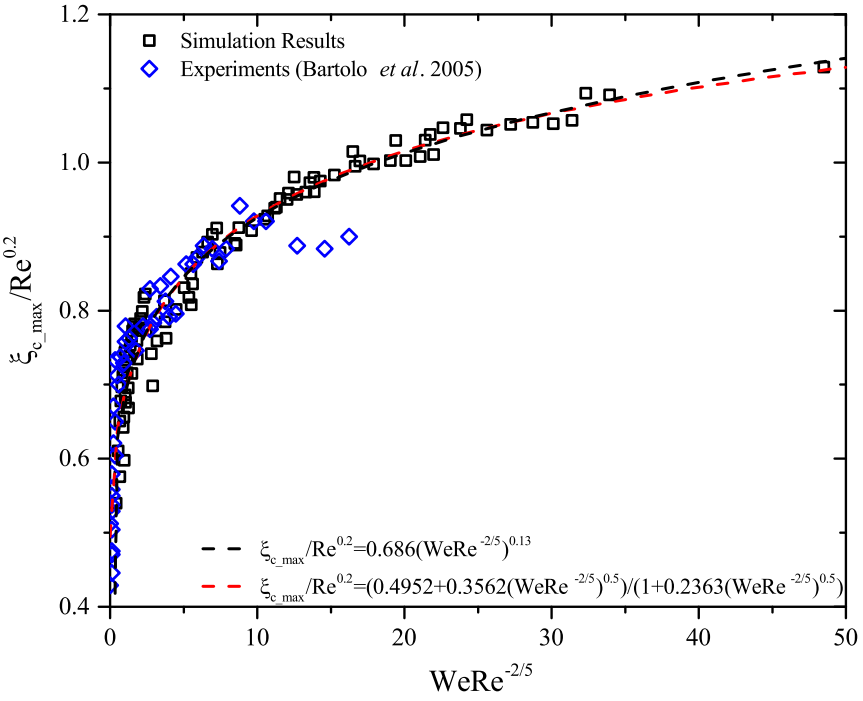

FIGURE **3.7**: The maximum contact factor ξ_{c_max} normalised by $Re^{1/5}$ as a function of $WeRe^{2/5}$.

Concerning the influences of contact angle on maximum spreading, Lee *et al.* [57] proposed an universal rescaling of droplet impact on wetting and non-wetting surfaces, smooth and rough surfaces. They observed that the dynamic wetting has large impact on the spreading at low velocity. And the dynamic wettability is taken into account by considering the surface energy at zero impact velocity , which relates to the spreading factor at zero velocity. Based on the assumption that the spreading droplet maintains the truncated-sphere shape and keeps a constant volume, the spreading factor $\xi_{V_0\to 0} = D_{V_0\to 0}/D_0$ could be expressed in terms of the contact angle $\theta_{V_0\to 0}$,

$$\xi_{V_0\to 0} = \begin{cases} \left(\frac{4sin^3\theta_{V_0\to 0}}{2-3cos\theta_{V_0\to 0}+cos^3\theta_{V_0\to 0}}\right)^{1/3}, & \text{if } \theta_{V_0\to 0} < 90°, \\ \left(\frac{1}{(2+cos\theta_{V_0\to 0})sin^4(\theta_{V_0\to 0}/2)}\right)^{1/3}, & \text{if } \theta_{V_0\to 0} > 90°, \end{cases} \tag{3.4}$$

for a hydrophilic surface $(\theta_{V_0\to 0} < 90°)$ and a hydrophobic surface $(\theta_{V_0\to 0} > 90°)$, respectively. After adding the capillary energy $E_{S0} \sim \sigma D^2_{V_0\to 0}$ in the low-velocity limit, the modified energy

balance becomes,

$$\rho D_0^3 V_0^2 + \sigma D_{V_0\to 0}^2 = \sigma D_{max}^2, \tag{3.5}$$

which gives

$$\sqrt{\xi_{max}^2 - \xi_{V_0\to 0}^2} = We^{1/2}. \tag{3.6}$$

Combine Eq.(3.6) proposed by Lee *et al.* [57] and the first-order Padé approximation Eq.(3.2) [52] and obtains,

$$\left(\xi_{max}^2 - \xi_{V_0\to 0}^2\right)^{1/2} Re^{-1/5} = \frac{We^{1/2}}{A + We^{1/2}}, \tag{3.7}$$

where A is a fitting constant.

Recall that the simulations presented in this chapter are performed under the condition that the target surface is purely non-wetting. Substitute $\theta = 170^\circ$ into Eq.(3.4), we obtain

$$\xi_{V_0\to 0} \approx 1, \tag{3.8}$$

then the raio $\left(\xi_{max}^2 - 1\right)^{1/2} / Re^{1/5}$ is plotted versus $WeRe^{-2/5}$ in Fig.3.8, together with the maximum contact factor ξ_{c_max}. The rescale function $\left(\xi_{max}^2 - \xi_{V_0\to 0}^2\right)^{1/2}$ rescale ξ_{max} nicely for low-velocity impact in the range $WeRe^{-2/5} < 10$. The data points in the blue rectangle, which are performed with higher impact velocity and viscosity, deviate relatively largely from the black fitting line. These deviations are caused by the overestimations of the influences of wettability in the viscous regime (high impact velocity, high viscosity). The error bars presented in Fig.3.8 are the difference between the values of our simulations and the estimated values provided by the fitting function.

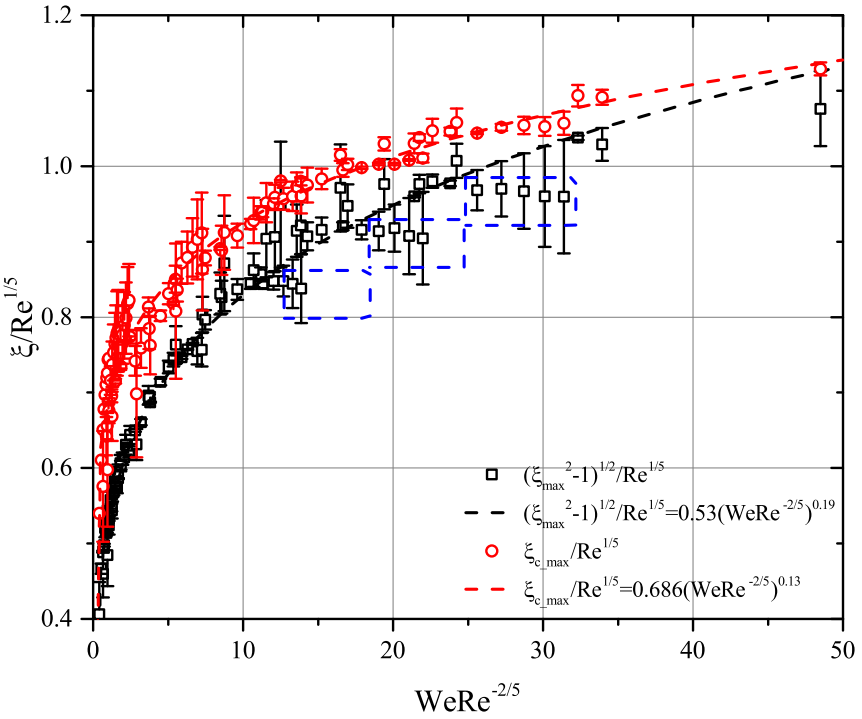

FIGURE **3.8**: The maximum spreading factor ξ_{c_max} and $(\xi_{max}^2 - 1)^{1/2}$ normalised by $Re^{1/5}$ plotted versus $WeRe^{-2/5}$.

In this section, we first go through the works on the maximum spreading diameter: the capillary regime at low impact velocity, the viscous regime at high impact velocity and the broad cross-over regime between the low and high impact velocities by interpolating between $We^{1/2}$ and $Re^{1/5}$. As the ξ_{max} from our simulations performed under purely non-wetting conditions failed to scale with the cross-over between capillary and viscous regimes, ξ_{max} scales with $We^{1/2}$ when $WeRe^{-2/5} < 10$ and with $(WeRe^{-2/5})^{1/10}$ in the range $10 < WeRe^{-2/5} < 40$. We conclude that this is due to the difference $\xi_{max} - \xi_{c\_max}$, or the rim radius. We found that the rim radius $\xi_{max} - \xi_{c\_max}$ scales as $\sim 0.3We^{-1/4}$ and showed $\xi_{max} - \xi_{c\_max}$ had large impact on maximum spreading diameter at low Weber number. For the droplet impacting on purely non-wetting surfaces, the wettability plays a significant role on the spreading when the impact velocity is small. A comparison is given between the maximum contact factor and the rescaled function $\left(\xi_{max}^2 - \xi_{V_0 \to 0}^2\right)^{1/2}$ considering the influences of wettability by Lee *et al.* [57]. The difference $\xi_{max} - \xi_{c\_max}$ is caused by the droplets' dynamic wetting behaviour at low impact velocity.

3.2 The Maximum Spreading Time t_{max}

The significance of studying the maximum spreading time t_{max} not only lies in describing the spreading behaviour of the droplet, but also in the calculation of the viscous dissipation energy (integrated over time to the point of maximum spreading). The maximum spreading time is defined as the time when the rim of the splat begin to recoil towards the centre of the splat. In the early studies, Pasandideh-Fard *et al.* [72] derived the time at maximum spreading as,

$$t_{max} = (8/3) \cdot D_0/V_0, \tag{3.9}$$

based on the simple geometric assumption that the splat at maximum spreading is approximated by a cylinder. Lee *et al.* [56] conducted experiments to show that the maximum spreading time t_{max} decreases with impact velocity and proposed a new scaling of t_{max} with maximum spreading factor ξ_{max} and surface tension as

$$t_{max} = bD_0\xi_{max}/V_0, \tag{3.10}$$

where parameter b equals to the ratio of surface tension of droplet liquid to a reference liquid. And recently, Huang and Chen [40] compared their experimental results with these two relations Eq.(3.9) and Eq.(3.10). The comparison shows that the dimensionless maximum spreading time can not be seen as constant, and the difference between prediction Eq.(3.10) and experimental results become larger with the increase of Weber number.

This section starts with the influences of droplet's physical properties on the maximum spreading time t_{max}. The droplet's major physical properties are the impact velocity V_0, surface tension σ and dynamic viscosity μ. The contact angle we applied between the droplet and the surface is set as $170°$, i.e., the droplet impacts on a purely non-wetting surface. Then, after studying the influences of droplet's physical properties on t_{max}, the effects of the contact angle condition are taken into consideration.

3.2.1 The influences of impact velocity, surface tension and dynamic viscosity on t_{max}

Here, we first investigate the influences of the physical properties of the droplet on the maximum spreading time t_{max}. The results of the maximum spreading time t_{max} after *Step 1* are presented

in Fig.3.9. The Fig.3.9 presents that t_{max} scales as an exponential function of V_0,

$$t_{max} \sim V_0^{-0.35}. \tag{3.11}$$

For the case of lower velocities ($V_0 = 3, 4, 5m/s$), the influences of dynamic viscosity on the maximum spreading time could be ignored compared to those for higher velocities ($V_0 = 10 \sim 25m/s$). In the cases with higher impact velocity higher Weber number, the effects of dynamic viscosity could not be ignored, the maximum spreading time decreases as the dynamic viscosity μ increases. The explanation could be said as for higher Weber number, as the droplet spreads much larger, the viscous dissipation during spreading becomes an important role in countering the inertia of the droplet.

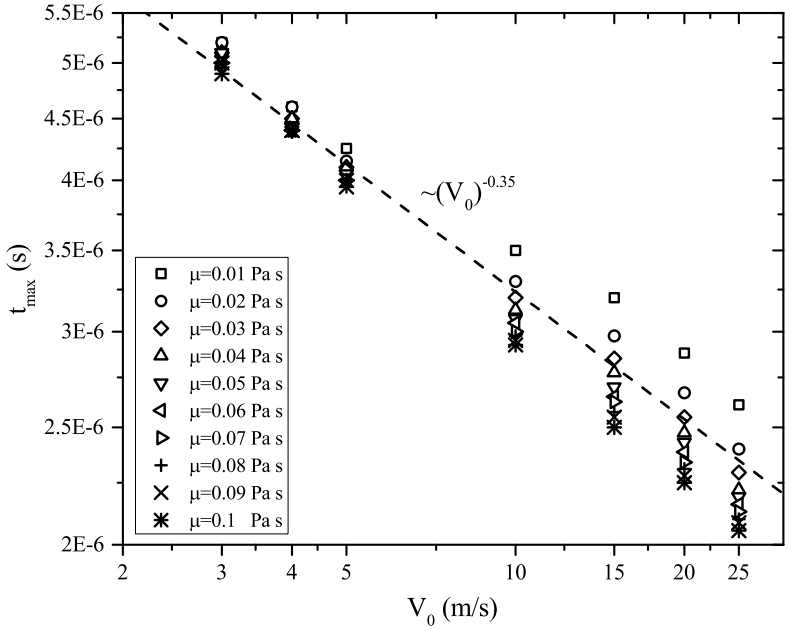

FIGURE **3.9**: The maximum spreading time t_{max} for the droplets with varying dynamic viscosity impacting on purely non-wetting surfaces at velocities from $3\ m/s$ to $25\ m/s$.

Then, the results in Fig.3.9 are normalised and replotted against the Reynolds number, presented in Fig.3.10. The dimensionless maximum spreading time t^*_{max} remains largely dependent on the impact velocity (Weber number). For the results in the cases with lower Weber number ($We < 5$), the exponent of Re is in order of 0.02. The results obtained with higher Weber

number ($We > 5$) show that

$$t^*_{max} \sim Re^{0.1}. \tag{3.12}$$

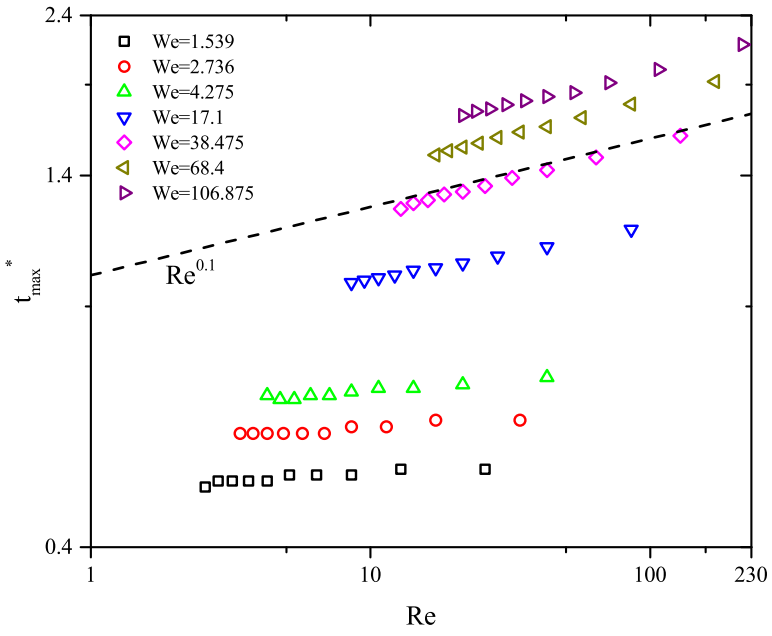

FIGURE **3.10**: The dimensionless maximum spreading time t^*_{max} plotted against Reynolds number for the droplets with varied dynamic viscosity impacting on purely non-wetting surfaces.

Next, plot t_{max} as a function of the surface tension coefficient, as presented in Fig.3.11. The droplet with higher surface tension takes shorter time to reach its maximum spreading state. In logarithmic scales, the data in each case could be well fitted by exponential functions presented in Table.3.1.

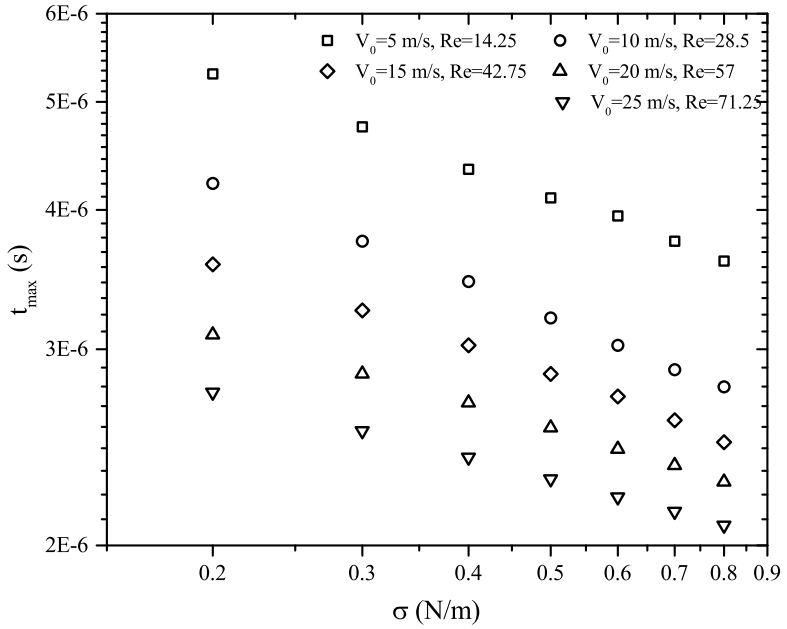

FIGURE **3.11**: The time t_{max} for the droplet to reach its maximum spreading state plotted against different values of surface tension coefficient σ. The Weber number is in the range of $2.18 \sim 267.2$.

TABLEAU **3.1**: The fitting functions of $t_{max} \sim f(\sigma)$ in Fig.3.11 .

V_0, Re	$f(\sigma)$
$5m/s, 14.25$	$t_{max} = 10^{-5.46891} \cdot \sigma^{-0.27628}$
$10m/s, 28.5$	$t_{max} = 10^{-5.58697} \cdot \sigma^{-0.30665}$
$15m/s, 42.75$	$t_{max} = 10^{-5.62672} \cdot \sigma^{-0.26278}$
$20m/s, 57$	$t_{max} = 10^{-5.66104} \cdot \sigma^{-0.21959}$
$25m/s, 71.25$	$t_{max} = 10^{-5.69936} \cdot \sigma^{-0.19795}$

Normalise the results in Fig.3.11 and plot them versus Weber number in Fig.3.12. In logarithmic scale, the dimensionless maximum spreading time t^*_{max} scale well as an exponential function of We.

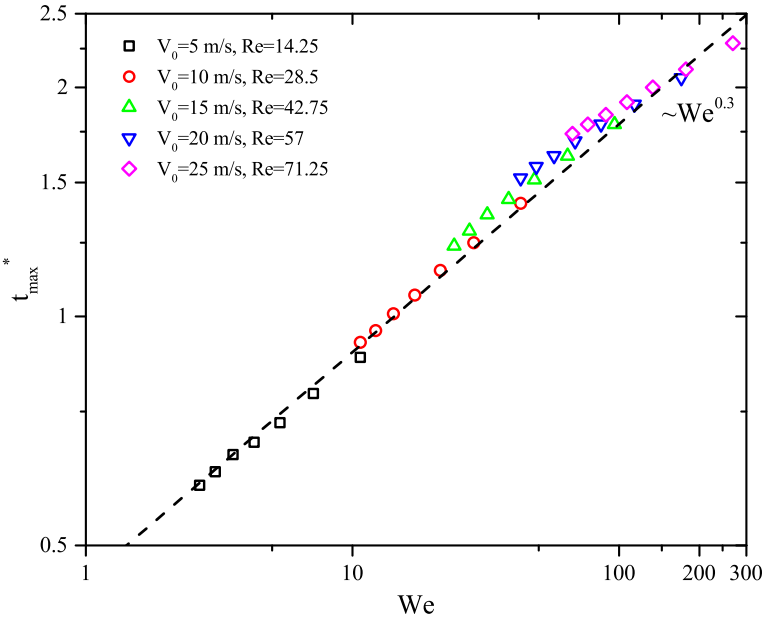

FIGURE **3.12**: The dimensionless maximum spreading time t^*_{max} plotted against Weber number for the droplets with varied surface tension impacting on purely non-wetting surfaces.

Based on these two figures Fig.3.10 and Fig.3.12, we observe that the dimensionless maximum spreading time t^*_{max} is an exponential function in terms We and Re. Recall the crossover function $Re^{-1/5} \cdot (WeRe^{-2/5})$ used to scale the maximum spreading factor, and plot the maximum spreading time results in Fig.3.10 and Fig.3.12 as $t^*_{max}/Re^{1/5} \sim WeRe^{-2/5}$, shown in Fig.3.13,

$$t^*_{max}/Re^{1/5} = 0.375(WeRe^{-2/5})^{0.264}. \tag{3.13}$$

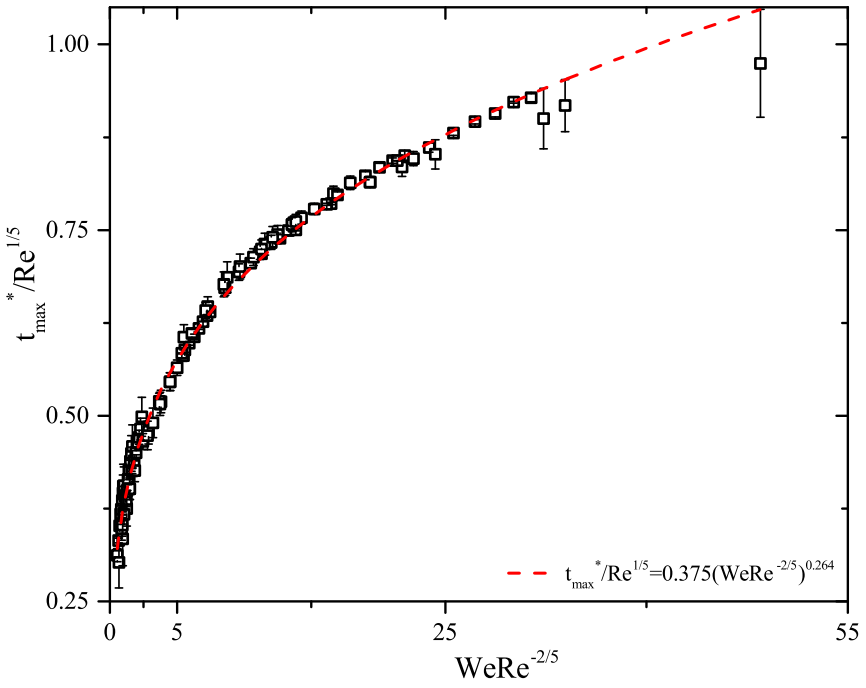

FIGURE **3.13**: The function $t^*_{max}/Re^{1/5}$ plotted versus the impact number $P = WeRe^{-2/5}$. All the data shown in Fig.3.10 and Fig.3.12 are included.

To validate this relation Eq.(3.13) we obtained, the experimental results of maximum spreading time in literature measured by Lee *et al.* [56] and Huang and Chen [40] are rescaled and replotted in Fig.3.14. Lee *et al.* [56] measured the maximum spreading time of ethanol, water and glycerol droplet on steel surface. On steel surface, ethanol maintains a dynamic contact angle ranging from $41°$ to $63°$ and wets the surface. While the water and glycerol maintains an obtuse contact angle between $93°$ and $121°$ and are dynamically nonwetting. Huang and Chen [40] measured the maximum spreading time of water droplet impacting onto parafilm surface with contact angle $110° \pm 7°$. In Fig.3.14, for clearness, only the Eq.(3.13) observed from our simulations is plotted. The experimental results measured from, water and glycerol droplets impacting onto steel surfaces, and water droplets impacting onto parafilm, coincide into a line which follows the Eq.(3.13). The spreading time measured from ethanol droplets impacting on steel surface are higher than the ones obtained on hydrophobic surfaces. Lee *et al.* [56] concluded that ethanol's lower surface tension attributed to its higher maximum spreading time than the one of water and glycerol. While as the numerical simulations we performed have taken the effects of the variation of surface tension on spreading time into consideration, we

draw the conclusion that the differences are caused by the different wettabilities.

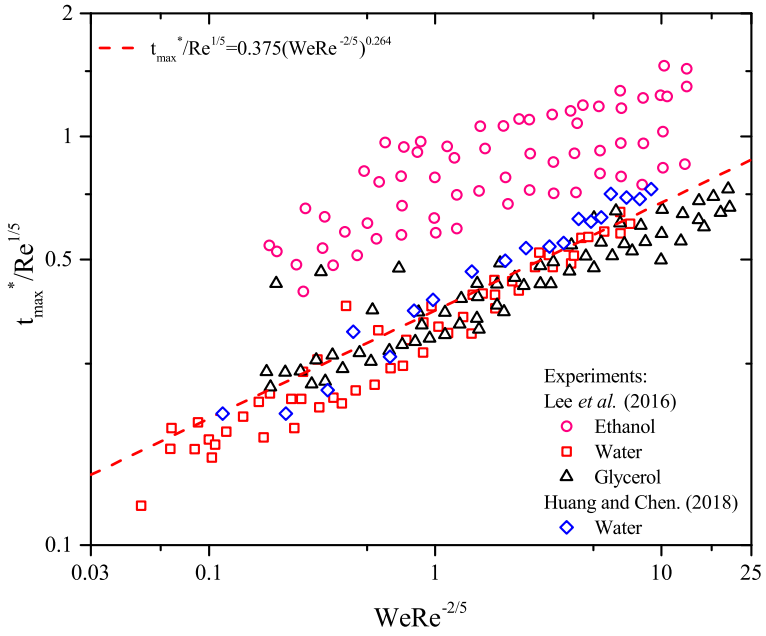

FIGURE **3.14**: Comparison between the scaling relation Eq.(3.13) and experimental results. The symbols represent experimental results from the works of Lee *et al.* [56] and Huang and Chen [40].

To conclude, our prediction of maximum spreading time obtained from droplets impacting on purely non-wetting surfaces fits well with experimental results obtained on hydrophobic surfaces $\theta > 90°$. For the experiments done on wetting surfaces, our prediction largely underestimates the maximum spreading time t_{max}. We postulate that the dimensionless spreading time t^*_{max} scales with no dependence on Reynolds number at low impact velocity, while scales with $Re^{1/10}$ at large impact velocity. The dimensionless maximum spreading time scales with the dependences of $We^{3/10}$ in the range of the Reynolds number, $Re < 300$. Inspired from the cross-over for ξ_{max} between capillary and viscous regimes, we found that the interpolation between $We^{1/2}$ and $Re^{1/5}$ provides a smooth cross-over for t^*_{max} as well.

3.3 The Correlation Between Maximum Spreading Diameter D_{max} and Spreading Time t_{max}

As investigated in previous sections, the maximum contact factor ξ_{c_max} and maximum spreading time t^*_{max} have been investigated systematically, and they both scale as the function $Re^{1/5} \cdot f(WeRe^{-2/5})$, Eq.(3.3) and Eq.(3.13), respectively. In the theoretical works predicting the maximum spreading diameter by energy conservation, the maximum spreading time t_{max} plays a significant role in calculating the dissipation work accumulated in spreading stage. The works predicting ξ_{max} theoretically, mainly used two models for the maximum spreading time t_{max}. The relation Eq.(3.9) by Pasandideh-Fard *et al.* [72] gives a constant $t^*_{max} = 8/3$. Lee *et al.* [56] proposed a relation $t_{max} = bD_{max}/2V_0$ and claimed that it fits well with their experimental results.

After the separate investigation on the maximum spreading factor and maximum spreading time, we try to establish the correlation between ξ_{max} and t^*_{max}. In Fig.3.15, the ratios ξ_{c_max}/t^*_{max} and ξ_{max}/t^*_{max} are plotted versus the Weber number. The black squares represent the data obtained with the variations of impact velocity and surface tension, the blue diamond represent the data obtained with the variations of impact velocity and viscosity. Regardless of the influences of viscosity with higher velocity, the ratios could be fitted nicely by

$$\frac{\xi_{c\_max}}{t^*_{max}} = 2We^{-0.1}, \qquad \frac{\xi_{max}}{t^*_{max}} = 2.44We^{-0.14}, \tag{3.14}$$

where the difference between these two equations are minor and could be neglected. Further, Eq.(3.14) have not taken the effects of viscosity into account when rescale the ratio between maximum spreading diameter and maximum spreading time. To account the minor effects of viscosity and surface tension at the same time, Eq.(3.14) are rescaled and presented as,

$$\frac{\xi_{c\_max}/t^*_{max}}{Oh^{0.2}} = f\left(Oh \cdot \left(WeRe^{-2/5}\right)^{1/2}\right), \tag{3.15}$$

where the influence of Reynolds number is much lower than the Weber number. The Eq.(3.15) serves as a rescale function which could rescale the results where the dynamic viscosity has an impact on ξ_{max}/t^*_{max}.

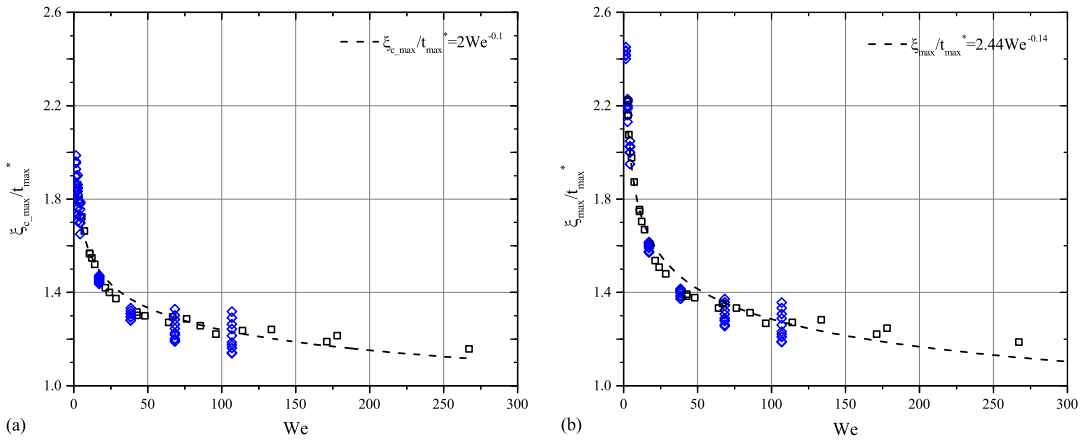

FIGURE **3.15**: (a) The ratio ξ_{c_max}/t^*_{max} versus Weber number. (b) The ratio ξ_{max}/t^*_{max} versus Weber number.

Then, the ratios ξ_{c_max}/t^*_{max} presented in Fig.3.15 (a) are rescaled with Eq.(3.15) and plotted in Fig.3.16 (a) with a fitting function provided by

$$\frac{\xi_{c\_max}/t^*_{max}}{Oh^{0.2}} = 1.7\left(Oh(WeRe^{-2/5})\right)^{-0.2278}, \tag{3.16}$$

with adjusted R-square 0.97. The rescaled ratio ξ_{max}/t^*_{max} is also plotted as a function of $Oh(WeRe^{-2/5})$ in Fig.3.16 (b), where the data deviate slightly further from the red dash line (Eq.(3.16)) compared to Fig.3.16 (a).

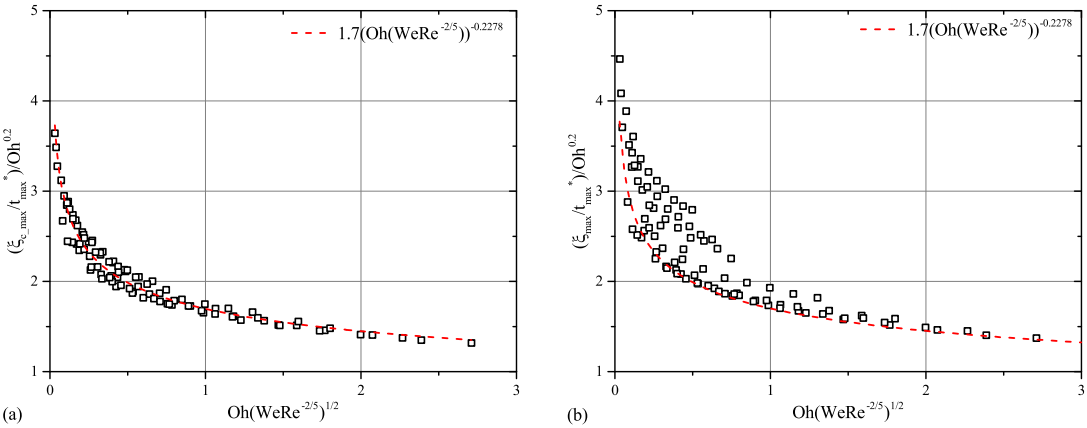

FIGURE **3.16**: (a) The rescaled ratio ξ_{c_max}/t^*_{max} as a function of $Oh(WeRe^{-2/5})$. (b) The rescaled ratio ξ_{max}/t^*_{max} as a function of $Oh(WeRe^{-2/5})$.

The Fig.3.15 and Fig.3.16 show that both these scale functions Eq.(3.14) and Eq.(3.16) provide good fitting to the ratio ξ_{max}/t^*_{max} based on our numerical results, where the maximum spreading factor ξ_{max} and dimensionless spreading time t^*_{max} have been validated with available experimental results in literature, respectively. Further determination between these two correlations should be given by a comparison to the existing experimental results. In Fig.3.17, comparisons between predictions of t^*_{max} and the value of t^*_{max} measured in experiments are presented. The Eq.(3.9) proposed by Pasandideh-Fard *et al.* [72], Eq.(3.10) by Lee *et al.* [56] and Eq.(3.14), Eq.(3.16) observed from our simulations give the predictions of t^*_{max} based on the maximum spreading diameter D_{max} measured from experiments. The subfigures Fig.3.17 (a), (b) and (c) present comparisons based on the experiments performed by Lee *et al.* [56], Fig.3.17 (d) gives the comparisons from the experimental results by Huang and Chen [40]. Lee *et al.* [56] performed the experiments where ethanol, water and glycerol droplet impacting on steel, aluminium and parafilm surfaces, and presented t^*_{max}. The experimental details and conditions of Lee *et al.* [56] and Huang and Chen [40] are given in the Appendix. The Eq.(3.9) proposed by Pasandideh-Fard *et al.* [72] seems unphysical that it assumes the dimensionless spreading time is constant. The Eq.(3.10) improved the predictions by replacing the initial diameter with maximum spreading diameter and considering the influences of surface tension roughly by introducing the ratio of surface tension of droplet liquid to water. While the difference between the experimental results and the the predictions by Eq.(3.10) increases with the increase of Weber number. The Fig.3.17 show that the two scale functions Eq.(3.14) and Eq.(3.16) both agree with the experiments qualitatively well, improve the accuracy of the predictions, especially the Eq.(3.14).

Compared the goodness of fitting with these rescale functions Eq.(3.14) and Eq.(3.15) to ratios ξ_{c_max}/t^*_{max} and ξ_{max}/t^*_{max}, the correlation between ξ_{max} and t^*_{max} is set as

$$\frac{\xi_{max}}{t^*_{max}} = 2We^{-0.1}. \tag{3.17}$$

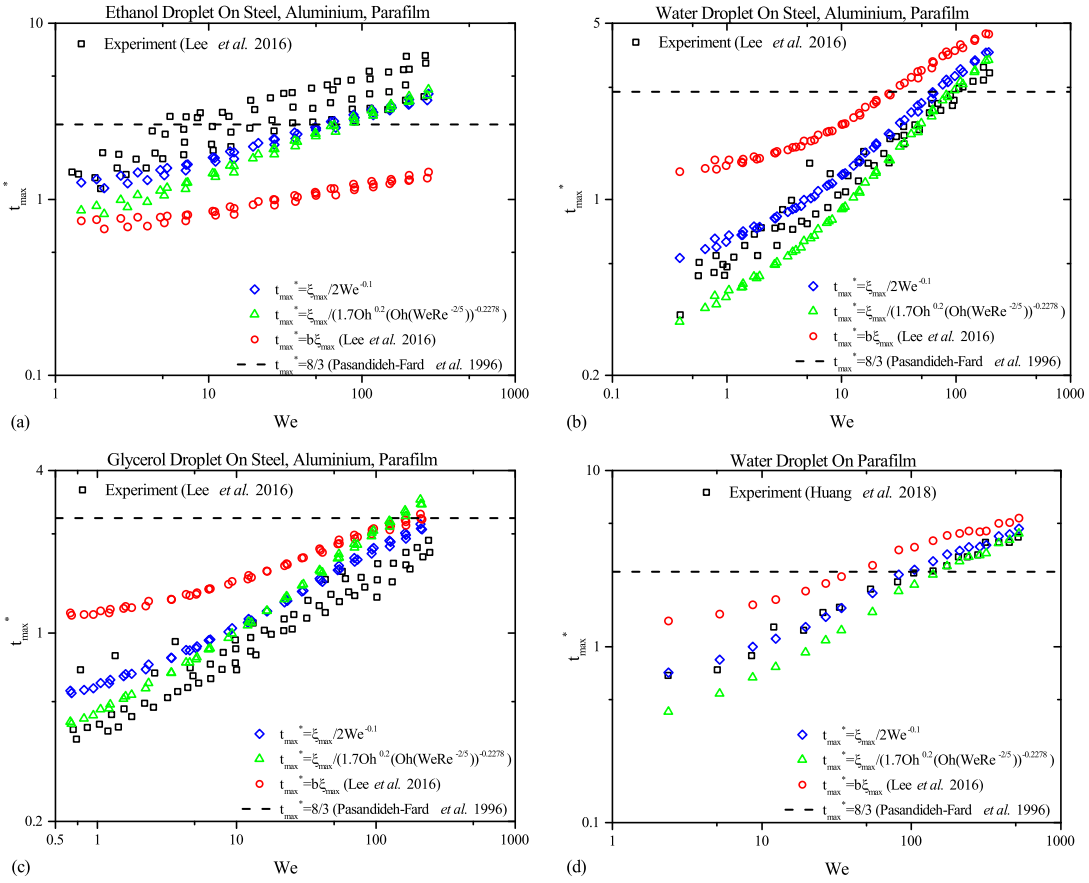

FIGURE **3.17**: Comparison between the prediction of the dimensionless spreading time t^*_{max} and the experiments. (a), (b) and (c) are the experiments performed by Lee *et al.* [56]. (d) are the experiments performed by Huang and Chen [40].

Two correlations between ξ_{max} and t^*_{max} are established based on the results in our simulations: Eq.(3.14) and Eq.(3.16). They both provide nice fitting goodness to the maximum contact factor ξ_{c_max}. Comparisons among Eq.(3.14) and Eq.(3.16), two widely adopted prediction models Eq.(3.9) and Eq.(3.10) and experimental results are presented nicely. With the measured ξ_{max} in experiment. The two predictions Eq.(3.14) and Eq.(3.16) present an apparent improvement on the accuracy of the t_{max} prediction given by Eq.(3.9) and Eq.(3.10), especially the Eq.(3.17). This correlation $\xi_{max}/t^*_{max} = 2We^{-0.1}$ can be used to describe the maximum spreading factor and time of liquid droplets impacting on wetting and non-wetting surfaces from low to high impact velocities.

3.4 Summary

In this chapter we studied the normal impact of liquid droplets on hydrophobic solid surfaces systematically, by considering the influences of impact velocity, surface tension and dynamic viscosity. A systematical and detailed analysis on maximum spreading factor and maximum spreading time is presented. The scaling of the maximum spreading factor ξ_{max}, the dimensionless maximum spreading time t^*_{max}, with the variation of impact velocity, surface tension and dynamic viscosity have been thoroughly investigated. Corresponding scale functions are proposed and validated with available experimental results.

For the maximum spreading factor, detailed analysis of the effects of three physical parameters, V_0, σ and μ, is provided. The two classical scaling, $\xi_{max} \sim We^{1/2}$ in the capillary and $\xi_{max} \sim Re^{1/5}$ viscous regime, are both recovered in our analysis. And we concluded that the interpolation proposed by Laan *et al.* [52] failed to establish a smooth crossover between these two regimes, as the impact of the wettability on the maximum spreading factor could not be neglected when droplets impacting on purely non-wetting surfaces at low impact velocities. To eliminate the effects of the wettabilities, the maximum contact factor ξ_{c_max} is introduced and scales nicely with the interpolation by Laan *et al.* [52]. The difference $\xi_{max} - \xi_{c\_max}$ at low impact velocity is large enough to have an impact on the scaling of the maximum spreading factor. The scale between $\xi_{max} - \xi_{c\_max}$ and Weber number We is observed as $\xi_{max} - \xi_{c\_max} \sim 0.3We^{-1/4}$. Compared to the universal scaling considering the influences of dynamic wettability at low impact velocity, the maximum contact factor provides a better and easier way to eliminate the influences of wettability.

Considering the dimensionless spreading time t^*_{max} that the droplet reaches its maximum spreading extension, t^*_{max} increases as $We^{0.3}$ in the range $1 < We < 300$. While the effects of Reynolds number on t^*_{max} could be neglected at low impact velocity, t^*_{max} scales with dependences $Re^{1/10}$ at high impact velocity. Thanks to the interpolation for ξ_{max} between capillary and viscous regimes, we observed a scale function $t^*_{max}/Re^{1/5} = 0.375\left(WeRe^{-2/5}\right)^{0.264}$, which agrees well with experimental results performed on hydrophobic surfaces but underpredicts the spreading time of droplets spreading on hydrophilic surfaces.

In addition, a correlation between the maximum spreading factor ξ_{max} and t^*_{max} of liquid droplets from low to high impact velocities on wetting and non-wetting surfaces is established.

The strongest conclusion from this chapter is this correlation $\xi_{max}/t^*_{max} = 2We^{-0.1}$, improves the existing predictions and agrees well with the experiments performed on wetting and non-wetting surfaces. This correlation could improves the accuracy of the theoretical predictions based on the energy balance, as the maximum spreading time t_{max} has a large impact on the calculation of the dissipation work accumulated in the spreading stage.

Chapter 4

The Droplets' Bouncing-Off State On Superhydrophobic Substrates

Apart from the applications plasma spray, ink printing, etc ... (utilising the deposition outcome of the droplets' impactions), the bouncing-off outcome of impacting droplets have also received substantial attention due to their ability to keep the target surface dry and clean [see e.g., 80, 14, 31]. A droplet impacting onto a non-wetting surface will first spread to a maximum diameter [see e.g., 17, 26, 52, 56], and recoil until it completely leaves the solid surface [8]. The time that the droplet stays in contact with the solid is called contact time, indicated by t_c in this chapter. Similarly, the contact time t_c is normalised as

$$t_c^* = \frac{t_c}{D_0/V_0}, \tag{4.1}$$

for non-dimensional analysis. The contact time could be split into two parts, the maximum spreading time t_{max} and retraction time $t_c - t_{max}$, the time from maximum spreading to the instant at which the droplet bounces off the solid substrate. The inertia, capillarity of the droplet and the surface-liquid interactions determines the contact time t_c. The total contact time t_c, from impact to rebound-off, has significant influences on the mass, momentum, heat and energy transfer between the droplet and target substrate. It is traditionally thought that the rebound-off behaviour of impacting droplets only occur in the cases the target surfaces are special, such as heated beyond the boiling temperature of the impacting droplets or superhydrophobic. Antonini *et al.* [2] pointed out that rebound can be observed only on surfaces on which the receding contact angle is greater than 100° and the contact time decreases with higher receding contact

angle.

Regarding the contact time between droplet and surface when the retractions are in the capillary-inertial regime, Okumura *et al.* [71] and Richard *et al.* [80] speculated the contact time scales as $(\rho R_0^3/\sigma)^{1/2}$ under the condition that the restitution coefficient ϵ reaches 0.9. The contact time, in the capillary-viscous regime in which the dissipation is important, needs to be investigated. In the literature, most of the works concerning reducing the contact time of impacting droplets focus on tailoring the surface microstructure [see e.g., 58, 14, 31, 79]. Impacting onto micro-patterned surfaces, the capillary energy stored in the liquid penetrating between pillars promotes the lift of the drop. Weisensee *et al.* [111] investigated droplets' impact onto elastic superhydrophobic surfaces experimentally. They found that droplets rebounded off the surface with shorter contact time as the vertical momentum provided by the elastic surfaces to the droplets. Numerical modelling of droplets impacting on superhydrophobic surfaces plays an important role in providing an understanding of complete bouncing-off phenomenon, where the experiments are difficult to be performed. In the available numerical investigations concerning droplet impact, most of them modelled the non-bouncing droplets and the lack of bouncing-off state modelling is significantly noticeable. In this chapter, we present a systematically numerical analysis on the traditional contact time t_c between droplets and superhydrophobic surfaces. The sample fluid is chosen as the molten ceramic. Then, vary the surface tension ($0.2 \sim 0.8$ $N \cdot m^{-1}$) and dynamic viscosity ($0.01 \sim 0.1$ $Pa \cdot s$) of the droplet to achieve a comprehensive and complete set of data from low to high impact velocity ($3 \sim 25$ m/s) in order to analyse their influences on the contact time. Most of the numerical simulations are carried out with the condition that the target surface is superhydrophobic ($\theta = 170°$). In the following sections, the contact angle takes the default value of $170°$ unless otherwise specified. In **section 4.1**, the different shapes of the droplets at bouncing-off instant are presented, along with the corresponding geometric shape at maximum spreading state. The mechanism behind the formation of these shapes and the formation of the air-entrapment is also included in this section. Through performing extensive simulations, we investigate the influences of parameters, such as impact velocity V_0, surface tension σ, dynamic viscosity μ and contact angle θ, on the contact time t_c in **section 4.2**. Last, a summary and perspectives will be presented in the end of the chapter.

4.1 Droplet's Geometric Shapes At Bouncing-Off Instant

At first, before detailed investigations on the droplets' bouncing-off state, the droplets' geometric shapes at maximum spreading state and bouncing-off instant are presented in Fig.4.1 and Fig.4.2 to deliver some basic understandings on the droplets' rebounding phenomenon.

In Fig.4.1, the dynamic viscosity μ is varied from $0.01\ Pa \cdot s$ to $0.1\ Pa \cdot s$. Lower dynamic viscosity means lower the dissipation work counted in spreading and recoiling process, and leads to larger maximum spreading factor and higher axial height. While Fig.4.2 presents that a droplet with large surface tension σ has smaller maximum spreading radius as surface energy restricts the droplet to spreading. The height h^* is determined by the total energy of the droplet, not only the surface energy.

In Fig.4.1, there are two different kinds of geometric shapes of the droplet at the bouncing-off instant, the spheroidal one and the peanut shape with a neck. The neck is formed and air is trapped in cases: $We = 17.1$, $Oh = 0.04837$; $We = 38.475$, $Oh = 0.096873$; $We = 68.4$, $Oh = 0.09673$ and $Oh = 0.1451$. The bouncing-off shapes in other cases in Fig.4.1 take the spheroidal shape with no air entrapped inside.

In Fig.4.1 and Fig.4.2, in the cases where the impact velocity V_0 is relatively large and the dynamic viscosity μ is small, several small air bubbles could be spotted inside the droplet and neck is formed at the bouncing-off state.

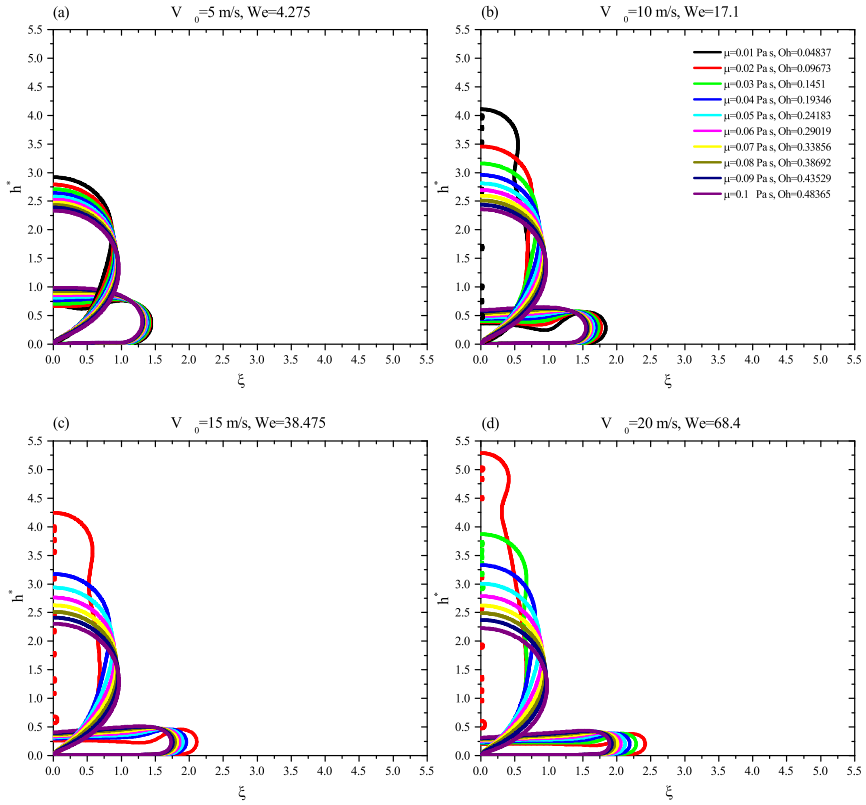

FIGURE **4.1**: The geometric shapes of droplet (with varied dynamic viscosity μ) at maximum spreading state and bouncing-off state. (a) $V_0 = 5\,m/s, We = 4.275$, (b) $V_0 = 10\,m/s, We = 17.1$, (c) $V_0 = 15\,m/s, We = 38.475$, (d) $V_0 = 20\,m/s, We = 68.4$.

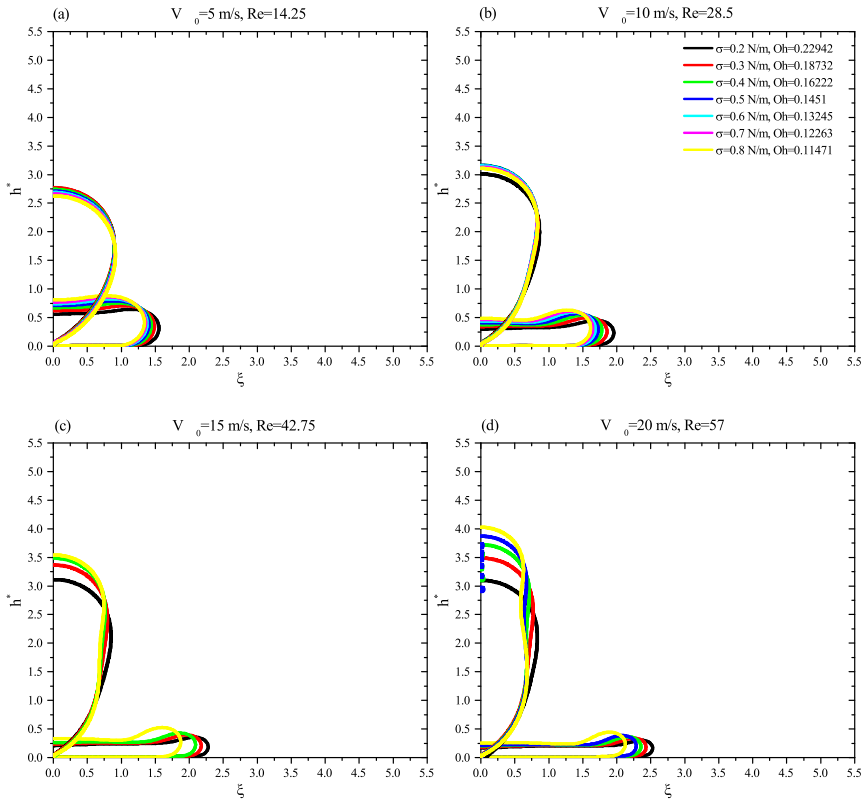

FIGURE **4.2**: The geometric shapes of droplet (with varied surface tension σ) at maximum spreading state and bouncing-off state. (a) $V_0 = 5\ m/s$, $Re = 14.25$, (b) $V_0 = 10\ m/s$, $Re = 28.5$, (c) $V_0 = 15\ m/s$, $We = 42.75$, (d) $V_0 = 20\ m/s$, $Re = 57$.

In order to investigate the physics behind the droplets' different geometric shapes in Fig.4.1 and Fig.4.2, a sequence of pressure and velocity contour inside a droplet, which impacts at $V_0 = 10\ m/s$ on superhydrophobic surface ($We = 17.1$, $Re = 28.5$), are presented in Fig.4.3 and Fig.4.4. The sequence of pressure contour in Fig.4.3 shows that there is no air-entrapment until $t = 6.85e-6\ s$. At $t = 6.85e-6\ s$, air is trapped in a T-shaped composition of cylinder and disk as the top of the splat connect first. Then the air-cylinder breaks into several air-bubbles floating towards the top. The pressure around the air-bubbles are slightly higher than the pressure near the air-bubbles.

The neck presented in the geometric shape is formed due to the distribution of the lift-velocity V_1 field at the neck and nearby (in Fig.4.4). At $t = 8e-6\ s$, the velocity V_1 increases from

the bottom to the top in the droplet. The minimum V_1 takes place at the bottom near the axisymmetric axis. While at $t = 9e-6\ s$, the velocity V_1 decreases and forms a small pit in the velocity contour at the top of the droplet. To $t = 1e-5\ s$, the velocity $V_1 > 8m/s$ contour shapes like a core and forces a neck formed. The velocity vectors plotted in Fig.4.3 and Fig.4.4 are of uniform length and are plotted over every 15 grids to provide a tidy illustration of the dynamics inside the droplet. The pressure and velocity field around the droplet in the gas are also balnked out for clearness.

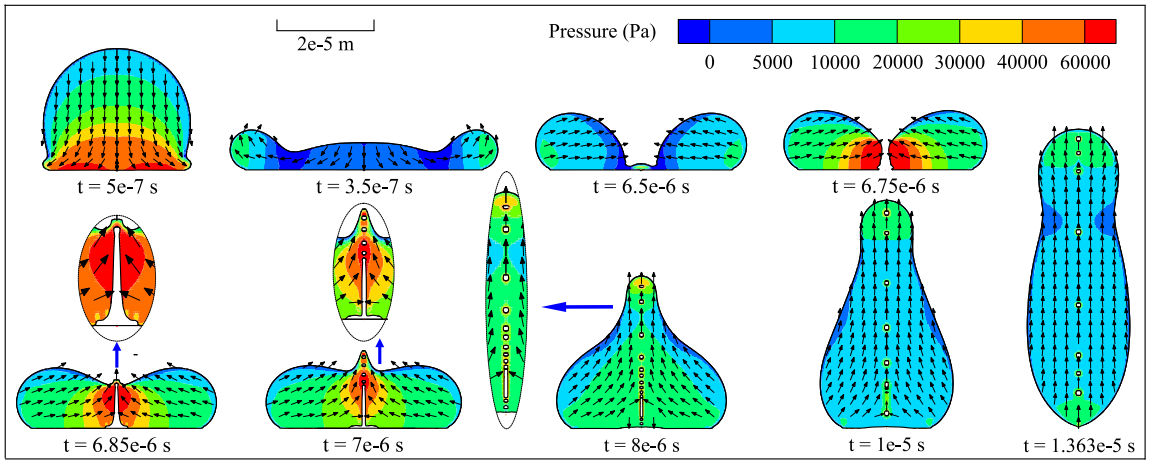

FIGURE **4.3**: The pressure contour P and velocity vector $\mathbf{V}$ in the droplet impacting at $V_0 = 10\ m/s$, $We = 17.1$, $Re = 28.5$. And at $t = 6.85e-6\ s$, $7e-6\ s$, $8e-6\ s$, the regions around the air-bubbles are zoomed.

Besides the fact that we spot air-entrapment in the retraction stage from our simulation resulte, we failed to find any experimental observation in works to support this observation. This air-entrapment may actually exist in the real physics or this air-entrapment is caused due to our axisymmetrical simulations, a numerical air-trapment.

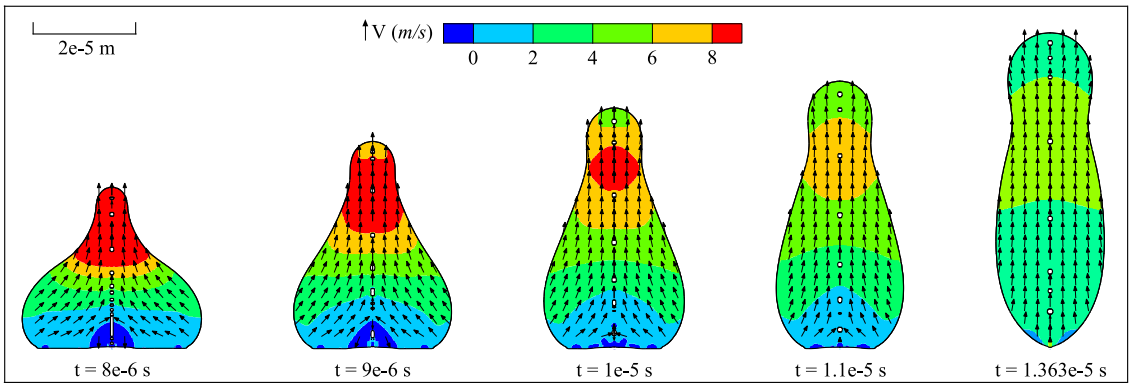

FIGURE **4.4**: The lift-velocity V_1 contour and velocity vector $\mathbf{V}$ inside the droplet during the retraction stage. The droplet impacts at impact velocity $V_0 = 10\ m/s$, $We = 17.1$, $Re = 28.5$ onto superhydrophobic surfaces.

4.2 A scaling function Of Contact Time t_c

This section starts with investigations on the effects of impact velocity, surface tension and dynamic viscosity on contact time t_c, then ends with a proposition of a function scaling contact time in terms of these effects.

4.2.1 The influence of impact velocity V_0

Richard *et al.* [80] investigated the contact time of water drops impacting onto superhydrophobic surfaces and found that the contact time t_c does not depend on the impact velocity over a range of Weber number ($We = 0.3 \sim 37$) in the capillary-inertial regime.

First, the effects of impact velocity on the contact time is investigated. In Fig.4.5, the non-dimensional contact time t_c^* are plotted against the impact velocity V_0, which increases as the increase of impact velocity V_0. The Fig.4.5 presents that, in logarithmic scales, the data are well fitted by a linear line of slope 1.0 ± 0.1 (The fitting functions for each Ohnesorge number in Fig.4.5 are listed in Table.4.1), suggesting that

$$t_c^* = \frac{t_c}{D_0/V_0} \sim V_0, \tag{4.2}$$

which indicates that the contact time t_c does not depend on the impact velocity V_0.

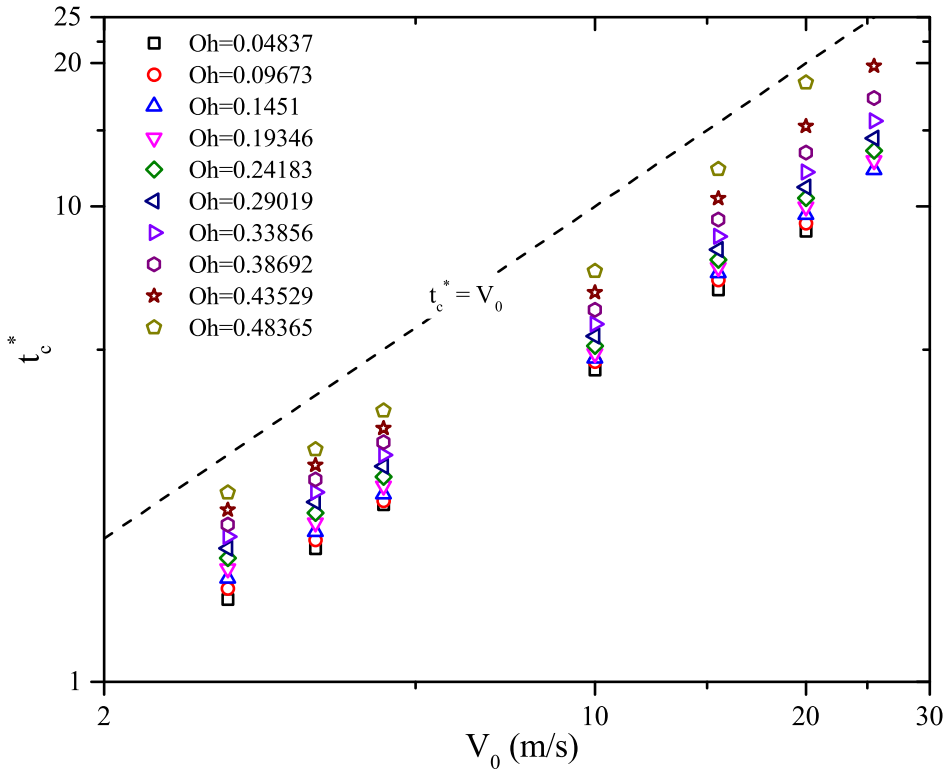

FIGURE **4.5**: The dimensionless contact time t_c^*, contact time normalised by D_0/V_0, as a function of the impact velocity.

TABLEAU **4.1**: The fitting functions in each case with different Ohnesorge number in Fig.4.5.

Oh	$t_c^* \sim f(V_0)$
0.04837	$t_c^* = 10^{-0.28344} \cdot V_0^{0.94271}$
0.09673	$t_c^* = 10^{-0.26661} \cdot V_0^{0.94308}$
0.1451	$t_c^* = 10^{-0.25116} \cdot V_0^{0.94468}$
0.19346	$t_c^* = 10^{-0.23161} \cdot V_0^{0.94172}$
0.24183	$t_c^* = 10^{-0.20921} \cdot V_0^{0.93794}$
0.29019	$t_c^* = 10^{-0.18967} \cdot V_0^{0.94087}$
0.33856	$t_c^* = 10^{-0.17444} \cdot V_0^{0.95346}$
0.38692	$t_c^* = 10^{-0.16219} \cdot V_0^{0.97555}$
0.43529	$t_c^* = 10^{-0.15533} \cdot V_0^{1.01251}$
0.48365	$t_c^* = 10^{-0.13397} \cdot V_0^{1.03945}$

4.2.2 The influence of surface tension σ on contact time t_c

After investigating the effect of the impact velocity V_0 on the contact time t_c, we change the value of the surface tension coefficient σ from $0.2 \sim 0.8\ N \cdot m^{-1}$ to study how the contact time scales versus the surface tension forces, data plotted in Fig.4.6. In Fig.4.6, for the droplets with constant dynamic viscosity $\mu = 0.03\ Pa \cdot s$ and impact velocity V_0 ($5\ m/s \leq V_0 \leq 25\ m/s$), the contact time t_c decreases when increasing the surface tension σ. The increasing surface tension σ would lead to a reduction of the maximum spreading radius. As the maximum spreading radius reduces, the shorter distance for the droplet to travel to bound off from the surface.

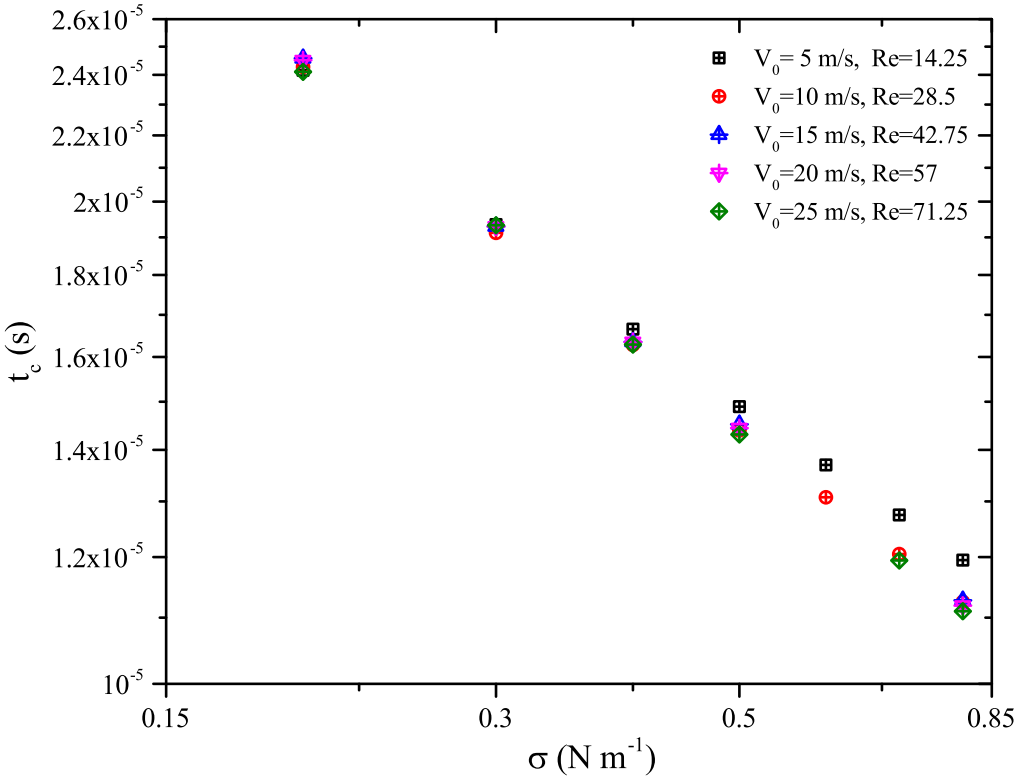

FIGURE **4.6**: The contact time t_c between droplet and surface versus the surface tension coefficient σ. The dynamic viscosity μ is constant ($\mu = 0.03\ Pa \cdot s$), the impact velocity V_0 and the surface tension coefficient σ are varied in a certain range ($2.67 < We < 267$).

TABLEAU **4.2**: The fitting functions in each case with different Reynolds number in Fig.4.6.

$\boldsymbol{Re}$	$\boldsymbol{t_c \sim f(\sigma)}$
14.25	$t_c = 10^{-4.87507} \cdot \sigma^{-0.505}$
28.5	$t_c = 10^{-5.00583} \cdot \sigma^{-0.554}$
42.75	$t_c = 10^{-5.00568} \cdot \sigma^{-0.561}$
57	$t_c = 10^{-5.00884} \cdot \sigma^{-0.566}$
71.25	$t_c = 10^{-5.01055} \cdot \sigma^{-0.562}$

In logarithmic scales, the contact time t_c scales like,

$$t_c \sim \sigma^{-1/2}, \tag{4.3}$$

which serves a strong validation for the speculation of Richard *et al.* [80].

4.2.3 The influence of dynamic viscosity μ on contact time t_c

Next, take the effects of dynamic viscosity μ on contact time into consideration. By keeping the surface tension constant $\sigma = 0.5\ N/m$, the variations of contact time t_c due to the augmentation of dynamic viscosity with different impact velocities are given in Fig.4.7. The dynamic viscosity μ takes the range from $0.01Pa \cdot s$ to $0.1Pa \cdot s$ to achieve the complete rebound outcome. The influences of dynamic viscosity on contact time t_c are significant, increasing the dynamic viscosity will slow down the retraction process as the more surface energy stored at the maximum spreading state is dissipated.

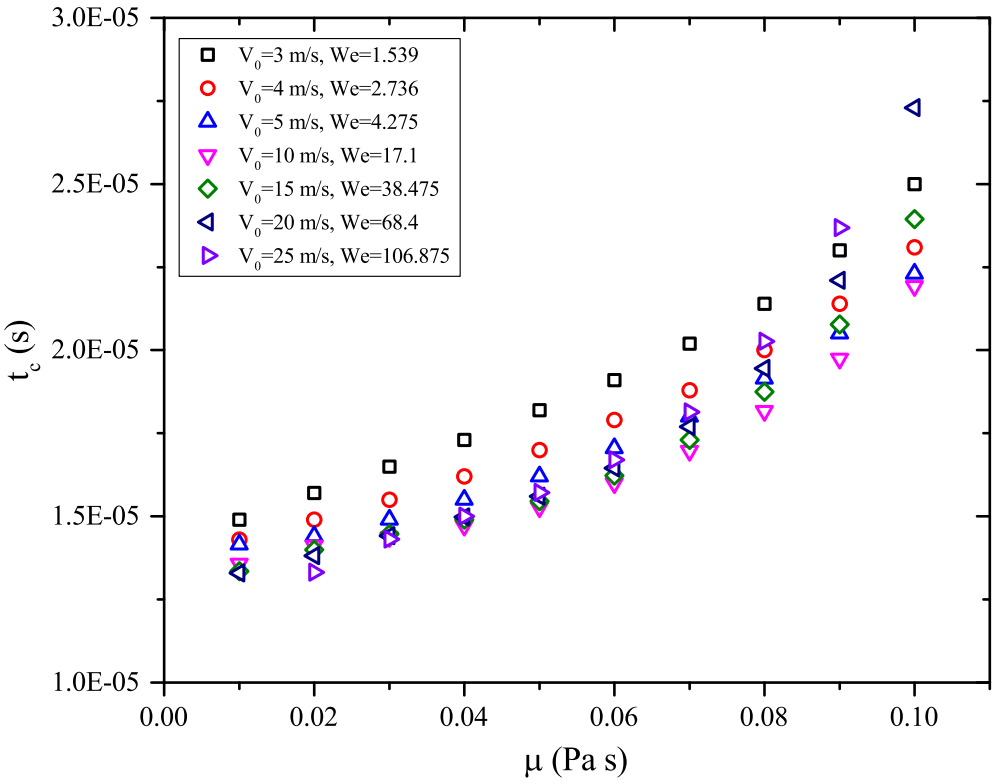

FIGURE **4.7**: The contact time t_c^* plotted with dynamic viscosity μ.

4.2.4 A scale function for contact time

The previous sections in this chapter present the influences of impact velocity V_0, surface tension σ, and dynamic viscosity μ on contact time,

- the contact time t_c is independent on the impact velocity,
- the contact time t_c decreases as the increase of surface tension, and scales as $t_c \sim \sigma^{-1/2}$,
- the contact time t_c is largely influenced by the dynamic viscosity, t_c increases with the augmentation of dynamic viscosity.

Then we assume that t_c scales as a function of surface tension σ and dynamic viscosity μ based on the equations Eq.(4.2) and Eq.(4.3). A scaling function for t_c^* is built as

$$t_c^* = Re \cdot f(Oh), \tag{4.4}$$

where $f(Oh)$ is a function of Ohnesorge number, to quantitatively measure the effects of σ and μ, presented in Fig.4.8. The data presented in Fig.4.5, Fig.4.6 and Fig.4.7 are replotted in Fig.4.8. The dash fitting lines in Fig.4.8 are provided by an exponential function (red) and First-order Padé approximation (black),

$$\frac{t_c^*}{Re} = 10^{0.2815} Oh^{1.22849}, \tag{4.5}$$

$$\frac{t_c^*}{Re} = \frac{0.0141 + 0.8925 Oh}{1 - 1.077 Oh}, \tag{4.6}$$

with error $R^2 > 0.98$. The reason that Padé approximation is provided is for future use to establish a crossover with other different scalings.

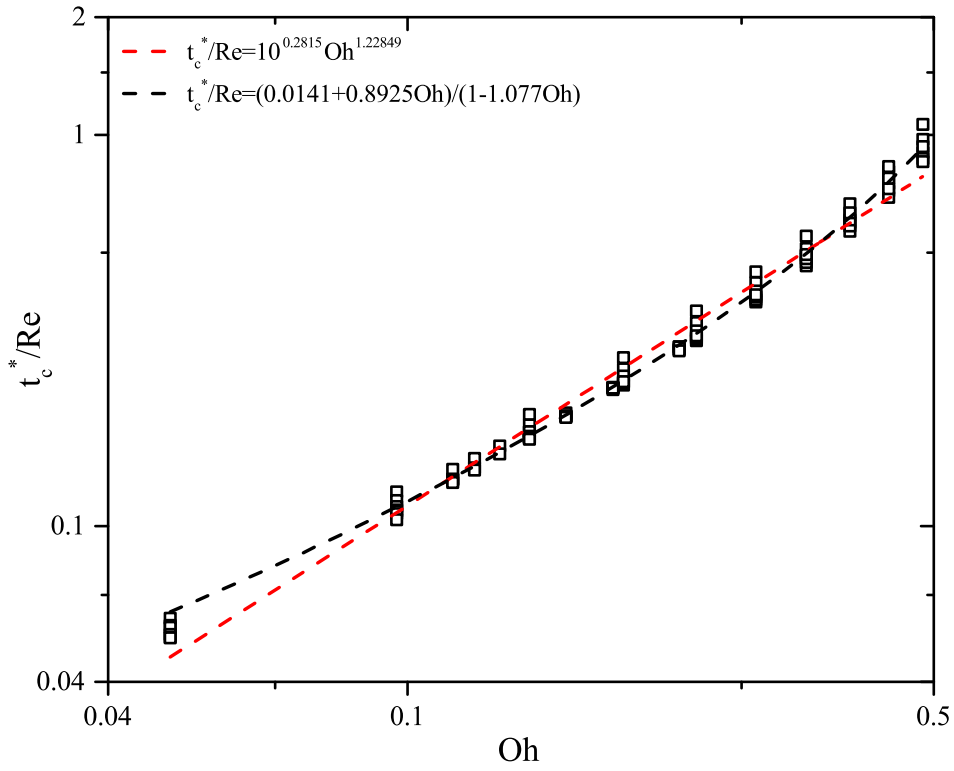

FIGURE **4.8**: The dimensionless contact time t_c^* plotted with Ohnesorge number. The black and red dash lines are the fitting curves plotted by Padé approximation and exponential function, respectively.

4.2.5 The Influence of Contact Angle θ on Contact Time t_c

Based on the investigations on the contact time of droplets impacting onto perfect non-wetting surfaces, we continue to perform numerical simulations of droplets impacting onto hydrophobic surfaces with smaller contact angle to study the influence of contact angle on the contact time t_c^*. The simulations of droplets impacting onto surfaces with contact angle $\theta = 120°, 150°$ are conducted and the contact time data are presented in Fig.4.9. It shows that the variation of contact angle between $150°$ and $170°$ has little influence on the contact time. The contact time obtained on surfaces with $\theta = 120°$ is apparently higher than the ones on surfaces with contact angle ($150° \leq \theta \leq 170°$). With these limited data presented in Fig.4.9, the contact time of a droplet impacting on surfaces with contact angle in the range of $120° - 170°$ takes a similar

tendency versus Ohnesorge number.

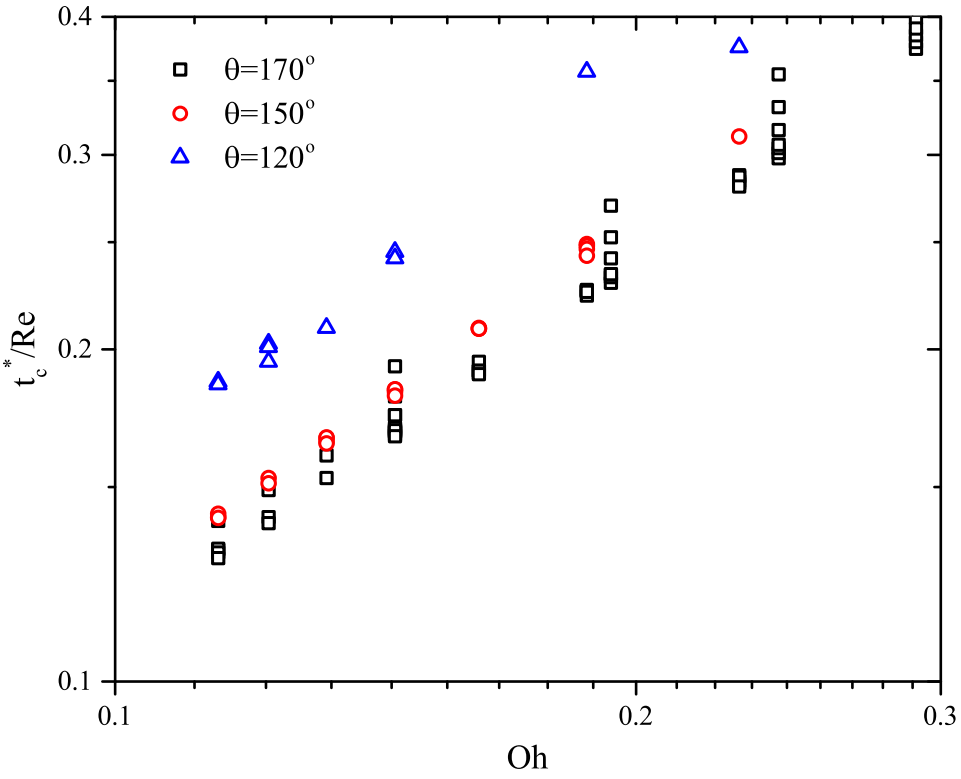

FIGURE **4.9**: The dimensionless contact time t_c^* of bouncing droplet on surfaces with different contact angles $\theta = 120°, 150°, 170°$.

4.2.6 The retraction time t_r

The time for the droplet to travel from its maximum spreading state to its bouncing-off instant is defined as the retraction time t_r,

$$t_r = t_c - t_{max}, t_r^* = t_r V_0 / D_0, \tag{4.7}$$

where t_{max} is the maximum spreading time defined in Chapter 4. The dimensionless retraction time t_r^* is plotted against the Ohnesorge number in Fig.4.10. It shows that the maximum spreading time t_{max}^* has little influence on the whole contact time t_c^* and the retraction time t_r^* shares a similar scale function with the contact time t_c^*.

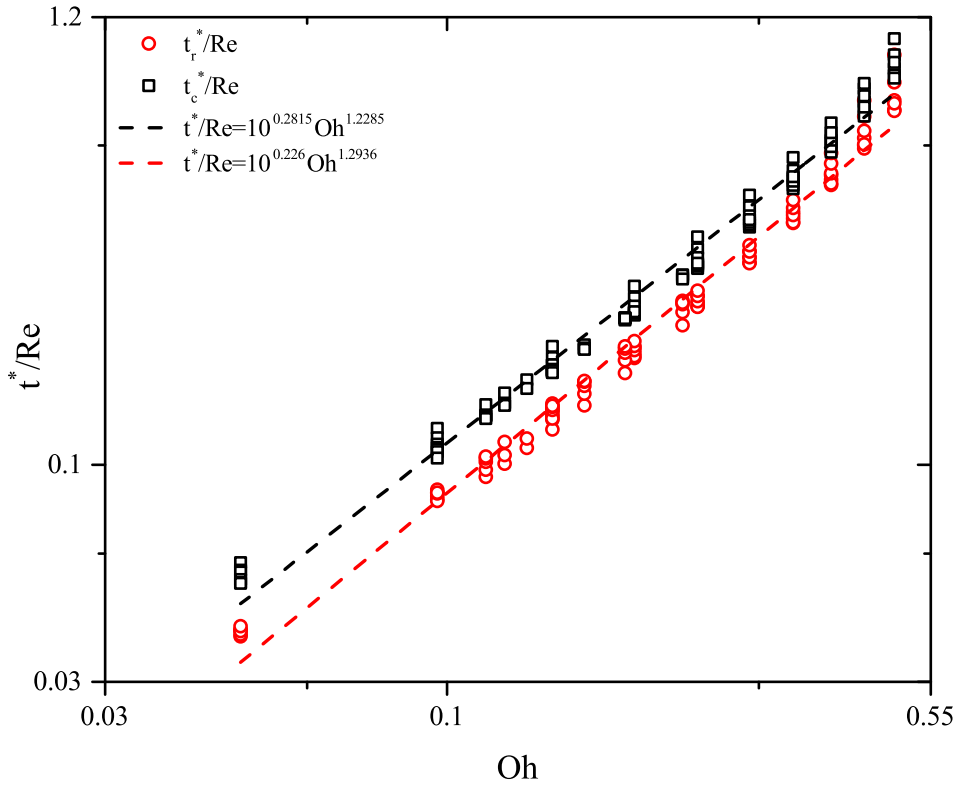

FIGURE **4.10**: The dimensionless contact time t_c^* and retraction time t_r^* plotted with Ohnesorge number.

4.3 Summary

In this chapter, the geometric shapes of droplet at bouncing-off instant are firstly presented, they are classified into two kinds, the spheroidal shape and the peanut shape with air bubbles trapped inside. The air is trapped at the instant that two rims coalesce and its section maintains a T-shape. The cylinder-part of the T-shape entrapment breaks into bubbles and the bubbles float with the upward internal flow, while the air-disk is forced to remain at the surface by the downward internal flows in Fig.4.4. The neck in the peanut shape appears due to the lift-velocity V_1 distribution in Fig.4.3.

The influences of impact velocity V_0, surface tension σ, dynamic viscosity μ on the contact time t_c of the droplets impacting onto superhydrophobic surfaces ($\theta = 170°$) are presented first. The

contact time t_c appears independent on the impact velocity V_0 shown in Table.4.1. Accounting for the effects of the surface tension σ, the contact time t_c scales as $t_c \sim \sigma^{-0.5}$ based on the obtained fitting functions in Table.4.2. For the variations of the dynamic viscosity μ, the contact time t_c increases with the augment of μ. To consider the influences of these three parameters, a scale function in terms of Re and Oh is successfully proposed as

$$\frac{t_c^*}{Re} = 10^{0.2815} Oh^{1.22849}. \tag{4.8}$$

After proposing the scale function for t_c^* on superhydrophobic surfaces, the contact angle between the droplet and surface is varied from $120°$ to $150°$. The contact time obtained on surfaces with $\theta = 120°, 150°$ maintains the same scale function as on purely non-wetting surfaces. The two set data of contact time t_c^* obtained on surfaces with $\theta = 150°$ and $\theta = 170°$ coincides in Fig.4.9, while the contact time obtained with $\theta = 120°$ are slightly higher, whereas shares a similar scaling tendency.

At the end of this chapter, an analysis of the energy at bouncing-off instant is given to illustrate the physics in the retraction stage. The major part of the surface energy stored E_{max}^S is dissipated by the viscous forces and the remaining is converted into kinetic energy.

Chapter 5

Energetic Analysis of Droplets' Dynamics on Solid Surface

Upon impact, the droplet begins to spread on the solid surface and the kinetic energy of the droplet is converted into surface energy. At the same time, fluid viscosity comes into play, particularly near the solid surface, where we assume a no-slip boundary condition. As the droplet spreads, it deforms into a thin film, whose thickness is limited by the growth of a viscous boundary layer near the solid wall. Owing to the surface tension, the edge of the film retracts relative to the flow in the film and fluid collects into a toroidal rim bounding the film. The energy balance of a droplet impacting on a solid surface takes into account the kinetic energy E^K, surface energy E^S, gravitational potential energy E^G and energy loss W due to viscous dissipation. Spreading is driven by the kinetic energy E^K and countered by the surface energy E^S and viscous dissipation W. The Weber number We describing the ratio between the kinetic energy and capillary energy, and the Reynolds number Re describing the ratio between the kinetic energy and viscous dissipation describe the initial energy of droplet. From an energy conservation standpoint, the energy of droplet prior to impact should equal to the energy of the splat and the dissipation work done to countering spreading. Then the energy conservation law prior to and after impact reads

$$E_0^S + E_0^K + E_0^G = E^S(t) + E^K(t) + E^G(t) + W(t), \tag{5.1}$$

where the subscript '0' indicates the initial state of droplet. And for these cases where the droplet is of micro-meter size, the difference of the gravitational potential energy of the droplet

before and after impaction $E^G - E_0^G$ could be neglected. Then the Eq.(5.1) could be written as

$$E_0^S + E_0^K = E^S(t) + E^K(t) + W(t). \tag{5.2}$$

Before impact, the total initial energy of the spherical droplet, consisting of the initial kinetic energy E_0^K and surface energy E_0^S, is given by

$$E_0 = E_0^S + E_0^K, \tag{5.3}$$

where

$$E_0^K = \left(\frac{1}{2}\rho V_0^2\right)\left(\frac{4\pi}{3}R_0^3\right), \tag{5.4}$$

and

$$E_0^S = \pi D_0^2 \sigma. \tag{5.5}$$

The calculations of energy of the droplet and the dissipation work (the right part of Eq.(5.2)) are the key issues to conduct an accurate analysis on the droplet's energy. The estimation of surface energy of the splat E^S is significantly dependent on the shape of the splat. The estimation of dissipation work W depends largely on the volume and the time where the dissipation occurs. We also assume that the droplet volume is constant.

A large number of studies deal with the prediction of maximum spreading on solid surface [116, 46], and a recent review for semi-empirical and energy balance models can be found in the work of Roisman *et al.* [84], Roisman [85] and Attane *et al.* [3]. In theoretical approaches, maximum spreading is commonly predicted based on the energy balance, in terms of kinetic energy and surface energy before impact and surface energy, viscous dissipation at its maximum spreading. Ukiwe and Kwok [99] investigated some of the models for estimating ξ_{max} and modified the model of Pasandideh-Fard *et al.* [72] with their experimental results.

In all these analytical or semi-analytical approaches, the total kinetic energy of the droplet at maximum spreading state is assumed to be zero. Among them, the cylinder model and ring-disk model are the most extensively used [see e.g., 72, 48, 32]. Clanet *et al.* [17] found that internal kinetic energy still exists when the droplet reaches its maximal extension with internal flux. In our simulations, the kinetic energy of the droplet at the maximum spreading extent does not reach zero exactly, but is negligible compared to the surface tension energy at the moment. This assumption simplifies the calculation of the energy balance at the maximum spreading extent. Good prediction was obtained by assuming zero internal kinetic energy [9]. The viscous

dissipation that being dissipated from the initial state to the maximum state also needs to be considered. Potential energy due to gravity is neglected in this work, as its effect is usually insignificant for momentum-driven droplet impact.

In this chapter, an energy analysis will be given in **Section 5.1**. This section will firstly present the overall time-evolving energy components during the spreading and retraction process. Then, the analysis on energy balance would be conducted in spreading and retraction phase, separately. The influences of liquid properties and impact condition on the transformation among three energy components will be investigated at the maximum spreading state. An analysis on the energy balance at the bouncing-off instant is provided for the first time to present more details on the droplets' bouncing-off mechanism. **Section 5.2** will focus on several theoretical models predicting the maximum spreading diameter based on the energy conservation equation. Then, an improved model would be proposed with the correlation Eq.(3.17) between ξ_{max} and t^*_{max} obtain in Chapter 4. A comparison of maximum spreading diameter between experiments, predictions of the original and the modified model will also be included. A summary of this chapter will be given in **Section 5.3**.

5.1 Energetic Analysis Based on Numerical Simulation Results

At the begining of this section, we present a comparison of the kinetic energy and the dissipation function between our simulation results and the simulations by Lee *et al.* [55]. The contact angle adopted in simulation is set as the equilibrium contact angle $\theta = 61°$, whereas Lee *et al.* [55] utilised the dynamic contact angle model by Kistler [49], in which the dynamic contact angle is calculated for each time step. Our simulation provides good prediction of the geometrical shapes of the liquid/gas interface at $t = 0.5\ ms$ and $1.0\ ms$, whereas at $t = 2.0\ ms$ and $2.6\ ms$, the droplet spreads larger in our simulation. This difference is caused by the different contact angle, the contact angle at $t = 2.0\ ms$ and $2.6\ ms$ are around $105°$. The droplet would spread larger with $\theta = 61°$ in our simulation. However, our simulation captures the dissipation occurring at the contact line better than the model by Lee *et al.* [55].

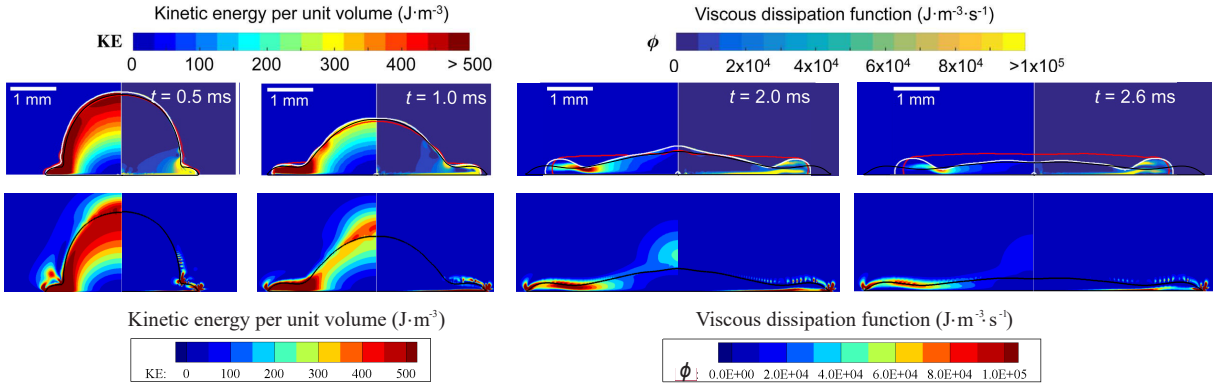

FIGURE **5.1**: Time evolution of water droplet impacting on a steel surface at $V_0 = 1.1\ m/s$. The upper row is adopted from the work by Lee *et al.* [55]. The second row is the results of numerical simulation. The red line presents the liquid/gas interfaces from experiments, measured by shadowgraphy and the the black line presents the interfaces from numerical simulations. The left contour map shows the kinetic energy per unit volume, and the right presents the dissipation function ϕ.

5.1.1 The energy evolution during dynamics

The spreading dynamics and outcomes after droplets' impaction are the results of the transformations among the kinetic energy, surface energy and viscous dissipation within the droplet. During spreading stage, the kinetic energy drives the spreading, and simultaneously is being countered by the surface energy and dissipation work, i.e., the kinetic energy decreases, the surface energy and viscous dissipation work increase in spreading. Studies distinguish two main regimes in spreading, the capillary regime and the viscous regime [see, e.g., 17, 26]. In capillary regime, the viscous dissipation could be neglected, the spreading factor is determined by the balance between kinetic and surface energy. In viscous regime, the viscous dissipation plays the dominating role in countering the spreading. In Fig.5.2, the time-evolving conversions among three energy terms $E^K(t)$, $E^S(t)$ and $W(t)$ are presented, firstly the overall energy balance from impact to rebound, then the energy balance in spreading and the energy balance in retraction. The column (a) and (b) shows a ceramic droplet ($\sigma = 0.5\ N/m$, $\mu = 0.09\ Pa \cdot s$) impacting at low velocity $V_0 = 3\ m/s$, and at high velocity $V_0 = 20\ m/s$, respectively. And the maximum spreading (t^*_{max}) and bouncing off (t^*_c) time are marked by the dash lines. Before droplet impact (referred to using subscript 0), the kinetic energy E^K_0 and surface energy E^S_0

constitute the total energy in the droplet. In Fig.5.2 (a-1) and (b-1), the evolving percent of energy terms to inital energy E_0 is plotted. In (a-1), the surface energy $E^S(t)$ takes 80% of the initial energy in the whole process after impact, while the dissipation occupies 80% of the initial energy in (b-1).

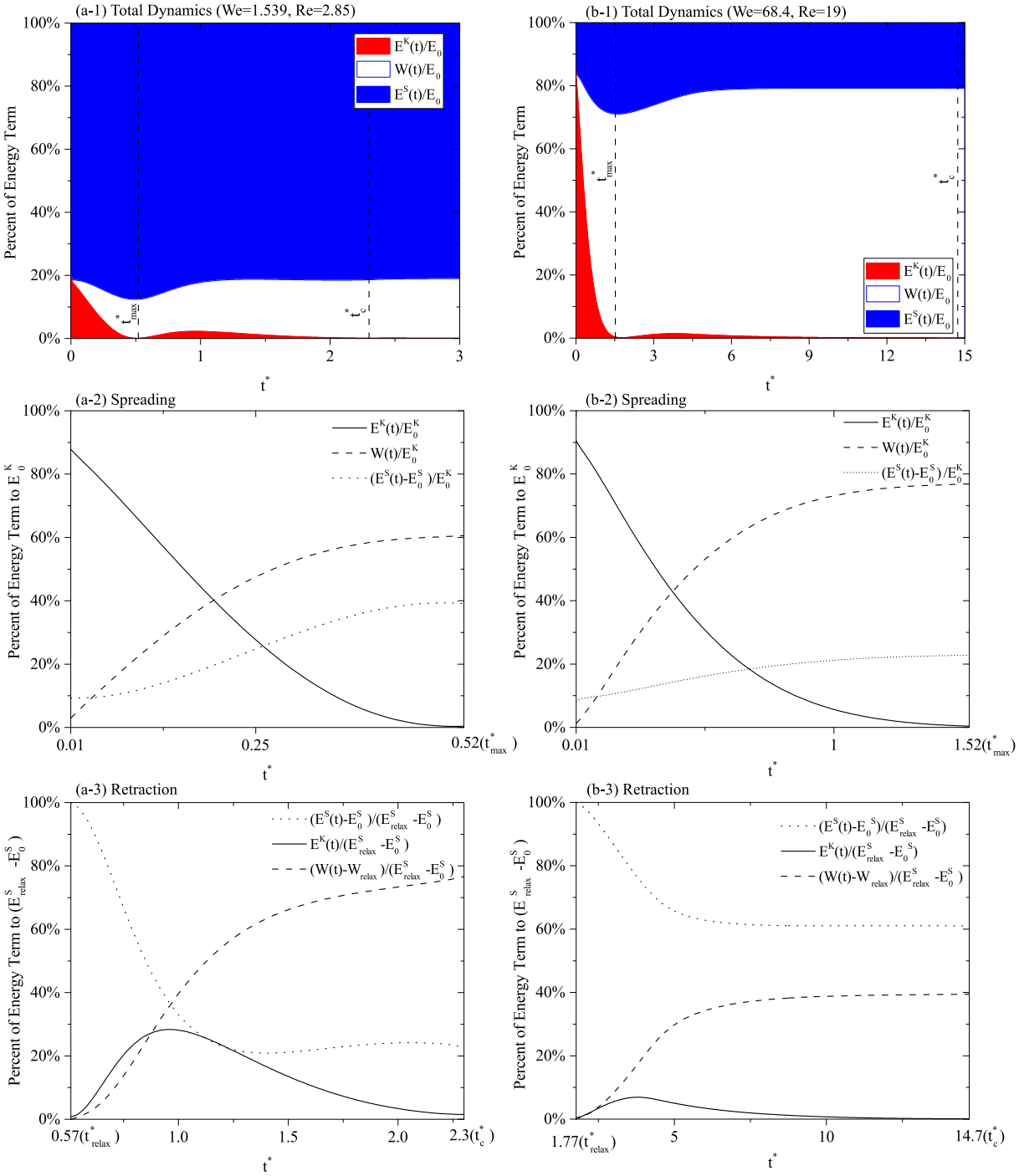

FIGURE **5.2**: Time-evolving energy components's percent at low impact velocity on a hydrophobic surface ($\theta = 170°$). The two columns: (a) $V_0 = 3\ m/s$, $We = 1.539$, $Re = 2.85$, (b) $V_0 = 20\ m/s$, $We = 68.4$, $Re = 19$.

After impact ($t^* = 0$), the kinetic energy $E^K(t)$ decreases with time and is converted to surface energy $E^S(t)$ and viscous dissipation $W(t)$ until the droplet reaches its maximum spreading state. During spreading, the surface energy $E^S(t)$ increases with time due to the increase of

surface area and the cumulative viscous dissipation work W increases simultaneously.

In spreading stage (Fig.5.2 (a-2) and (b-2)), the percent of energy terms to E_0^K are plotted, as the inertial forces drive the droplet to spread. At the very early time, the percent $(E^S(t) - E_0^S)/E_0^K$ is higher than the percent of dissipation work $W(t)/E_0^K$, as the droplet deforms largely in the short time after impaction. As the accumulating rate of dissipation work is faster than the transforming rate of surface energy, the dissipation occupies higher portion than surface energy in the later spreading stage.

At maximum spreading, the remaining kinetic energy E_{max}^K in the droplet is less than 2% to the initial energy. A phenomenon should be highlighted is that the kinetic energy $E^K(t)$ does not reach its bottom at maximum spreading due to some flows inside the droplet. The droplet reaches its maximum spreading slightly earlier than its kinetic droplet reaches its bottom. The time that the kinetic energy $E^K(t)$ decreases to its bottom is defined as the relaxing time, t_{relax} with dimensionless expression $t_{relax}^* = t_{relax}/(D_0/V_0)$. The phase between t_{max} and t_{relax} is called the relaxing phase.

The retraction phase starts after the relaxing phase. The retraction dynamics is motored by the surface energy stored in the droplet at maximum spreading. In order to illustrate the retraction stage clearly, the percent of variations of energy terms $E^S(t) - E_0^S$, $E^K(t)$ and $W(t) - W_{relax}$ since the end of relaxing phase to $E_{relax}^S - E_0^S$ are given in (Fig.5.2 (a-3) and (b-3)). We first notice that the kinetic energy $E^K(t)$ will regain some energy from surface energy to reach a small summit at first before being dissipated. We also could tell that these two retraction stages (a-3) and (b-3) are both in the capillary-viscous regime as the influences of viscous forces could not be neglected. In the later retraction phase, the kinetic energy starts to decrease and the variation of surface energy is small and slow. We also observe that the dissipation work is mainly done in the spreading stage (see Fig.5.3). The dissipation work done in spreading equals W_{max} and the total dissipation work accumulated in the whole contact time equals W_{BC}, the ratio W_{max}/W_{BC} is plotted versus an exponential function as $WeRe^{-3/4}$.

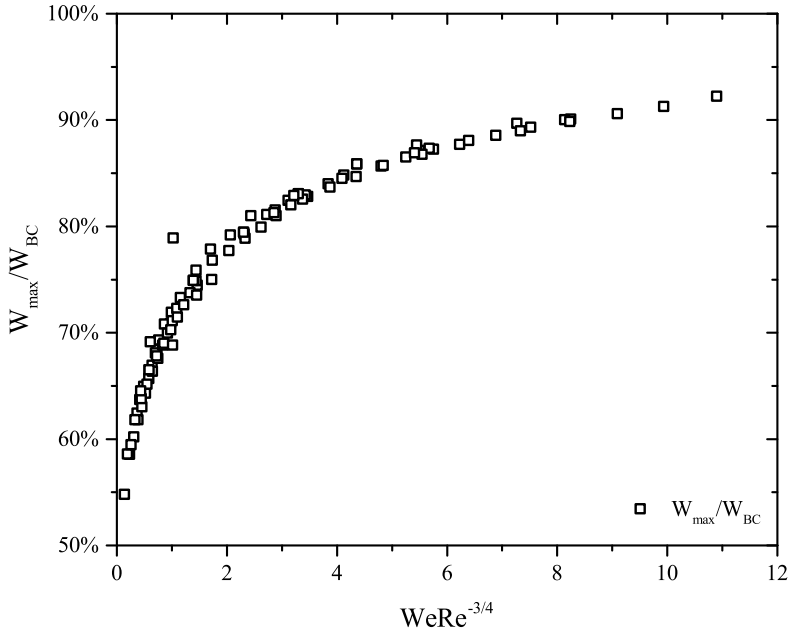

FIGURE **5.3**: The ratio between the dissipation in spreading and the total dissipation W_{max}/W_{BC} plotted versus $WeRe^{-3/4}$.

From Fig.5.2 (a-1) and (b-1), we also could tell that at low impact velocity, the droplets' shapes are spheroidal at t_c as the surface energy at bouncing-off instant is nearly the same as the initial surface energy, and at high impact velocity, the droplets will not maintain spheroidal shapes as the difference between E^S_{BC} and E^S_0 becomes larger than the one at low impact velocity.

5.1.2 Energy Balance at The Maximum Spreading State

After investigating the time-evolving transformation among three energy components, we continue to conduct an analysis on the influences of liquid properties on the portion of energy components at maximum spreading state. The percent of kinetic energy, surface energy and dissipation work of impacting droplet to initial energy E_0 at maximum spreading state are presented in Fig.5.4. At maximum spreading, the percent of remaining kinetic energy of the droplets at maximum spreading state is around 2% of the initial energy of the droplet ($E_0 = E^K_0 + E^S_0$). Based on this result, we regard that the kinetic energy of droplet vanishes at the maximum spreading state. For lower impact velocities ($V_0 = 3, 4, 5m/s$), surface energy occupies a major part (around 80%) of the total energy of the droplet, the growing dissipation work gains a

minor portion of the total energy. For higher impact velocities, the dissipation work increases as the increase of the spreading diameter. The influences of dynamics viscosity become larger at higher impact velocities.

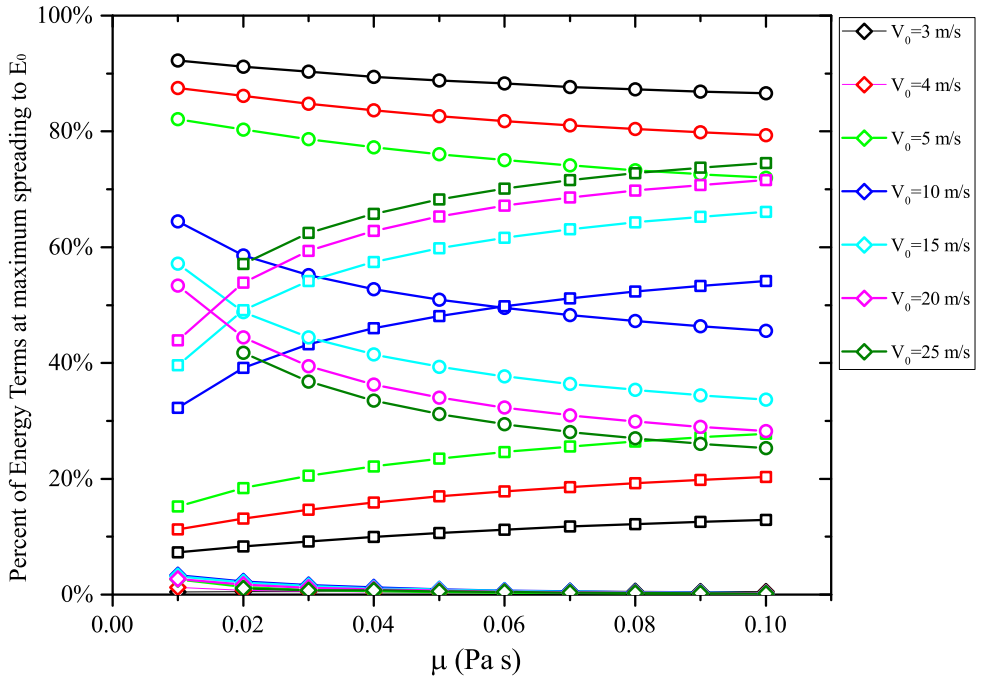

FIGURE **5.4**: Energy components's portion at maximum spreading state when droplets impact on a hydrophobic surface ($\theta = 170°$). The diamond ($\diamond$), circle ($\circ$) and square ($\square$) represent the ratio of E^K_{max}/E_0, E^S_{max}/E_0 and W_{max}/E_0, respectively. The colours indicate different impact velocities of the impacting droplets.

It is worth knowing the conversion among the three energy components during the spreading stage. The transport among three energy terms during spreading phase are defined as,

$$\Delta E^K_{max} = E^K_{max} - E^K_0, \quad \Delta E^S_{max} = E^S_{max} - E^S_0, \quad \Delta W_{max} = W_{max}, \tag{5.6}$$

to describe the exchange qualitatively. During the spreading stage, the initial kinetic energy E^K_0 turns into the augmentations in surface energy ΔE^S and dissipation work ΔW. In Fig.5.5, the ratios of $\Delta E^S_{max}/\Delta E^K_{max}$ and $\Delta W_{max}/\Delta E^K_{max}$ are presented with a systematic variation of dynamic viscosity for impacting droplets with different impact velocities. It is observed that the ratio ΔW_{max} increases with the increase of dynamic viscosity μ.

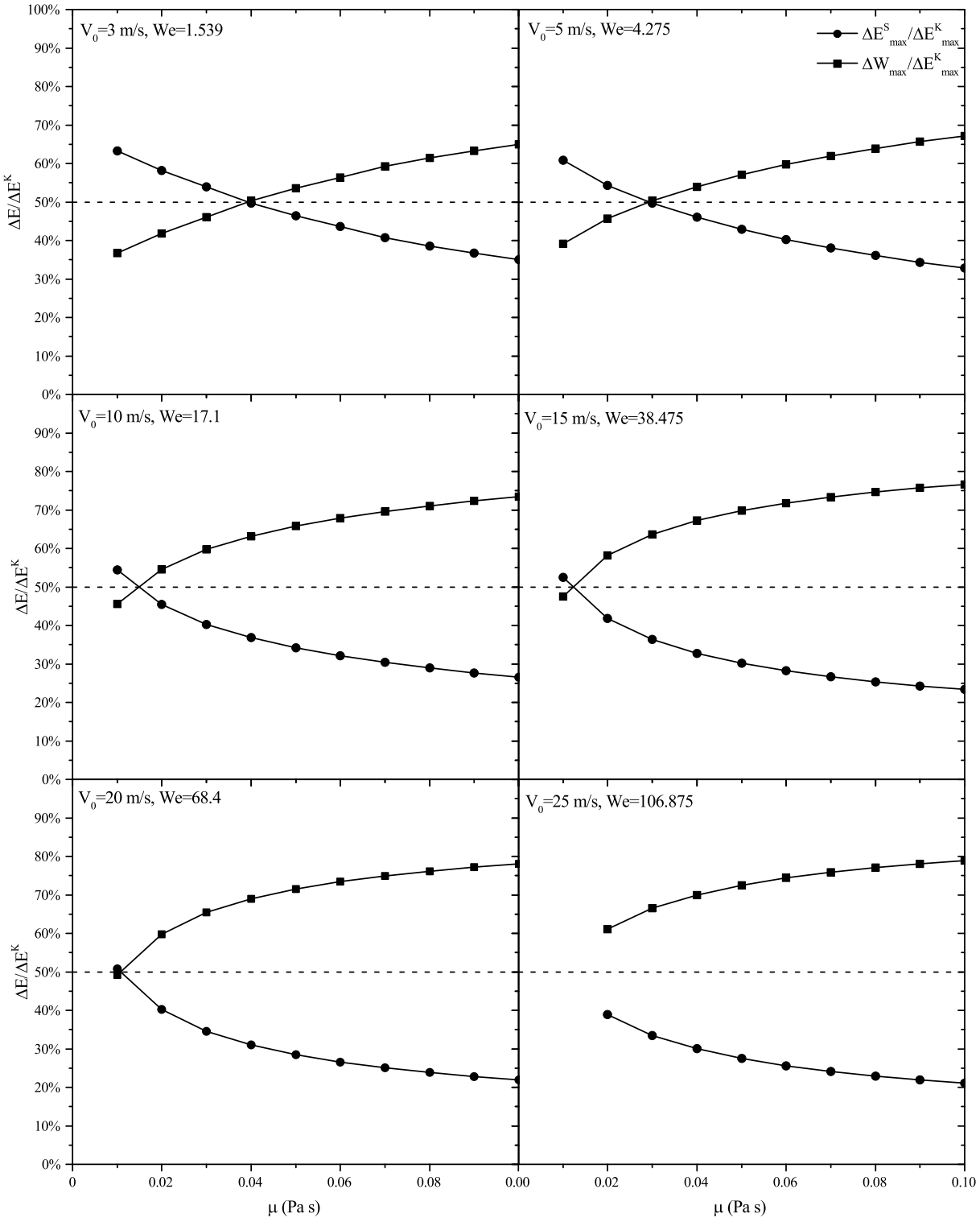

FIGURE **5.5**: Energy components's variations at maximum spreading state when droplets impact on a hydrophobic surface ($\theta = 170°$).

5.1.3 Energy Balance at The Bouncing-Off Instant

As mentioned in chapter 5, the retractions in the works by Richard *et al.* [80] and Okumura *et al.* [71] are in the capillary-inertial regime with high restitution coefficient $\epsilon \to 1$ where the droplet hardly spreads, our simulations are set up to put droplets' retraction dynamics in the capillary-viscous regime, where the droplet spreads till maximum spreading extent then recoil to rebound off from the surface. Recall the definition of restitution coefficient $\epsilon = E^K_{BC}/E^K_0$ given previously. The restitution coefficient ϵ in this work is smaller than 0.4, as shown in Fig.5.6.

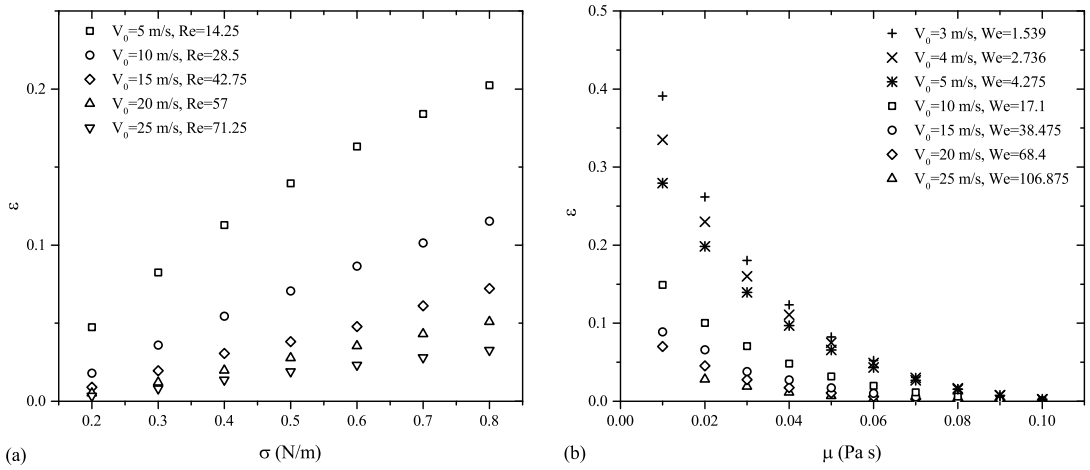

FIGURE **5.6**: The restitution coefficient ϵ plotted versus surface tension σ (a) and viscosity μ (b).

In the capillary-viscous regime, the restitution coefficient ϵ increases linearly with the surface tension (Fig.5.6 (a)), and decreases when increasing the viscosity (Fig.5.6 (b)). We also highlight that the restitution coefficient ϵ becomes larger with smaller impact velocity V_0 in this regime where the spreading is influential.

Recall the important assumption made that the droplet's kinetic energy E^K_{max} vanishes at maximum spreading state. In the spreading stage, compared to the surface energy E^S_{max} and the energy W_{max} having been dissipated, the droplet's kinetic energy E^K_{max} could be regarded as zero, this assumption is validated by numerical simulations and experiments. While this assumption could no longer be delivered in the retraction stage, as the major part of initial energy

is dissipated during the spreading stage. And the kinetic energy E^K_{max} at maximum spreading and E^K_{relax} is in the same order as the kinetic energy E^K_{BC} at bouncing-off instant.
The energy variations between the bouncing-off instant and the end of relaxing phase are defined as

$$\Delta E^K_{BC} = E^K_{BC} - E^K_{relax}, \tag{5.7}$$

$$\Delta E^S_{BC} = -(E^S_{BC} - E^S_{relax}), \tag{5.8}$$

$$\Delta W_{BC} = W_{BC} - W_{relax}, \tag{5.9}$$

where the subscript $'BC'$ indicates the droplet's bouncing-off instant and $'relax'$ for the end in relaxing phase. Note that the surface energy stored inside at the end of relaxing phase is the motor behind the recoil dynamics.
In Fig.5.7, the variations of kinetic energy ΔE^K_{BC}, surface energy ΔE^S_{BC}, and dissipation work ΔW_{BC} between two state: the maximum spreading state and the bouncing-off state are presented. In the four cases shown in Fig.5.7, the variations ΔE^S_{BC} and ΔE^K_{BC} decrease as the dynamic viscosity μ increases from $0.01\ Pa \cdot s$ to $0.1\ Pa \cdot s$. Concerning the difference of kinetic energy ΔE^K_{BC} between two states, ΔE^K_{BC} would become negative ($E^K_{BC} - E^K_{max} < 0$) when the dynamic viscosity is near $0.1\ Pa \cdot s$. In the cases $We < 5$ (subfigure (a) and (b)) the variation of dissipation work ΔW_{BC} does not change when varying the dynamic viscosity μ, the variations of surface energy ΔE^S_{BC} is mostly reflected by the variations in kinetic energy ΔE^K_{BC}. while the variation of kinetic energy with viscosity is apparent when the Weber number is larger ($We = 38.475, 106.875$, (c) and (d)).

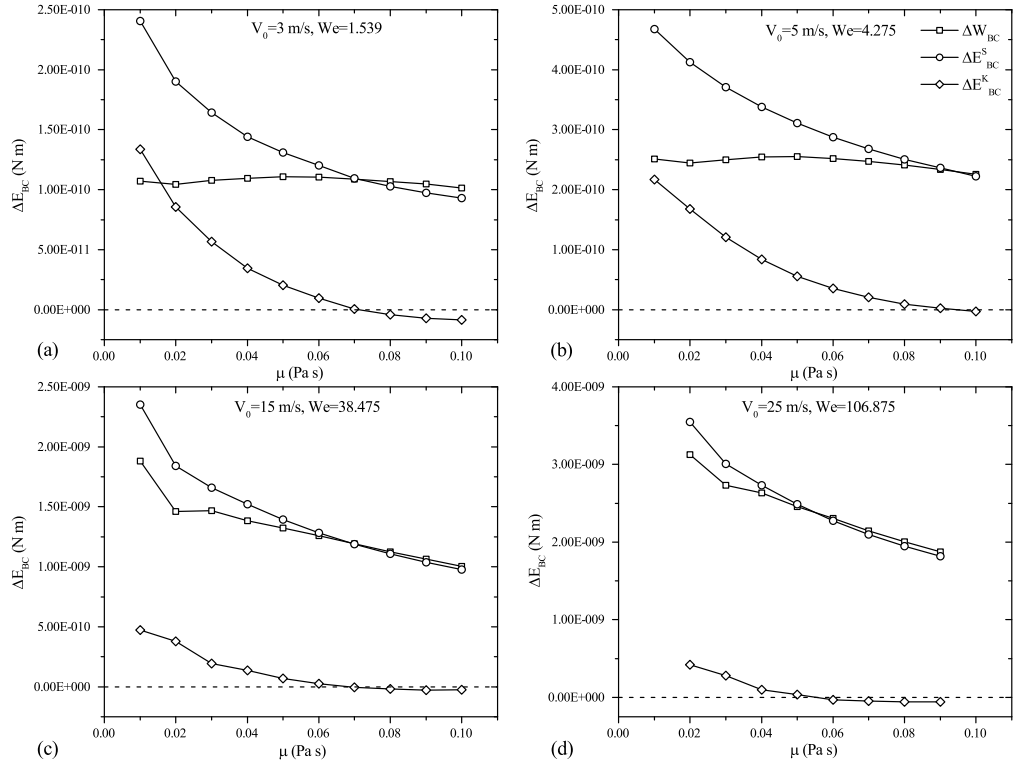

FIGURE **5.7**: The energy components' variations ΔE^K_{BC}, ΔE^S_{BC}, ΔW_{BC}, between droplets' bouncing-off instant and the end of relaxing phase on superhydrophobic surfaces. (a) $V_0 = 3\ m/s$, $We = 1.539$, (b) $V_0 = 5\ m/s$, $We = 4.275$, (c) $V_0 = 15\ m/s$, $We = 38.475$, (d) $V_0 = 25\ m/s$, $We = 106.875$.

Further, the ratios $\Delta W_{BC}/\Delta E^S_{BC}$ and $\Delta E^K_{BC}/\Delta E^S_{BC}$ are plotted in Fig.5.8. In subfigure (a) ($We = 1.539, 2,736, 4.275$), the ratio $\Delta W_{BC}/\Delta E^S_{BC}$ increases from around 50% to 100%, the ratio $\Delta E^K_{BC}/\Delta E^S_{BC}$ declines from 50% to approximate 0. The negative values of ratio $\Delta E^K_{BC}/\Delta E^S_{BC}$ mean that the kinetic energy E^K_{max} is smaller than E^K_{BC}. Only in the cases $We = 1.539$, $Re = 85.5$ and $We = 2.736$, $Re = 85.5$, the ratio $\Delta E^K_{BC}/\Delta E^S_{BC}$ is higher than $\Delta W_{BC}/\Delta E^S_{BC}$. In subfigure (b) with higher Weber number ($We = 38.475, 68.4, 106.875$), it's clear that the surface energy E^S_{max} stored in the droplet at maximum spreading state are mostly dissipated by the viscous forces. And the influence of viscosity on the energy transform in retraction stage at low impact velocity is larger than at high velocity.

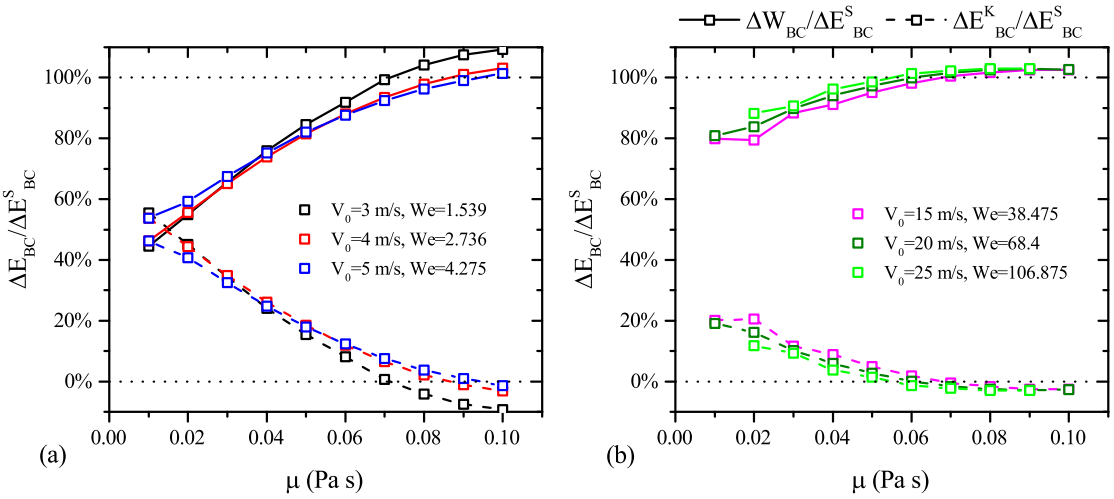

FIGURE **5.8**: The energy components' percent $\Delta W_{BC}/\Delta E^S_{BC}$, $\Delta E^K_{BC}/\Delta E^S_{BC}$ between droplets' bouncing-off instant and maximum spreading state on purely non-wetting surfaces. (a) Lower velocity, $V_0 = 3,\ 4,\ 5\ m/s$, (b) Higher velocity, $V_0 = 15,\ 20,\ 25\ m/s$.

The variations of the ratio $\Delta W_{BC}/\Delta E^S_{BC}$ and $\Delta E^K_{BC}/\Delta E^S_{BC}$ with surface tension σ are presented in Fig.5.9. With higher surface tension σ, the more portion of E^S_{max} is converted into the kinetic energy E^K_{BC} and less energy is dissipated by the viscous forces.

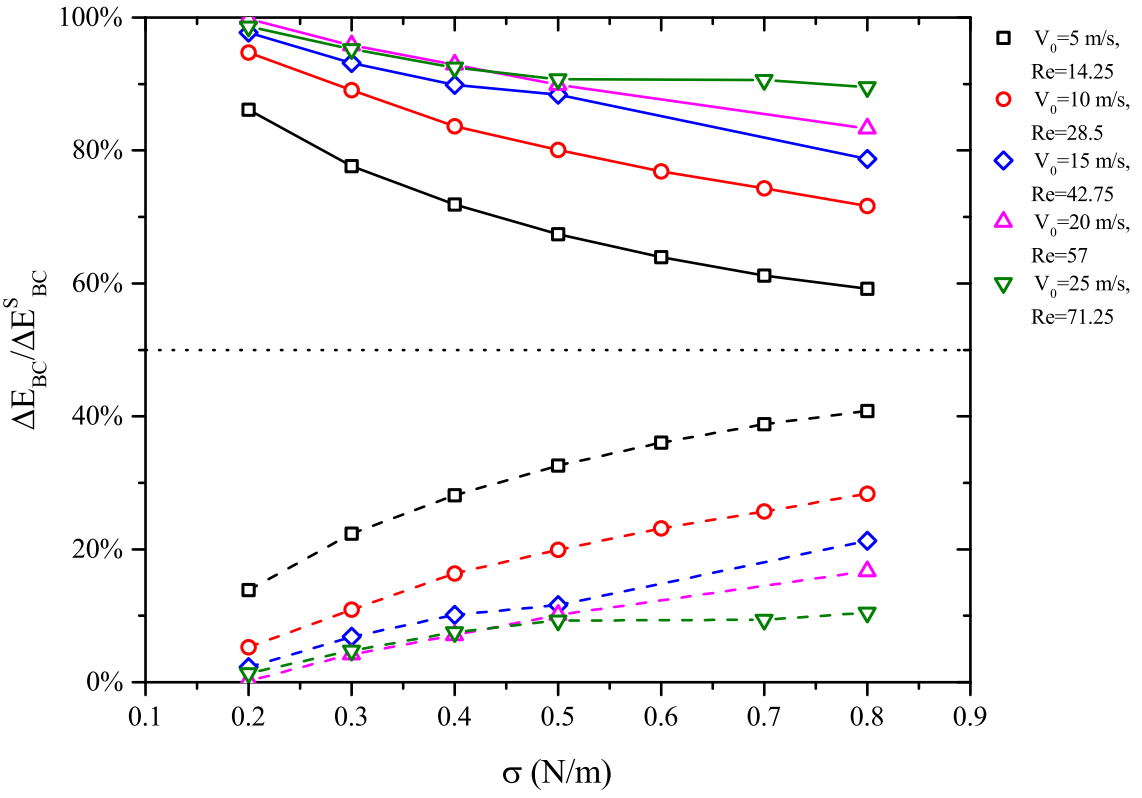

FIGURE **5.9**: The energy components' percent $\Delta W_{BC}/\Delta E^S_{BC}$ (symbol with solid line), $\Delta E^K_{BC}/\Delta E^S_{BC}$ (symbol with dash line) between droplets' bouncing-off instant and maximum spreading state on purely non-wetting surfaces.

5.2 Brief review of several theoretical cylinder models on predicting droplets' maximum spreading

As shown in Fig.4.1 and Fig.4.2 in chapter 4, the liquid/gas interfaces of droplets at maximum spreading stage could be approximated as a cylinder in our simulations. To keep the consistency of this thesis, several theoretical prediction models [16, 72, 99, 56] based on cylinder assumption will be reviewed in this section .

When the energy conservation law Eq.(5.2) is used to calculate the maximum spreading diameter, it takes the form,

$$E^S_0 + E^K_0 = E^S_{max} + E^K_{max} + W_{max}, \tag{5.10}$$

where the superscript 'max' represents the droplet's maximum spreading state. Publications concerning theoretical prediction of maximum spreading diameter generally make the key assumption that the kinetic energy of the droplet at maximum spreading state E^K_{max} vanishes. The kinetic energy E^K_{max} is not rigorously, but could be seen as zero due to the existence of flows inside the droplet (shown in Fig.5.2 (a-1), (b-1)). Eliminating the term E^K_{max} from Eq.(5.10) leads to

$$E^S_0 + E^K_0 = E^S_{max} + W_{max}. \tag{5.11}$$

Different models based on Eq.(5.11) have been proposed, which differ in the choice of terms included in this energy balance, as well as the geometry of the droplet during spreading and the specific descriptions of the terms E^S_{max} and W. In this section, we first list and compare the analytical models predicting the maximum spreading diameter with the cylinder assumption existing in the literature, then propose a new analytical model for the estimation of maximum spreading diameter.

5.2.1 The model of Chandra and Avedisian [16]

Chandra and Avedisian [16] proposed an estimation for the maximum spreading diameter from this energy conservation for the case with no bubbles entrapped inside the droplet. The droplet shape at maximum spreading state is modelled as a disc where the curved edge of the boundary of the splat is neglected. The disc is in contact with two interfaces: the liquid/gas and the liquid/solid interfaces. The surface energy of the liquid/gas interface (top interface) is calculated as,

$$E^S_{LG} = \pi\sigma D^2_{max}/4, \tag{5.12}$$

where σ the surface tension of liquid/gas interface. The surface energy of the liquid/solid interface (bottom interface) is

$$E^S_{SL} = \pi D^2_{max}(\sigma_{SL} - \sigma_{SG})/4, \tag{5.13}$$

in which σ_{SL} and σ_{SG} are the surface tension of liquid/solid and solid/gas interface. Then, the surface energy $E^S_{max} = E^S_{SL} + E^S_{LG}$ takes the expression,

$$E^S_{max} = \frac{\pi}{4}\sigma D^2_{max}(1 - cos\theta), \tag{5.14}$$

with the use of Young's equation Eq.(1.1) [118].

Chandra and Avedisian [16] approximated the work done against viscosity in deforming the droplet as

$$W_{max} = \int_0^{t_{max}} \int_\Omega \phi \mathrm{d}V \mathrm{d}t \approx \phi \Omega t_{max}, \tag{5.15}$$

where ϕ is the dissipation function, Ω is the volume where the dissipation work takes place and t_{max} is the maximum spreading time. They assume that the dissipation occurs inside the droplet, the Ω equals to $\pi D_{max}^2 h/4$ and,

$$t_{max} = D_0/V_0, \tag{5.16}$$

which is the time for a droplet height to vanish from its maximum value D_0. The dissipation function ϕ is given by

$$\phi = \mu \frac{\partial V_i}{\partial x_j}\Big(\frac{\partial V_i}{\partial x_j} + \frac{\partial V_j}{\partial x_i}\Big) \approx \mu \Big(\frac{V_0}{h}\Big)^2. \tag{5.17}$$

Taking the expressions of ϕ, Ω and t_{max} into Eq.(5.15) yields

$$W_{max} \approx \frac{\pi \mu D_0 D_{max}^2 V_0}{4h}. \tag{5.18}$$

Substituting the initial terms Eq.(5.4), Eq.(5.5) and terms Eq.(5.14), Eq.(5.18) at maximum spreading state into Eq.(5.11) gives

$$\frac{3We}{2Re}\xi_{max}^4 + (1 - cos\theta)\xi_{max}^2 - \Big(\frac{We}{3} + 4\Big) \approx 0. \tag{5.19}$$

They assumed that the characteristic length scale in the impact direction was of the order of the splat thickness at the maximum spread, i.e., the dissipation occurred in the whole droplet. This model over-predicted the maximum spreading factor compared to the experimental results by up to 40%.

5.2.2 The model of Pasandideh-Fard *et al.* [72]

Like the work of Chandra and Avedisian [16] and many other models, Pasandideh-Fard *et al.* [72] assumed the shape of maximum spreading splat to be cylindrical. The difference lies in the estimation of dissipation work. The first modification made to the model of Chandra and Avedisian [16] is in the assumption of t_{max}. They assumed that the droplet flows from a truncated-sphere into a cylinder and utilized the mass conservation law to determine the contact line velocity. The maximum spreading time t_{max} was calculated as

$$t_{max} = \frac{8D_0}{3V_0}. \tag{5.20}$$

Many works, concerning the maximum spreading factor from energy balance perspective, use this form of t_{max} to calculate the viscous dissipation [see e.g., 32, 48, 99].

The second modification is in the calculation of the volume where the dissipation takes place. They proposed that most of the viscous dissipation took place in the boundary layer at liquid/solid interface. The viscous dissipation function becomes

$$\phi \approx \mu \left(\frac{V_0}{\delta} \right)^2, \tag{5.21}$$

where δ is the boundary layer thickness,

$$\delta = (cD_\mu \cdot t_{max})^{1/2} = \frac{2D_0}{\sqrt{Re}}, \tag{5.22}$$

where $c = 2/3$, D_μ is the transverse momentum diffusion constant and equals μ/ρ. Then the dissipation work W is obtained as

$$W_{max} = \frac{\pi}{3\sqrt{Re}} \rho V_0^2 D_0 D_{max}^2. \tag{5.23}$$

Substituting this expression Eq.(5.23) of dissipation work and Eq.(5.14) into the energy conservation law Eq.(5.11), the maximum spreading factor ξ_{max} is obtained as

$$\xi_{max} = \sqrt{\frac{We + 12}{3(1 - cos\theta) + 4We/\sqrt{Re}}}. \tag{5.24}$$

With these two modifications, Pasandideh-Fard *et al.* [72] still overpredicted ξ_{max} by 15%. The error is mainly caused by the calculation of t_{max}, which usually is larger than the actual one measured in experiments.

5.2.3 The model of Ukiwe and Kwok [99]

Compared to the models proposed by Chandra and Avedisian [16] and Pasandideh-Fard *et al.* [72], a modification to the estimation of surface energy is made by considering the surface energy of the lateral liquid/gas interface of the disk. The new surface energy E_{max}^S has the expression as

$$E_{max}^S = \pi\sigma D_{max} h + \frac{\pi}{4}\sigma D_{max}^2 (1 - cos\theta), \tag{5.25}$$

where $h = (2D_0^3)/(3D_{max}^2)$ is the height of the disk due to the volume conservation. With this modified term E_S and the viscous term of Pasandideh-Fard *et al.* [72], Ukiwe and Kwok [99]

derived the maximum spreading factor as

$$(We + 12)\xi_{max} = 8 + \xi_{max}^3 \left[3(1 - cos\theta) + 4\frac{We}{\sqrt{Re}}\right]. \tag{5.26}$$

The major difference between Eq.(5.26) and Eq.(5.24) obtained by Pasandideh-Fard *et al.* [72] lies in the estimation of surface energy at the maximum spread.

5.2.4 The model of Lee *et al.* [56]

The previous models [16, 72, 99] used the equilibrium Young contact angle in calculating the surface energy E_{max}^S, which contributes considerate deviations of the predictions from the measured ξ_{max}. The recent model predicting the maximum spreading factor by Lee *et al.* [56] used the contact angle $\theta_D(t_{max})$ experimentally measured experimentally in replace of the Young contact angle. Further, in their experiments, they also found that the spreading time is dependent on the liquids' surface tension, and proposed that $t_{max} = bD_{max}/V_0$, where b is the ratio of surface tension of liquid to water. So the prediction takes the expression as

$$\rho D_0 V_0^2 + 12\sigma = 3\sigma(1 - cos\theta_D(t_{max}))\xi_{max}^2 + \frac{8\sigma}{\xi_{max}} + 3\left(\frac{b}{2}\right)^{1/2} \rho D_0 V_0^2 \xi_{max}^{5/2} Re^{-1/2}. \tag{5.27}$$

5.2.5 Refinement of the Models

Based on the model by Ukiwe and Kwok [99], we introduced the correlation Eq.(3.17) between ξ_{max} and t_{max} obtained in Chapter 4 to the calculation of dissipation work Eq.(5.21), the boundary layer thickness equals

$$\delta = (cD_\mu \cdot t_{max})^{1/2} = \sqrt{\frac{D_{max}D_0}{Re} \cdot \left(\frac{We}{2}\right)^{0.1}}, \tag{5.28}$$

in which the constant c equals 2 for one-dimensional problem. Then the dissipation work W expresses as

$$W_{max} = \frac{\pi\mu}{8} D_{max}^3 V_0 \left(\frac{Re}{D_{max}D_0}\right)^{1/2} \left(\frac{We}{2}\right)^{0.05}. \tag{5.29}$$

With other energy terms used in the model of Ukiwe and Kwok [99], the energy balance Eq.(5.11) for the maximum spreading factor is solved as follows,

$$\frac{We}{12} + 1 = \frac{2}{3}\frac{1}{\xi_{max}} + \frac{1 - cos\theta}{4}\xi_{max} + \frac{1}{8}\frac{We}{\sqrt{Re}}\xi_{max}^{5/2}\left(\frac{We}{2}\right)^{0.05}. \tag{5.30}$$

This model is referred as the current model and can be solved numerically to provide prediction of ξ_{max}. In Fig.5.10, we compare the predictions of Chandra and Avedisian [16], Pasandideh-Fard *et al.* [72], Ukiwe and Kwok [99] and Lee *et al.* [56]. We find that all the models provide good predictions at high impact velocity. The models of Chandra and Avedisian [16], Pasandideh-Fard *et al.* [72] and Ukiwe and Kwok [99] over-predict the maximum spreading factor when the impact velocity is smaller than $1\ m/s$. The recent model by Lee *et al.* [56] and current model fit well with the experiments at low and high velocity. For the discrimination between different models, only the model of Pasandideh-Fard *et al.* [72] using $\theta_D(t_{max})$ as the Young contact angle is given to present the influence of Young contact angle. Replacing the Young contact angle θ with $\theta_D(t_{max})$ has a significant impact on the prediction of maximum spreading factor in the range of low impact velocity. With this comparison, using $\theta_D(t_{max})$ seems rational, as it is the actual contact angle between the droplet and the surface at maximum spreading. However, the solid-liquid and solid-gas interfacial tension σ_{SL}, σ_{SG} can only be expressed in terms of liquid-gas interfacial tension σ and θ. In some cases, the dynamic contact angle $\theta_D(t_{max})$ at maximum spreading can be close to the Young contact angle θ, as shown in Fig.5.10 (d). Nevertheless, the measured dynamic contact angle $\theta_D(t_{max})$ could provide better prediction of ξ_{max}.

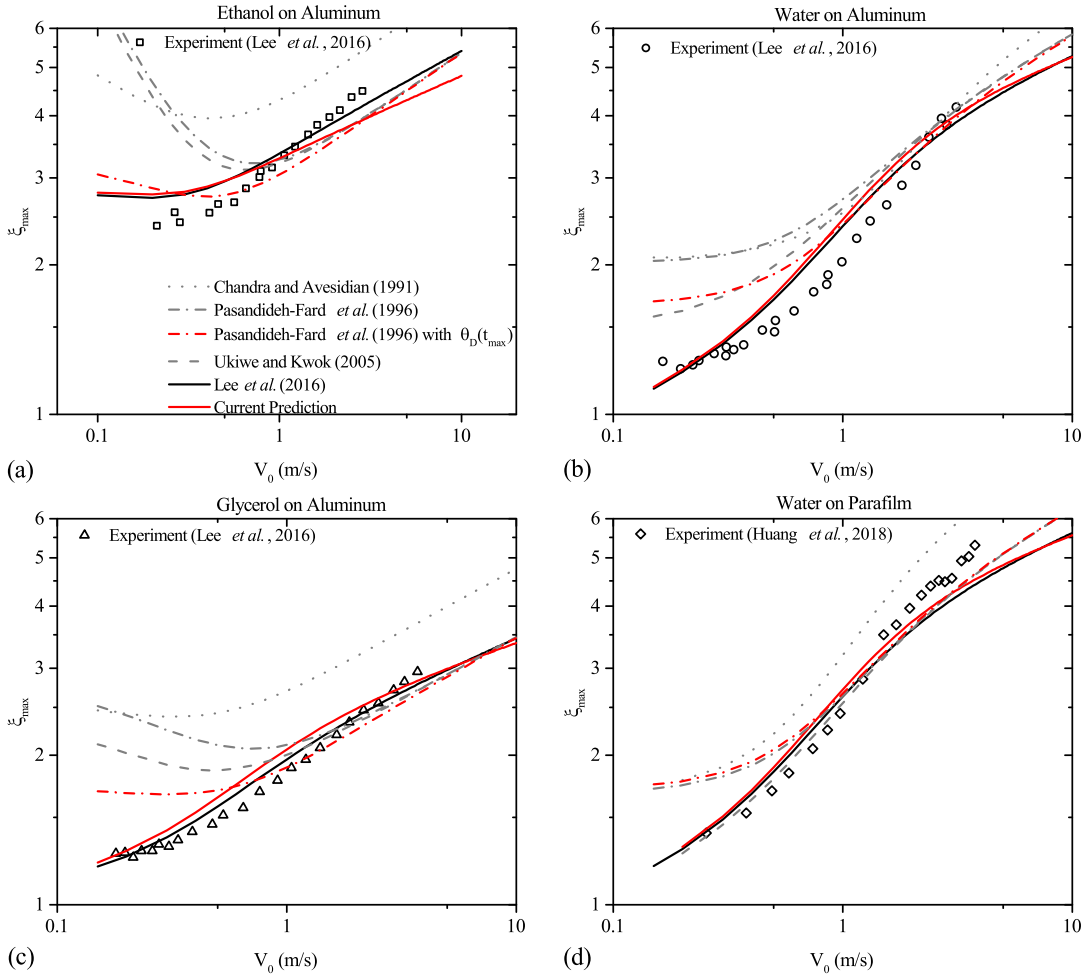

FIGURE **5.10**: Comparison between maximum spreading factor predictions and experimental results. (a), (b), (c) presents experiments of ethanol, water, glycerol droplets impacting on aluminium surface by Lee *et al.* [56], respectively. (d) presents experiments of water droplets impacting on parafilm surface by Huang and Chen [40]. The red and black lines indicate predictions calculated with $\theta_D(t_{max})$, grey lines for predictions with θ. The legend for lines is given in (a).

The Fig.5.10 has shown that our current model Eq.(5.30) provides similar prediction of ξ_{max} as the model of Lee *et al.* [56] and fits well with the experimental results given by Lee *et al.* [56] and Huang and Chen [40]. As the model [56] predicts ξ_{max} best among the existing models discussed above, a comparison is then conducted between the model by Lee *et al.* [56] and our simulations. Two representative cases are chosen from our simulations, one is a droplet impacts

at low velocity ($V_0 = 5\ m/s$), the other one is at high impact velocity ($V_0 = 20\ m/s$). In both cases, the dynamic viscosity of the droplet is varied in the range of $0.01 \sim 0.1\ Pa \cdot s$. In this comparison (Fig.5.11), the spread factor ξ_{max} and dissipation work W_{max} at maximum spreading state are compared. The Fig.5.11 (a-1) and (a-2) plots the spread factor and the dissipation work versus viscosity in the case of low impact velocity, respectively. The current model gives better prediction of ξ_{max} than the model of Lee *et al.* [56]. More importantly, the prediction by the current model falls between the values of ξ_{max} and ξ_{c_max}, and close to the maximum spreading factor with lower viscosity and close to maximum contact factor. This phenomenon could be explained with the geometric shapes presented in Fig.4.1 (a). The shape that the droplet maintains at maximum spreading with high viscosity is more like a cylinder, whereas the shape that droplet forms is more like a disk with a rim with low viscosity. The current model slightly over-predicts the dissipation work accumulated at the maximum spreading, whereas the model by Lee *et al.* [56] gives a relatively unsatisfying prediction of W_{max}.

At high velocity, the predictions given by the current model and Lee *et al.* [56] both underestimate the maximum spreading factor, as they overestimate the dissipation work W_{max}. The current model under-predicts ξ_{max} by 10% to 17% and Lee *et al.* [56] by 50% to the our simulation results. As concluded in Chapter 4, the correlation Eq.(3.17) between ξ_{max} and t^*_{max} provides better prediction of t_{max} than Eq.(3.10) by Lee *et al.* [56], which leads to a more accurate estimation of the dissipation work W_{max} accumulated at maximum spreading, and a better model predicting the maximum spreading factor ξ_{max} at last.

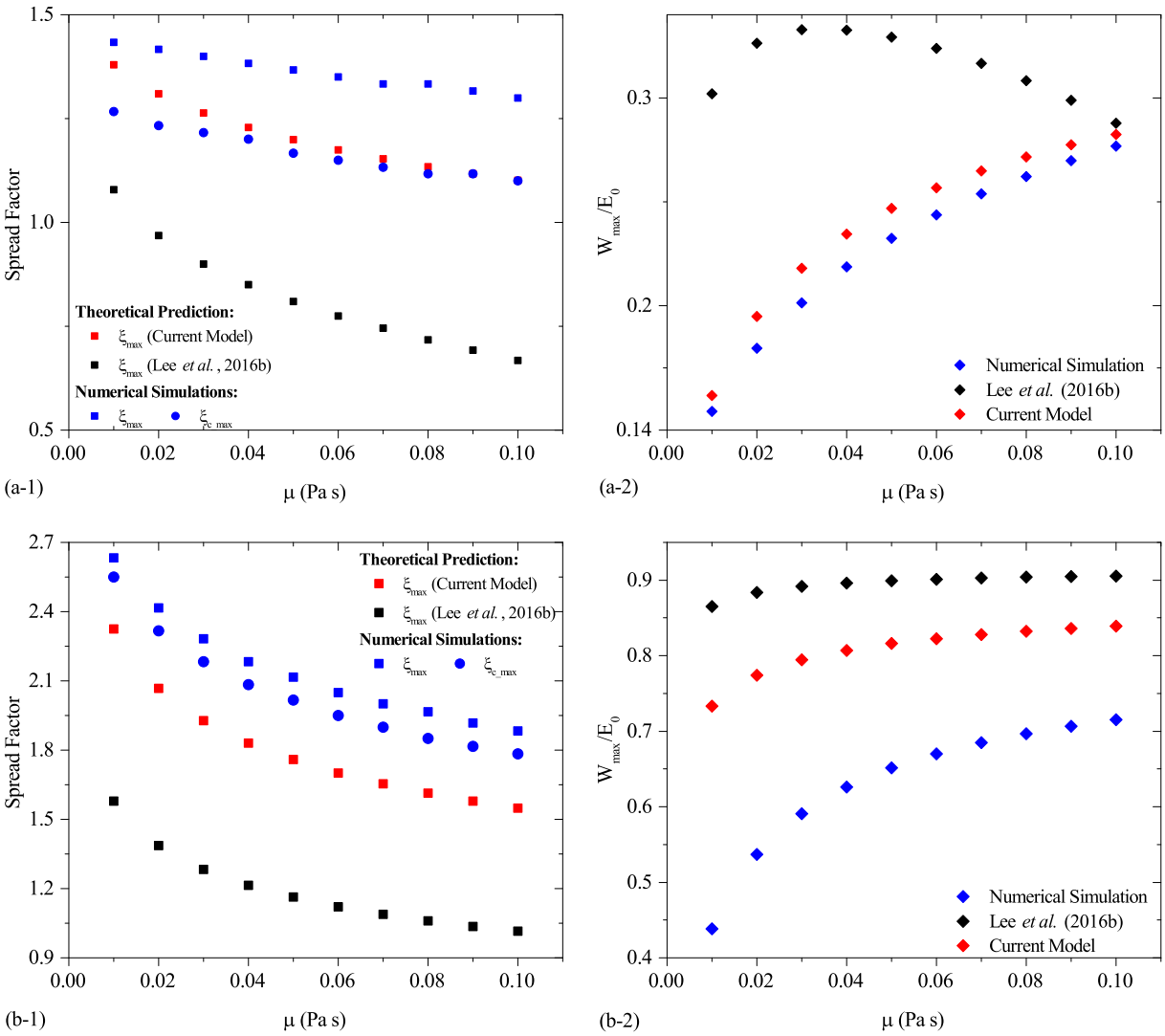

FIGURE **5.11**: Comparison of maximum spreading factor predictions ξ_{max} ((a-1) and (b-1)) and dissipation work W_{max} ((a-2) and (b-2)) between theoretical predictions and numerical simulations with varied viscosity. The first row (a) presents the case in which a ceramic droplet impacts at $V_0 = 5\ m/s$ on a superhydrophobic surface, $We = 4.275$. The row (b) gives the case where a ceramic droplet impacts at $V_0 = 20\ m/s$ on a superhydrophobic surface, $We = 68.4$.

5.3 Summary

This chapter starts with a overall analysis on the energy balance of the droplet from the instant the droplet impacts on a superhydorphobic surface to the instant the droplet rebounds off from the surface. Then, this analysis is divided into two parts: the spreading and the retraction stage.

In spreading stage, the initial kinetic energy drives the droplet to spread, and the surface energy and dissipation play against the spreading. In the retraction stage, the surface energy stored in the droplet forces the droplet to recoil. The surface energy transforms partly to the kinetic energy, and is dissipated by the viscous force simultaneously in the early retraction. Later, the regained kinetic energy contributes to the augmentation of the dissipation work, whereas the surface energy changes slightly with time. Regarding the dissipation work amount accumulated in spreading and retraction stage, we find the ratio between the dissipation W_{max} in spreading stage and the total dissipation W_{BC} scales as an exponential function of $WeRe^{-3/4}$.

In the analysis, we highlight the two important states: the maximum spreading state and the boucing-off state. The contributions of energy components at these two states are given, and the influences of dynamic viscosity on the portions of energy terms are investigated. Considering the maximum spreading state, a brief review is given on the previous theoretical prediction models based on the energy conservation and the cylinder assumption. With the correlation Eq.(3.17) in Chapter 4, we modified the model of Ukiwe and Kwok [99] in the estimation of the dissipation work W_{max}. Based on the validations against experiments and comparisons with our simulations, we concluded that the current model provides satisfying predictions of maximum spreading factor.

Chapter 6

General Conclusions

In this manuscript, we present a numerical study of liquid droplets' normal impact on solid surfaces with the numerics code Thetis. We first introduce the contact angle as a boundary condition into the numeric algorithm, then several validations with existing experiments are performed. Then vary the liquid properties (surface tension and viscosity), impact conditions (impact velocity and wettability) in a systematical way to investigate their influences on the spreading dynamics, maximum spreading diameter and time and the retraction dynamics. All these simulations indicate that the three energy components, the kinetic energy, the surface energy and the dissipation work are vital to the dynamics and outcomes of the droplets' impaction. We have investigated the early spreading dynamics after droplets' impaction. We find that in the early spreading stage, the strong liquid-solid interaction existing on hydrophilic surfaces restricts the spreading more severely than the relatively weak liquid-solid interaction on the hydrophobic surfaces. It is concluded that the wettability of the surface has little influences on the jetting time, furthermore, we observed the jetting time scales as $t_j/(\rho D_0^3/\sigma) \sim V_0^{-1}$.
Based on the numerous works on the maximum spreading diameter, we have studied, in detail, the maximum spreading diameter and the maximum spreading time for droplets impacting on hydrophobic surfaces. To consider the influences of wettability on maximum spreading diameter, the maximum contact diameter is also investigated and could be rescaled by the interpolation between two capillary and viscous regimes. Compared to the method considering the influences of wettability by eliminating the spreading diameter at zero velocity, using contact diameter presents better scale behaviour and will not over-estimate the influences of wettability at high impact velocity. We observed the dimensionless rim radius, the difference $\xi_{max} - \xi_{c\_max}$,which

is largely dependent on the inertial forces, scales as $0.3We^{-1/4}$. In the meantime, the maximum spreading time is investigated systematically for the first time, the dimensionless spreading time t^*_{max} increases with $We^{0.3}$ within the range $1 < We < 300$. At low velocity, similar to the capillary regimes, the effects of viscosity on t^*_{max} could be neglected. While at high velocity, the influence of viscosity becomes important and makes t^*_{max} dependent on $Re^{1/10}$. After being normalised with $Re^{1/5}$, we obtain $t^*_{max}/Re^{1/5} = 0.375(WeRe^{-2/5})^{0.264}$, which fits well with available experimental results. Combing the two scales of ξ_{max} and t_{max}, a correlation is successfully established as $\xi_{max}/t^*_{max} = 2We^{-1/10}$. This correlation improves the prediction accuracy largely compared to the existing prediction models, and agrees nicely with the experiments carried out at low to high velocity on hydrophilic or hydrophobic surfaces. More importantly, this correlation improves the accuracy of the existing theoretical models predicting the maximum spreading based on energy conservation.

We also conducted an analysis on the the contact time between droplets and surface. To supplement the work by Bartolo *et al.* [8], the simulations are designed as the droplets' retractions is in the capillary-viscous regime. We find that the contact time is independent on impact velocity in this capillary-viscous regime, then we conclude that the influences of impact velocity on contact time could be neglected in both the capillary-inertia and capillary-viscous regimes. Furthermore, the dimensionless contact time scales as a function taking the form $Re \cdot f(Oh)$ in the capillary-viscous regime. Besides, we also include the scale of the retraction time t_r, which shares the similar scaling with the contact time as the maximum spreading time occupies a little portion in the whole contact time from impaction to rebounding.

Lastly, the energetic analysis on droplets' dynamics is provided to help understand the driving or dominating factors behind the droplets' dynamics. The energy analysis in this thesis is divided into two parts: the spreading and the retraction stage. We extend the previous work on spreading energy balance by studying droplets impacting on superhydrophobic surfaces with more details on the transformation among the three energy components. The analysis on energy balance in retraction is conducted for the first time, which is of significance in understanding the physics after the droplet reaching its maximum spreading state. In the retraction stage, the surface energy stored in the droplet motors the droplets' retraction, and majorly dissipated by the viscous forces. The droplet's kinetic energy is usually assumed to vanish at maximum spreading state. While in the studies on the energy analysis, this assumption no longer validates. As for the

cases with low viscosity at low impact velocity, the percent of the surface energy at maximum spreading state transformed into kinetic energy and being dissipated are similar, around 50%, which indicates that the cross-over between the capillary-viscous regime and capillary-inertial regime in the retraction dynamics. And in our investigation on most important state during the dynamics, the maximum spreading state, we improved the model of Ukiwe and Kwok [99] by introducing the correlation $\xi_{max}/t^*_{max} = 2We^{-1/10}$ to the estimation of dissipation work. Compared to the recent model proposed by Lee *et al.* [56], our model provides a good prediction of maximum spreading factor based on a validation against experiments, and a better estimation of the dissipation work compared to the results of our simulations.

All of these studies have led us to a deeper understanding on the droplets' spreading dynamics and characteristic scales of the maximum spreading diameter, maximum spreading time and contact time. These scalings could have an impact on the theoretical models based on energy conservation and could be useful in numerical simulations related to plasma spay. However, the present work can be extended in several direction.

In the present work, only the normal impact of liquid droplets on smooth surfaces has been studied. A natural extension is to the oblique impaction of liquid droplets to the target surface. Such an extension is not direct but expected to be particularly rich and important from the mechanical point of view. Although the scales of maximum spreading diameter could be applied to the cases with rough surfaces, it is still necessary to conduct simulations of liquid droplets impacting on rough surface to achieve a comprehensive understanding on the influences of roughness on spreading diameter. When conducting simulations of droplets impacting on rough surfaces, the contact angle model should be improved to the dynamic contact angle model [see, e.g., 5, 92, 83, 102].

Secondly, the heat transfer between droplets and surfaces should be taken into account. The temperature of the target substrate affects the outcomes of droplet impact enormously [27]. Accompany the heat transfer, the phase change of droplets is also an important issue to be investigated. Although many studies on millimetre-size droplets have concluded that the solidification is much slower than the spreading, this conclusion remains debatable for small size droplets [see, e.g., 25, 109].

References

[1] Antonini, C., Amirfazli, A. and Marengo, M., 2012. Drop impact and wettability: From hydrophilic to superhydrophobic surfaces. Physics of Fluids, 24(10), p.102104.

[2] Antonini, C., Villa, F., Bernagozzi, I., Amirfazli, A. and Marengo, M., 2013. Drop rebound after impact: The role of the receding contact angle. Langmuir, 29(52), pp.16045-16050.

[3] Attané, P., Girard, F. and Morin, V., 2007. An energy balance approach of the dynamics of drop impact on a solid surface. Physics of Fluids, 19(1), p.012101.

[4] Attinger, D., Zhao, Z. and Poulikakos, D., 2000. An experimental study of molten microdroplet surface deposition and solidification: transient behavior and wetting angle dynamics. Journal of Heat Transfer, 122(3), pp.544-556.

[5] Afkhami, S., Zaleski, S. and Bussmann, M., 2009. A mesh-dependent model for applying dynamic contact angles to VOF simulations. Journal of Computational Physics, 228(15), pp.5370-5389.

[6] Aziz, S.D. and Chandra, S., 2000. Impact, recoil and splashing of molten metal droplets. International Journal of Hear and Mass Transfer, 43(16), pp.2841-2857.

[7] Bhola, R. and Chandra, S., 1999. Parameters controlling solidification of molten wax droplets falling on a solid surface. Journal of Materials Science, 34(19), pp.4883-4894.

[8] Bartolo, D., Josserand, C. and Bonn, D., 2005. Retraction dynamics of aqueous drops upon impact on non-wetting surfaces. Journal of Fluid Mechanics, 545, pp.329-338.

[9] Bennett, T. and Poulikakos, D., 1993. Splat-quench solidification: estimating the maximum spreading of a droplet impacting a solid surface. Journal of Materials Science, 28(4), pp.963-970.

[10] Bergeron, V., Bonn, D., Martin, J.Y. and Vovelle, L., 2000. Controlling droplet deposition with polymer additives. Nature, 405(6788), p.772.

[11] Bird, J.C., Mandre, S. and Stone, H.A., 2008. Short-time dynamics of partial wetting. Physical Review Letters, 100(23), p.234501.

[12] Biance, A.L., Clanet, C. and Quere, D., 2004. First steps in the spreading of a liquid droplet. Physical Review E, 69(1), p.016301.

[13] Brackbill, J.U., Kothe, D.B. and Zemach, C., 1992. A continuum method for modeling surface tension. Journal of Computational Physics, 100(2), pp.335-354.

[14] Blossey, R., 2003. Self-cleaning surfaces - virtual realities. Nature Materials, 2(5), p.301.

[15] Bussmann, M., Chandra, S. and Mostaghimi, J., 2000. Modeling the splash of a droplet impacting a solid surface. Physics of Fluids, 12(12), pp.3121-3132.

[16] Chandra, S. and Avedisian, C.T., 1991. On the collision of a droplet with a solid surface. Proceedings of the Royal Society of London A: Mathematical, Physical and Engineering Sciences, 432, pp.13-41.

[17] Clanet, C., Béguin, C., Richard, D. and Quéré, D., 2004. Maximal deformation of an impacting drop. Journal of Fluid Mechanics. 517: 199-208.

[18] Collings, E.W., Markworth, A.J., McCoy, J.K. and Saunders, J.H., 1990. Splat-quench solidification of freely falling liquid-metal droplets by impact on a planar substrate. Journal of Materials Science, 25(8), pp.3677-3682.

[19] Chibowski, E. and Terpilowski, K., 2008. Surface free energy of sulfur - Revisited: I. Yellow and orange samples solidified against glass surface. Journal of Colloid and Interface Science, 319(2), pp.505-513.

[20] Caruyer, C., Vincent, S., Meillot, E. and Caltagirone, J.P., 2010. Modeling the first instant of the interaction between a liquid and a plasma jet with a compressible approach. Surface and Coatings Technology, 205(4), pp.974-979.

[21] Delhaye, J. 1974. Jump conditions and entropy sources in two-phase systems. Local instant formulation. International Journal of Multiphase Flow, 1, pp.395-409.

[22] de Ruiter, J., Oh, J.M., van den Ende, D. and Mugele, F., 2012. Dynamics of collapse of air films in drop impact. Physical Review Letters, 108(7), p.074505.

[23] Dhiman, R., McDonald, A.G. and Chandra, S., 2007. Predicting splat morphology in a thermal spray process. Surface and Coatings Technology, 201(18), pp.7789-7801.

[24] Duchemin, L. and Josserand, C., 2011. Curvature singularity and film-skating during drop impact. Physics of Fluids, 23(9), p.091701.

[25] Dykhuizen, R.C., 1994. Review of impact and solidification of molten thermal spray droplets. Journal of Thermal Spray Technology, 3(4), pp.351-361.

[26] Eggers, J., Fontelos, M.A., Josserand, C. and Zaleski, S., 2010. Drop dynamics after impact on a solid wall: theory and simulations. Physics of Fluids, 22(6), p.062101.

[27] Escure, C., Vardelle, M. and Fauchais, P., 2003. Experimental and theoretical study of the impact of alumina droplets on cold and hot substrates. Plasma Chemistry and Plasma Processing, 23(2), pp.185-221.

[28] Fuster, D., Agbaglah, G., Josserand, C., Popinet, S. and Zaleski, S., 2009. Numerical simulation of droplets, bubbles and waves: state of the art. Fluid Dynamics Research, 41(6), p.065001.

[29] Fauchais, P., Vardelle, A., Vardelle, M. and Fukumoto, M., 2004. Knowledge concerning splat formation: an invited review. Journal of Thermal Spray Technology, 13(3), pp.337-360.

[30] Fukai, J., Shiiba, T., Yamamoto, T., Miyatake, O., Poulikakos, D., Megaridis, C.M. and Zhao, Z., 1995. Wetting effects on the spreading of a liquid droplet surface : Experiment and modelling colliding with a flat. Physics of Fluids, 7(2), pp.236-247.

[31] Gao, X. and Jiang, L., 2004. Biophysics: water-repellent legs of water striders. Nature, 432(7013), p.36.

[32] Gao, X. and Li, R., 2014. Spread and recoiling of liquid droplets impacting solid surfaces. AIChE (American Institute of Chemical Engineers) Journal, 60(7), pp.2683-2691.

[33] Ghafouri-Azar, R., Shakeri, S., Chandra, S. and Mostaghimi, J., 2003. Interactions between molten metal droplets impinging on a solid surface. International Journal of Heat and Mass Transfer, 46(8), pp.1395-1407.

[34] Gueyffier, D., Li, J., Nadim, A., Scardovelli, R. and Zaleski, S., 1999. Volume-of-fluid interface tracking with smoothed surface stress methods for three-dimensional flows. Journal of Computational Physics, 152(2), pp.423-456.

[35] Gao, L. and McCarthy, T.J., 2006. Contact angle hysteresis explained. Langmuir, 22(14), pp.6234-6237.

[36] Guillaument, R., Vincent, S. and Caltagirone, J.P., 2015. An original algorithm for VOF based method to handle wetting effect in multiphase flow simulation. Mechanics Research Communications, 63, pp.26-32.

[37] Hartley, G.S. and Brunskill, R.T., 1958. Reflection of water droplets from surfaces. Surface Phenomena in Chemistry and Biology, pp.214-223.

[38] Healy, W. M., Hartley, J. G. and Abdel-Khalik, S. I. 1996. Comparison between theoretical models and experimental data for the spreading of liquid droplets impacting a solid surface. International Journal of Heat and Mass Transfer, 39(14), pp.3079-3082.

[39] Hirt, C.W. and Nichols, B.D., 1981. Volume of fluid (VOF) method for the dynamics of free boundaries. Journal of Computational Physics, 39(1), pp.201-225.

[40] Huang, H.M. and Chen, X.P. 2018. Energetic analysis of drop's maximum spreading on solid surface with low impact speed. Physics of Fluids, 30(2), p.022106.

[41] Harlow, F.H. and Shannon, J.P., 1967. The splash of a liquid drop. Journal of Applied Physics, 38(10), pp.3855-3866.

[42] Harlow, F.H. and Welch, J.E., 1965. Numerical calculation of time dependent viscous incompressible flow of fluid with free surface. The Physics of Fluids, 8(12), pp.2182-2189.

[43] Jamet, D., Torres, D. and Brackbill, J.U., 2002. On the theory and computation of surface tension: the elimination of parasitic currents through energy conservation in the second-gradient method. Journal of Computational Physics, 182(1), pp.262-276.

[44] Jian, Z., Josserand, C., Popinet, S., Ray, P. and Zaleski, S., 2018. Two mechanisms of droplet splashing on a solid substrate. Journal of Fluid Mechanics, 835, pp.1065-1086.

[45] Jung, S., Tiwari, M.K., Doan, N.V. and Poulikakos, D., 2012. Mechanism of supercooled droplet freezing on surfaces. Nature Communications, 3, p.615.

[46] Josserand, C. and Thoroddsen, S.T., 2016. Droplet impact on a solid surface. Annual Review of Fluid Mechanics, 48, pp.365-391.

[47] Kataoka, I., 1986. Local instant formulation of two-phase flow. International Journal of Multiphase Flow, 12(5), pp.745-758.

[48] Kim, H.Y. and Chun, J.H., 2001. The recoiling of liquid droplets upon collision with solid surfaces. Physics of Fluids, 13(3), pp.643-659.

[49] Kistler, S.F., 1993. Hydrodynamics of wetting; Wettability; Marcel Dekker: New York, 6, pp.311-430.

[50] Korobkin, A.A., Ellis, A.S. and Smith, F.T., 2008. Trapping of air in impact between a body and shallow water. Journal of Fluid Mechanics, 611, pp.365-394.

[51] Kobayashi, K., Konno, K., Yaguchi, H., Fujii, H., Sanada, T. and Watanabe, M., 2016. Early stage of nanodroplet impact on solid wall. Physics of Fluids, 28(3), p.032002.

[52] Laan, N., de Bruin, K.G., Bartolo, D., Josserand, C. and Bonn, D., 2014. Maximum diameter of impacting liquid droplets. Physical Review Applied, 2(4), p.044018.

[53] Le Bot, C., Vincent, S. and Arquis, E., 2005. Impact and solidification of indium droplets on a cold substrate. International Journal of Thermal Sciences, 44(3), pp.219-233.

[54] Le Bot, C., Vincent, S., Meillot, E., Sarret, F., Caltagirone, J.P. and Bianchi, L., 2015. Numerical simulation of several impacting ceramic droplets with liquid/solid phase change. Surface and Coatings Technology, 268, pp.272-277.

[55] Lee, J.B., Derome, D., Dolatabadi, A. and Carmeliet, J., 2016. Energy budget of liquid drop impact at maximum spreading: numerical simulations and experiments. Langmuir, 32(5), pp.1279-1288.

[56] Lee, J.B., Derome, D., Guyer, R. and Carmeliet, J., 2016. Modeling the maximum spreading of liquid droplets impacting wetting and nonwetting surfaces. Langmuir, 32(5), pp.1299-1308.

[57] Lee, J.B., Laan, N., de Bruin, K.G., Skantzaris, G., Shahidzadeh, N., Derome, D., Carmeliet, J. and Bonn, D., 2016. Universal rescaling of drop impact on smooth and rough surfaces. Journal of Fluid Mechanics, 786.

[58] Liu, Y., Moevius, L., Xu, X., Qian, T., Yeomans, J.M. and Wang, Z., 2014. Pancake bouncing on superhydrophobic surfaces. Nature Physics, 10(7), p.515.

[59] Madejski, J., 1976. Solidification of droplets on a cold surface. International Journal of Heat and Mass Transfer, 19(9), pp.1009-1013.

[60] Meillot, E., Damiani, D., Vincent, S., Caruyer, C. and Caltagirone, J.P., 2013. Analysis by modeling of plasma flow interactions with liquid injection. Surface and Coatings Technology, 220, pp.149-156.

[61] Mandre, S. and Brenner, M.P., 2012. The mechanism of a splash on a dry solid surface. Journal of Fluid Mechanics, 690, pp.148-172.

[62] Mani, M., Mandre, S. and Brenner, M.P., 2010. Events before droplet splashing on a solid surface. Journal of Fluid Mechanics, 647, pp.163-185.

[63] Manservisi, S. and Scardovelli, R., 2009. A variational approach to the contact angle dynamics of spreading droplets. Computers and Fluids, 38(2), pp.406-424.

[64] Mao, T., Kuhn, D., Tran, H., 1997. Spread and rebound of liquid droplets upon impact on flat surfaces. AIChE Journal, 43(9), pp.2169-2179.

[65] McPherson, R., 1989. A review of microstructure and properties of plasma sprayed ceramic coatings. Surface and Coatings Technology, 39, pp.173-181.

[66] McDonald, A., Lamontagne, M., Moreau, C. and Chandra, S., 2006. Impact of plasma-sprayed metal particles on hot and cold glass surfaces. Thin Solid Films, 514(1-2), pp.212-222.

[67] Mellali, M., Fauchais, P. and Grimaud, A., 1996. Influence of substrate roughness and temperature on the adhesion/cohesion of alumina coatings. Surface and Coatings Technology, 81(2-3), pp.275-286.

[68] Mishchenko, L., Hatton, B., Bahadur, V., Taylor, J.A., Krupenkin, T. and Aizenberg, J., 2010. Design of ice-free nanostructured surfaces based on repulsion of impacting water droplets. ACS Nano (American Chemical Society Nano), 4(12), pp.7699-7707.

[69] Moreira, A.L.N., Moita, A.S. and Panao, M.R., 2010. Advances and challenges in explaining fuel spray impingement: How much of single droplet impact research is useful?. Progress in Energy and Combustion Science, 36(5), pp.554-580.

[70] Mostaghimi, J., Chandra, S., Ghafouri-Azar, R. and Dolatabadi, A., 2003. Modeling thermal spray coating processes: a powerful tool in design and optimization. Surface and Coatings Technology, 163, pp.1-11.

[71] Okumura, K., Chevy, F., Richard, D., Quéré, D. and Clanet, C., 2003. Water spring: A model for bouncing drops. Europhysics Letters, 62(2), p.237.

[72] Pasandideh-Fard, M., Qiao, Y.M., Chandra, S. and Mostaghimi, J., 1996. Capillary effects during droplet impact on a solid surface. Physics of Fluids, 8(3), pp.650-659.

[73] Pasandideh-Fard, M., Pershin, V., Chandra, S., and Mostaghimi. 2002. Splat shapes in a thermal spray coating process: Simulations and experiments. Journal of Thermal Spray Technology, 11(2), pp.206-217.

[74] Popinet, S., 2009. An accurate adaptive solver for surface-tension-driven interfacial flows. Journal of Computational Physics, 228(16), pp.5838-5866.

[75] Qian, T., Wang, X.P. and Sheng, P., 2006. A variational approach to moving contact line hydrodynamics. Journal of Fluid Mechanics, 564, pp.333-360.

[76] Quéré, D., 2005. Non-sticking drops. Reports on Progress in Physics, 68(11), p.2495.

[77] Quéré, D., 2008. Wetting and roughness. Annual Reviews of Materials Research, 38, pp.71-99.

[78] Rein, M., 1993. Phenomena of liquid droplet impact on solid and liquid surfaces. Fluid Dynamics Research, 12(2), pp.61-93.

[79] Reyssat, M., Pépin, A., Marty, F., Chen, Y. and Quéré, D., 2006. Bouncing transitions on microtextured materials. Europhysics Letters, 74(2), p.306.

[80] Richard, Denis, Christophe Clanet, and David Quéré. 2002. Surface phenomena: Contact time of a bouncing drop. Nature 417, no. 6891: 811.

[81] Rioboo, R., Tropea, C. and Marengo, M., 2001. Outcomes from a drop impact on solid surfaces. Atomization and Sprays, 11(2), pp.155-165.

[82] Roisman, I.V., Rioboo, R. and Tropea, C., 2002. Normal impact of a liquid drop on a dry surface: model for spreading and receding. Proceedings of the Royal Society of London A: Mathematical, Physical and Engineering Sciences, 458(2022), pp.1411-1430.

[83] Roisman, I.V., Opfer, L., Tropea, C., Raessi, M., Mostaghimi, J. and Chandra, S., 2008. Drop impact onto a dry surface: Role of the dynamic contact angle. Colloids and Surfaces A: Physicochemical and Engineering Aspects, 322(1-3), pp.183-191.

[84] Roisman, I.V., Berberović, E. and Tropea, C., 2009. Inertia dominated drop collisions. I. On the universal flow in the lamella. Physics of Fluids, 21(5), p.052103.

[85] Roisman, I.V., 2009. Inertia dominated drop collisions. II. An analytical solution of the Navier - Stokes equations for a spreading viscous film. Physics of Fluids, 21(5), p.052104.

[86] Stow, C.D. and Hadfield, M.G., 1981. An experimental investigation of fluid flow resulting from the impact of a water drop with an unyielding dry surface. Proceedings of The Royal Society A, 373(1755), pp.419-441.

[87] San Lee, J., Weon, B.M., Je, J.H. and Fezzaa, K., 2012. How does an air film evolve into a bubble during drop impact?. Physical Review Letters, 109(20), p.204501.

[88] Šikalo, Š., Marengo, M., Tropea, C. and Gani'c, E.N., 2002. Analysis of impact of droplets on horizontal surfaces. Experimental Thermal and Fluid Science, 25(7), pp.503-510.

[89] Schiaffino, S. and Sonin, A.A., 1997. Molten droplet deposition and solidification at low Weber numbers. Physics of Fluids, 9(11), pp.3172-3187.

[90] Schiaffino, S. and Sonin, A.A., 1997. Motion and arrest of a molten contact line on a cold surface: An experimental study. Physics of Fluids, 9(8), pp.2217-2226.

[91] Schiaffino, S. and Sonin, A. a., 1997. Formation and stability of liquid and molten beads on a solid surface. Journal of Fluid Mechanics, 343, pp.95-110.

[92] Šikalo, Š., Tropea, C. and Ganić, E.N., 2005a. Dynamic wetting angle of a spreading droplet. Experimental Thermal and Fluid Science, 29(7), pp.795-802.

[93] Šikalo, Š., Wilhelm, H.D., Roisman, I.V., Jakirlić, S. and Tropea, C., 2005b. Dynamic contact angle of spreading droplets: Experiments and simulations. Physics of Fluids, 17(6), p.062103.

[94] Sussman, M., Smereka, P. and Osher, S., 1994. A level set approach for computing solutions to incompressible two-phase flow. Journal of Computational Physics, 114(1), pp.146-159.

[95] Thoroddsen, S.T., Etoh, T.G. and Takehara, K., 2008. High-speed imaging of drops and bubbles. Annual Review of Fluid Mechanics, 40, pp.257-285.

[96] Tanaka, Y. and Fukumoto, M., 1999. Investigation of dominating factors on flattening behavior of plasma sprayed ceramic particles. Surface and Coatings Technology, 120-121, pp.124-130.

[97] Tadmor, R., 2004. Line energy and the relation between advancing, receding, and Young contact angles. Langmuir, 20(18), pp.7659-7664.

[98] Thoroddsen, S.T., Etoh, T.G., Takehara, K., Ootsuka, N., Hatsuki, Y., 2005. The air bubble entrapped under a drop impacting on a solid surface. Journal of Fluid Mechanics, 545, pp.203-212.

[99] Ukiwe, C., Kwok, D.Y., 2005. On the maximum spreading diameter of impacting droplets on well-prepared solid surfaces. Langmuir, 21(2), pp.666-673.

[100] Unverdi, S.O. and Tryggvason, G., 1992. A front-tracking method for viscous, incompressible, multi-fluid flows. Journal of Computational Physics, 100(1), pp.25-37.

[101] Vardelle, M., Vardelle, A., Leger, A.C., Fauchais, P. and Gobin, D., 1995. Influence of particle parameters at impact on splat formation and solidification in plasma spraying processes. Journal of Thermal Spray Technology, 4(1), pp.50-58.

[102] Vadillo, D.C., Soucemarianadin, A., Delattre, C. and Roux, D.C.D., 2009. Dynamic contact angle effects onto the maximum drop impact spreading on solid surfaces. Physics of Fluids, 21(12), p.122002.

[103] Vincent, S. and Caltagirone, J.P., 1999. Efficient solving method for unsteady incompressible interfacial flow problems. International Journal for Numerical Methods in Fluids, 30(6), pp.795-811.

[104] Vincent, S., Caltagirone, J.P. and Arquis, E., 2000. Numerical simulation of liquid metal particles impacting onto solid substrate: description of hydrodynamic processes and heat transfers. High Temperature Material Processes: An International Quarterly of High-Technology Plasma Processes, 4(1).

[105] Vincent, S., Randrianarivelo, T.N., Pianet, G. and Caltagirone, J.P., 2007. Local penalty methods for flows interacting with moving solids at high Reynolds numbers. Computers and Fluids, 36(5), pp.902-913.

[106] Vincent, S., Balmigere, G., Caruyer, C., Meillot, E. and Caltagirone, J.P., 2009. Contribution to the modeling of the interaction between a plasma flow and a liquid jet. Surface and Coatings Technology, 203(15), pp.2162-2171.

[107] Vincent, S., Sarthou, A., Caltagirone, J.P., Sonilhac, F., Février, P., Mignot, C. and Pianet, G., 2011. Augmented Lagrangian and penalty methods for the simulation of two-phase flows interacting with moving solids. Application to hydroplaning flows interacting with real tire tread patterns. Journal of Computational Physics, 230(4), pp.956-983.

[108] Vincent, S., Le Bot, C., Sarret, F., Meillot, E., Caltagirone, J.-P., Bianchi, L. 2015. Penalty and Eulerian-Lagrangian VOF methods for impact and solidification of metal droplets plasma spray process. Computers and Fluids, 113, pp.32-41.

[109] Wan, Y.P., Zhang, H., Jiang, X.Y., Sampath, S. and Prasad, V., 2001. Role of solidification, substrate temperature and Reynolds number on droplet spreading in thermal spray deposition: measurements and modeling. Journal of Heat Transfer, 123(2), pp.382-389.

[110] Weisensee, P., Ma, J., King, W. and Miljkovic, N., 2018. Controlling the Contact Times of Bouncing Droplets: Droplet Impact on Vibrating Surfaces. Journal of Heat Transfer, 140(3), p.030901.

[111] Weisensee, P.B., Tian, J., Miljkovic, N. and King, W.P., 2016. Water droplet impact on elastic superhydrophobic surfaces. Scientific Reports, 6, p.30328.

[112] Wildeman, S., Visser, C.W., Sun, C. and Lohse, D., 2016. On the spreading of impacting drops. Journal of Fluid Mechanics, 805, pp.636-655.

[113] Winkels, K.G., Weijs, J.H., Eddi, A. and Snoeijer, J.H., 2012. Initial spreading of low-viscosity droplets on partially wetting surfaces. Physical Review E, 85(5), p.055301.

[114] Worthington, A.M., 1876. On the forms assumed by droplets of liquids falling vertically on a horizontal plate. Proceedings of The Royal Society of London, 25(171-178), pp.261-272.

[115] Xu, L., Zhang, W.W., Nagel, S.R., 2005. Drop splashing on a dry smooth surface. Physical Review Letters, 94(18), p.184505.

[116] Yarin, A.L., 2006. Droplet impact dynamics: splashing, spreading, receding, bouncing.... Annual Review of Fluid Mechanics, 38(1), pp.159-192.

[117] Yokoi, K., Vadillo, D., Hinch, J. and Hutchings, I., 2009. Numerical studies of the influence of the dynamic contact angle on a droplet impacting on a dry surface. Physics of Fluids, 21(7), p.072102.

[118] Young, T., 1805. III. An essay on the cohesion of fluids. Philosophical Transactions of The Royal Society of London, 95, pp.65-87.

[119] Youngs, D.L., 1982, Time-dependent multimaterial flow with large fluid distortion. Morton K.W. and Baines M.J. (editors), Numerical Methods for Fluid Dynamics, Academic Press, p.27.

[120] Yonemoto, Y. and Kunugi, T., 2017. Analytical consideration of liquid droplet impingement on solid surfaces. Scientific Reports, 7(1), p.2362.

[121] Zaleski, S., Li, J., Scardovelli, R. and Zanetti, G., 1997. Direct simulation of multiphase flows with density variations. In IUTAM Symposium on Variable Density Low-Speed Turbulent Flows. Springer Netherlands, pp.51-58.

Appendix A

The properties of liquids and impact conditions in the experiments by Lee *et al.* [56] and Huang and Chen [40]

The properties of liquids and impact conditions in the experiments performed by Lee *et al.* [56] are given in Table.A.1. The equilibrium contact angle and $\theta_{max}(t_{max})$ are listed in Table.A.2

TABLEAU **A.1**: Impact Conditions and Properties of Liquids at 25° [56]

	Ethanol	Water	Glycerol
Density ρ (kg/m^3)	789	0.023	0.0012
Surface Tension σ (N/m)	998	0.073	0.001
Viscosity μ $(Pa \cdot s)$	1158	0.068	0.01
Initial Diameter D_0 (m)	0.0018	0.002	0.0018
Weber Number We	$2.5 - 315$	$1.0 - 290$	$1.1 - 414$
Reynolds Number Re	$260 - 2900$	$350 - 6300$	$40 - 750$

TABLEAU **A.2**: Contact angles measured of liquid droplet on surfaces at 25° [56]

	Ethanol	Water	Glycerol
θ_{eq} (deg) on Aluminum	~ 0	87.6 ± 7.1	59.8 ± 2.6
θ_{eq} (deg) on Steel	~ 0	60.9 ± 3.3	52.4 ± 3.7
θ_{eq} (deg) on Parafilm	21.3 ± 1.9	109.6 ± 2.6	94.4 ± 3.4
θ_{adv} (deg) on Aluminum	~ 0	94.0 ± 2.8	59.4 ± 1.4
θ_{adv} (deg) on Steel	~ 0	61.5 ± 3.3	48.5 ± 4.3
θ_{adv} (deg) on Parafilm	22.5 ± 1.4	115.0 ± 6.3	105.4 ± 4.5
θ_{rec} (deg) on Aluminum	~ 0	~ 0	~ 0
θ_{rec} (deg) on Steel	~ 0	6.8 ± 1.0	~ 0
θ_{rec} (deg) on Parafilm	~ 0	86.1 ± 5.5	71.3 ± 2.0
$\theta_D(t_{max})$ (deg) on Aluminum	51.4 ± 5.8	115.5 ± 5.8	107.6 ± 2.9
$\theta_D(t_{max})$ (deg) on Steel	43.9 ± 2.5	102.9 ± 3.2	121.2 ± 6.9
$\theta_D(t_{max})$ (deg) on Parafilm	63.0 ± 5.9	107.6 ± 5.6	116.2 ± 5.9

Huang and Chen [40] measured the maximum spreading diameter and spreading time in their experiments where water droplets impacting on Parafilm surface, $D_0 = 0.0027mm$, $V_0 = 0 \sim 3.83m/s$. The measured advancing contact angle θ_{adv} between water droplet and parafilm is $110^\circ \pm 7^\circ$.